IVW - Schriftenreihe Band 82
Institut für Verbundwerkstoffe GmbH - Kaiserslautern

Suchart Siengchin

Water-Mediated Melt Compounding to Produce Thermoplastic Polymer-Based Nanocomposites: Structure-Property Relationships

Bibliografische Information Der Deutschen Bibliothek

Die Deutsche Bibliothek verzeichnet diese Publikation in der Deutschen Nationalbibliografie; detaillierte bibliografische Daten sind im Internet über <http://dnb.ddb.de> abrufbar.

Bibliographic information published by Die Deutsche Bibliothek

Die Deutsche Bibliothek lists this publication in the Deutsche Nationalbibliografie; detailed bibliographic data is available in the Internet at <http://dnb.ddb.de>.

Herausgeber: Institut für Verbundwerkstoffe GmbH
Prof. Dr.-Ing. Alois K. Schlarb
Erwin-Schrödinger-Straße
TU Kaiserslautern, Gebäude 58
67663 Kaiserslautern
http://www.ivw.uni-kl.de

Verlag: Institut für Verbundwerkstoffe GmbH

Druck: Technische Universität Kaiserslautern
ZBT – Abteilung Foto-Repro-Druck

D 386

Als Manuskript gedruckt. Printed in Germany.
ISSN 1615-021X
ISBN 978-3-934930-78-0
ISBN 3-934930-78-6

Water-Mediated Melt Compounding to Produce Thermoplastic Polymer-Based Nanocomposites: Structure-Property Relationships

Vom Fachbereich für Maschinenbau und Verfahrenstechnik
der Technischen Universität Kaiserslautern
vorgelegte Dissertation
zur Verleihung des akademischen Grades

Doktor-Ingenieur (Dr.-Ing.)

genehmigte Dissertation

von

Dipl.-Ing.(FH), M.Sc., M.Sc. Suchart Siengchin

aus Bangkok, Thailand

Tag der mündlichen Prüfung: 25 August 2008

Prüfungsvorsitzender: Prof. Dipl.-Ing. Dr. techn. habil. Hans-Jörg Bart
1. Berichterstatter: Prof. Dr.-Ing. habil. Dr. h.c. József Karger-Kocsis
2. Berichterstatter: Prof. Dr.-Ing. Tibor Czigány

Acknowledgements

The present work was completed between November 2005 and August 2008 at the Institute for Composite materials (Institut für Verbundwerkstoffe GmbH, IVW) of the Technical University of Kaiserslautern, Germany.

First and foremost, I would like to express my special gratitude to my supervisor Prof. Dr.-Ing. habil. Dr.h.c. József Karger-Kocsis for his scientific support and constant interest on my work. Our fruitful discussions on polymer science and technology during my stay as PhD research assistant broadened my knowledge and enlightened the perspectives of this field. I am thankful to Prof. Dr. techn. Hans-Jörg Bart for accepting the presidency of the examination committee and to Prof. Dr.-Ing. Tibor Czigány for the co-referent of this PhD thesis.

I would like to express my special acknowledgements to Dr. Anton A. Apostolov, Dr. Ralf Thomann and Dr. Georgios Ch. Psarras for the X-ray Diffraction Scattering (XRD), Transmission Electron Microscopy (TEM) and Broadband dielectric experiments, respectively. Their assistance and scientific skills accelerated the progress of this thesis significantly.

I would like to thank the German Science Foundation (DFG) for the financial support. I am grateful to the IVW for providing me the opportunity of working in an outstanding environment from the scientific and technical point of view. The support of the colleagues at the IVW is grateful acknowledged during my stay. Many thanks to Mr. Herrmann Giertzsch, Mr. Rolf Walter, Mr. Joachim Stephan and Mr. Ralf Schimmele for their kind help in the experiments. Especially I would like to express my appreciation for the help and friendship to Dr. Sergiy Gryshchuk, Dr. Zhenyu Jiang, Dr. Thomas N. Abraham, Dr. Santosh Wanjale, MS.c. Nuria Castellá and Dipl.-Ing. Andŕe Meichsner.

I would like to convey my special thanks to my parents and my sisters and brother who constantly supported and encouraged me.

Table of Contents

Abstract

Nanotechnology is now recognized as one of the most promising areas for technological development in the 21st century. In materials research, the development of polymer nanocomposites is rapidly emerging as a multidisciplinary research activity whose results could widen the applications of polymers to the benefit of many different industries. Nanocomposites are a new class of composites that are particle-filled polymers for which at least one dimension of the dispersed particle is in the nanometer range. In the related area polymer/clay nanocomposites have attracted considerable interest because they often exhibit remarkable property improvements when compared to virgin polymer or conventional micro- and macro- composites.

The present work addresses the toughening and reinforcement of thermoplastics via a novel method which allows us to achieve micro- and nanocomposites. In this work two matrices are used: amorphous polystyrene (PS) and semi-crystalline polyoxymethylene (POM). Polyurethane (PU) was selected as the toughening agent for POM and used in its latex form. It is noteworthy that the mean size of rubber latices is closely matched with that of conventional toughening agents, impact modifiers. Boehmite alumina and sodium fluorohectorite (FH) were used as reinforcements. One of the criteria for selecting these fillers was that they are water swellable/dispersible and thus their nanoscale dispersion can be achieved also in aqueous polymer latex. A systematic study was performed on how to adapt discontinuous- and continuous manufacturing techniques for the related nanocomposites.

The dispersion of nanofillers was characterized by transmission, scanning electron and atomic force microcopy (TEM, SEM and AFM respectively), X-ray diffraction (XRD) techniques, and discussed. The crystallization of POM was studied by means of differential scanning calorimetry and polarized light optical microscopy (DSC and PLM, respectively). The mechanical and thermomechanical properties of the composites were determined in uniaxial tensile, dynamic-mechanical thermal analysis (DMTA), short-time creep tests, and thermogravimetric analysis (TGA).

PS composites were produced first by a discontinuous manufacturing technique, whereby FH or alumina was incorporated in the PS matrix by melt blending with and without latex precompounding of PS latex with the nanofiller. It was found that direct

melt mixing (DM) of the nanofillers with PS resulted in micro-, whereas the latex mediated pre-compounding (masterbatch technique, MB) in nanocomposites. FH was not intercalated by PS when prepared by DM. On the other hand, FH was well dispersed (mostly intercalated) in PS via the PS latex-mediated predispersion of FH following the MB route. The nanocomposites produced by MB outperformed the DM compounded microcomposites in respect to properties like stiffness, strength and ductility based on dynamic-mechanical and static tensile tests. It was found that the resistance to creep (summarized in master curves) of the nanocomposites were improved compared to those of the microcomposites. Master curves (creep compliance vs. time), constructed based on isothermal creep tests performed at different temperatures, showed that the nanofiller reinforcement affects mostly the initial creep compliance.

Next, ternary composites composed of POM, PU and boehmite alumina were produced by melt blending with and without latex precompounding. Latex precompounding served for the predispersion of the alumina particles. The related MB was produced by mixing the PU latex with water dispersible boehmite alumina. The composites produced by the MB technique outperformed the DM compounded composites in respect to most of the thermal and mechanical characteristics.

Toughened and/or reinforced PS- and POM-based composites have been successfully produced by a continuous extrusion technique, too. This technique resulted in good dispersion of both nanofillers (boehmite) and impact modifier (PU). Compared to the microcomposites obtained by conventional DM, the nanofiller dispersion became finer and uniform when using the water-mediated predispersion. The resulting structure markedly affected the mechanical properties (stiffness and creep resistance) of the corresponding composites. The impact resistance of POM was highly enhanced by the addition of PU rubber when manufactured by the continuous extrusion manufacturing technique. This was traced to the dispersed PU particle size being in the range required from conventional, impact modifiers.

Kurzfassung

Die Nanotechnologie wird heute als eines der bedeutendensten Gebiete für technologische Entwicklungen des 21. Jahrhunderts gehalten. In der Werkstoffwissenschaft hat sich die Entwicklung von Polymernanocompositen schnell zu einem multidisziplinären Forschungsfeld entwickelt. Dessen Ergebnisse konnten das Einsatzgebiet von Kunststoffen zum Vorteil verschiedener Industriezweige erweitern. Nanocomposite sind eine neue Materialklasse, wobei es sich bei diesen Werkstoffen um partikelgefüllte Kunststoffe handelt. Die Größe der feinstverteilten Partikel liegt im Nanometerbereich. Weiterhin hat das Gebiet der Polymer/Schichtsilikat Nanocomposite beachtliches Interesse auf sich gezogen, da sie im Vergleich mit reinen Polymeren bzw. konventionellen Mikro- und Makrocompositen in vielen Fällen eine deutliche Eigenschaftsverbesserung zeigen.

Die vorliegende Arbeit beschäftigt sich mit der Zähigkeitsmodifizierung und der Verstärkung von Thermoplasten mittels einer neuartigen Methode, die es erlaubt Mikro- und Nanocomposite herzustellen. Es wurden zwei Matrixsysteme untersucht: zum einen amorphes Polystyrol (PS) und zum anderen teilkristallines Polyoxymethylen (POM). Als Zähigkeitsmodifikator für POM wurde Polyurethan (PU) eingesetzt, welches in Latex-form verwendet wurde. Die Kautschukpartikelgröße stimmt mit Abmessungen konventioneller Zähigkeitsmodifikatoren überein. Für die Partikelverstärkung wurde synthetischer Boehmit und synthetischer Fluorohectorit (FH) eingesetzt. Ein Grund für die Auswahl dieser Verstärkungselemente lag in deren Wasserlöslichkeit bzw. Wasserdispergierbarkeit. Dadurch konnte eine nanoskalige Dispersion auch in wasserbasiertem Polymer-Latex erzielt werden. Weiterhin wurde im Rahmen der Arbeit eine systematische Studie über die Adaption von diskontinuierlichen und kontinuierlichen Herstellungstechniken für derartige Nanocomposite durchgeführt.

Die Dispersion der Füllstoffe wurde durch Transmissions-, Rasterelektronen-, Atomkraftmikroskopie (TEM, REM und AFM), Röntgendiffraktion (XRD) charakterisiert und diskutiert. Die Kristallinität von POM wurde mittels Differentialkalorimetrie und Polarisationslichtmikroskopie (DSC und PLM) untersucht. Eine Bestimmung der mechanischen und thermomechanischen Eigenschaften der Composite erfolgte durch quasistatische Zugversuche, dynamisch-mechanische

thermische Analyse (DMTA), Kurzzeitkriechversuche und thermogravimetrische Analyse (TGA).

Die PS-Verbundwerkstoffe wurden zunächst mit Hilfe eines diskontinuierlichen Verfahrens hergestellt, wobei FH oder Aluminiumoxid durch ein Schmelzcompoundierverfahren, mit oder ohne Vorkompoundierung des PS-Latex mit Nanofüllstoffen, eingearbeitet wurden. Es wurde festgestellt, dass wenn die Nanofüllstoffe mit dem PS im direkten Schmelzverfahren (DSV) verarbeitet wurden Microcomposite zur Folge hatten, während bei Anwendung der latexbasierenden Masterbatchtechnik (MBT) Nanocomposite entstanden. Die FH Partikel wurden durch PS-ketten nicht interkaliert, wenn es mit dem DSV verarbeitet wurde. Andererseits wurde das FH gut im PS dispergiert und lag in interkalierter Form vor, wenn die MBT angewendet wurde. Die Nanocomposite, die mittels MBT hergestellt wurden, übertreffen die Microcomposite, die mit Hilfe des DSV gefertigt wurden, in diversen Eigenschaften, wie zum Beispiel: Steifigkeit, Festigkeit und Duktilität. Außerdem konnte der Kriechwiderstand der Nanocomposite im Vergleich zu den Microcompositen verbessert werden, was in Masterkurven zusammengefasst wurde. Diese Masterkurven (Änderung der Nachgiebigkeit über die Zeit) wurden basierend auf den Ergebnissen von isothermen Kriechversuchen konstruiert, welche bei verschiedenen Temperaturen durchgeführt wurden. Sie zeigen, dass die Nachgiebigkeit am Anfang von der Nanoverstärkung beeinflusst wird. Im Rahmen der Arbeit wurde weiterhin ein dreikomponentiger Verbundwerkstoff untersucht, welcher aus POM, PU und Boehmit hergestellt wurde. Das bewährte Schmelzcompoudierverfahren, mit oder ohne Vorkompoundierung des Latex zur Verteilung der Boehmitpartikel, wurde erneut verwendet. Das zugehörige Masterbatch (MB) wurde durch Mischen von PU-Latex mit in Wasser dispergiertem Boehmit hergestellt. Die Composite, die mit der MBT hergestellt wurden, übertrafen die mittels DSV gefertigten Composite in den meisten thermischen und mechanischen Eigenschaften.

Im Rahmen der durchgeführten Forschungsarbeiten konnten zähigkeitsmodifizierte und/oder verstärkte PS- und POM- basierte Verbundwerkstoffe erfolgreich mittels einer kontinuierlichen Extrusionstechnik hergestellt werden. Der Einsatz der Extrusionstechnologie hatte eine gute Dispersion von Nanofüllstoff (Boehmit) und

Zähigkeitsmodifikator (PU) zur Folge. Weiterhin konnte im Vergleich zu den Mikrocompositen, welche im konventionellen DSV hergestellt wurden, durch den Einsatz einer wasserbasierten Vordispersion eine feinere und gleichmäßigere Verteilung der Nanofüllstoffe erreicht werden. Die resultierende Struktur der jeweiligen Composite hat einen wesentlichen Einfluss auf die mechanischen Eigenschaften Steifigkeit und Kriechwiderstand ausgeübt. Die Impakteigenschaften von POM konnten durch die Zugabe von PU-Kautschuk deutlich verbessert werden, wenn die kontinuierliche Extrusionsfertigungstechnik angewendet wurde. Diese Verbesserung der Impakteigenschaften ist begründet durch die Größe der dispergierten PU-Partikel, welche in der Größenordnung konventioneller Zähigkeitsmodifikatoren liegt.

List of Abbreviations and Symbols

Abbreviations

Al	Aluminium
Au	Gold
Ag	Silver
Al_2O_3	Aluminum oxide
AFM	Atomic force microcopy
$CaCO_3$	Calcium carbonate
CNT	Carbon nanotube
DSC	Differential scanning calorimetry
DM	Direct melt compounding
DM-CT	Direct melt compounding continuous technique
DMTA	Dynamic-mechanical thermal analysis
Disperal® P2	Disperable boehmite alumina type P2
Dispal® 11N7-80	Disperable boehmite alumina type 11N7-80
EDAX	Energy dispersive analysis X-ray spectrometry
FH	Sodium fluorohectorite
Fe	Iron
HDT	Heat distortion temperature
IP	Interfacial polarization
MB	Masterbatch technique
MBa	Advanced masterbatch technique
MVR	Melt volume rate
MWS	Maxwell-Wagner-Sillars
Na_2SiF_6	Sodium hexaflorosilicate
Na_2O	Sodium oxide

PS	Polystyrene
POM	Polyoxymethylene
PU	Polyurethane
PLM	Polarized optical microscopy
RT	Room temperature
rpm	revolution per minute
SiO_2	Silicon dioxide
SEM	Scanning electron microcopy
SP	Softening point
TiO_2	Titanium dioxide
TEM	Transmission electron microcopy
TGA	Thermo gravimetric analysis
TPU	Thermoplastic polyurethane
TTS	Time temperature superposition
WM-CT	Water mediated continuous technique
WLF	Williams-Landel-Ferry
wt.%	Weight percent
XRD	Wide angle X-ray diffraction scattering
ZnO	Zinc oxide

Symbols

a_T	[1]	Shift factor
c	[1]	Constant factor
D, D_r	[GPa^{-1}]	Creep-, recovery compliance
D_k	[GPa^{-1}]	Compliance of the Kelvin unit
D_F	[GPa^{-1}]	Creep compliance of Findley power law
D_{F0}	[GPa^{-1}]	Time-independent compliance
D_{F1}	[$GPa^{-1}s^{1/n}$]	Creep coefficient of the time-dependent term
ΔH	[kJ/mol]	Activation energy
E^*	[MPa]	Complex modulus
$E^{'}$, $E^{''}$	[MPa]	Storage-, loss modulus
E_r	[GPa]	Relaxation modulus
$E_{0,}$ E_k	[Gpa]	Zero-time-, different relaxation modulus
E_{rF}	[GPa^{-1}]	Relaxation modulus of inverse Findley power law
E_{rF0}	[GPa^{-1}]	Time-independent relaxation
E_{rF1}	[$GPa^{-1}s^{1/n}$]	Relaxation coefficient of the time-dependent term
f, f_0	[Hz]	Actual-, reference frequency
H_m	[J/g]	Melting enthalpy
L	[mm]	Length
M^*	[MPa]	Complex dielectric electric modulus
$M^{'}$, $M^{''}$	[MPa]	Real-, imaginary dielectric modulus
n	[1]	Constant independent of stress
R	[$J \cdot K^{-1} \cdot mol^{-1}$]	Universal gas constant
r	[mm]	Radius
T, T_0	[°C]	Actual-, reference temperature
T_g, T_c	[°C]	Glass transition-, crystallization tempera ture

T_f, T_m	[°C]	Flow-, melting temperature
t	[s]	Time
tan δ	[1]	Mechanical loss factor
X_c	[%]	Crystallinity

Greek Symbols

ε, ε_0	[%]	Strain-, amplitude of the strain
ε', ε''	[F/m]	Real-, imaginary permittivity
ψ	[GPa^{-1}]	Equilibrium compliance part
σ	[MPa]	Stress
σ_0	[MPa]	Applied constant stress
θ	[°]	Angle
ω	[rad/s]	Angular frequency
μ_0	[Pa.s]	Viscosity (Strain)
τ	[s]	Retardation time
η^*	[Pa.s]	Complex Viscosity
δ	[1]	Phase angle shift

1 State of the Art

1.1 Introduction

Nowadays great effects are undertaken to improve the mechanical, thermal and other properties (e.g. flame resistance, barrier properties, electric conductivity) of polymers. To achieve this property upgrade nanocomposites are produced using fillers of various shape factors and dispersing them on nano-scale resulting in the formation of nanocomposites. For example, the modification of polystyrene (PS) was already tried with metal oxides [1-2], organophilic modified layered silicates [3-14], single and multiwall carbon nanotubes [15-17]. Layered silicates of natural and synthetic origin exhibit several interesting properties which can well be exploited for the property modification of polymers [18-21]. First, they show swelling capability in water and other fluids. Second, layered silicates have a platy (disc) structure with very high aspect ratio (as their thickness is ca. 1 nm and their length can reach up to 2 µm the aspect ratio is up to 2000) offering very large polymer/silicate interface area. Third, due to isomorphic substitution of the constituting Si and Al atoms by other ones in the crystal structure the layers become negatively or positively charged. This surface charge is balanced by cations and anions, respectively, located between the layers. It is noteworthy that layered silicates with cation exchange capacity were exclusively used for polymer modification so far. The interlayer cations are usually replaced by alkylammonium cations rendering the layered silicates “organophilic”. The onium cations, usually with long alkyl chains, widen the initial interlayer distance (initially at about 1 nm) (e.g. [22]). So, the interlayer distance of commercially available montmorillonite based clays (the term clay is used throughout the text if the layered silicate is of natural origin) is between 1.5 and 2.5 nm. This distance is enough to produce intercalated and exfoliated structures. In an intercalated structure, silicate sheets maintain their layer stacking, but the gallery distance has increased to accommodate the intercalated polymer chains. In an exfoliated structure, silicate sheets lose their layered geometry and are individually dispersed in the polymers.

The intercalation/exfoliation of PS was preferred topics of different studies. This is mostly due to the amorphous nature of PS which allows us to study the intercalation/exfoliation processes in absence of crystallization. So, Krishnamoorti et al. [23]

demonstrated in their early work the effect of polymer diffusion on the intercalation of PS in organophilic layered silicate. Very recent works on PS/layered silicate nanocomposites dealt with effects of processing parameters during melt compounding (e.g. [24]) and with the in-situ polymerization of styrene in presence of organophilic modified layered silicates (e.g. [6-7, 25]). Effect of clay particles on the film formation from PS latex was also investigated recently [26]. Shen et al. explored the production of water-expandable PS/clay nanocomposite via the “latex route” [27].

Polyoxymethylene (POM) is another thermoplastic which became under spot of research interest due to its excellent mechanical properties (creep resistance, high stiffness and high heat deflection temperature) and resistance against various solvents [28-30]. The extreme high crystallinity of POM, accompanied with brittleness is the limiting factors of its applications [31-32]. Blending of POM with thermoplastic polyurethane elastomer (TPU) [33-36] or compounding with both rubber and rigid particles [37], have attracted considerable attention in recent years owing to the achieved improvements in toughness. Recently, nanosilica/POM latex was used by Wang et al. [38] to obtain a hybrid film which exhibited good surface properties and better thermal behavior than the unmodified POM.

It was early recognized that the preparation technique of the nanocomposites has a strong impact on the dispersion of the nanoparticles. Usually one differentiates between in-situ polymerization, melt blending and solution/dispersion preparation techniques [39]. The latter grouping covers also the latex compounding/latex coagulation methods. Major benefits of the “latex route” are listed below. It is noteworthy that for the production of rubber nanocomposites the latex coagulation is already widely used [40-43]. Note that many polymers are produced by suspension and emulsion polymerizations in aqueous media. The related suspensions, emulsions or latices can be easy modified with water swellable or water dispersible particles. Water swellable are for example several layered silicates (montmorillonites, bentonites) bearing intergallery inorganic cations. Via hydration of the intergallery cations the layered silicates became intercalated and exfoliated. So, the production of nanocomposites from polymer latex/layered silicate may be facile and affordable.

Among the water dispersible commercially available nanofillers boehmite alumina (AlO(OH)) should be mentioned. To produce nanocomposites using aqueous disper-

sions, slurries is not only an affordable method (no organophilic modification is needed for the fillers) but associated also with reduced health hazard. Recall that the particles introduced are in micron range and become nano-scaled only in the aqueous media. In the follow-up steps (coagulation, drying etc.) the nanoparticles are embedded in the polymer which guarantees easy handling and minimized health risk. Apart from rubbers, this “latex-route” is followed for various polymers, including POM and PS [44-46], to produce various nanocomposites. There is a further scientific beauty with this approach: it is possible to produce micro- and nanocomposites using the same components. This is very straightforward in order to figure out whether a “nanoeffect” exists and what is its influence on the material performance.

Water dispersible alumina, offered by the company Sasol were already incorporated in thermoplastics [47-49], thermosets [50], and even in thermoplastic rubbers [51], however usually after their organophilic modification. In pristine form alumina nanoparticles were dispersed in polyurethane rubber through latex compounding [52]. Note that the alumina particles remain in agglomerates (micron-sized) when introduced in polymers by melt blending.

In this work, a novel method was used to produce nanoreinforced and/or toughened thermoplastics. This comprises a water-assisted melt compounding whereby nanoparticles in water slurry and rubber latices are introduced in the polymer melt.

1.2 Background

1.2.1 Thermoplastic materials

A thermoplastic is a plastic that melts to a liquid when heated and solidifies when cooled. Most thermoplastics are high molecular weight polymers whose chains associate through weak Van der Waals forces (polyethylene); stronger dipole-dipole interactions and hydrogen bonding (polyamide); or even by stacking of aromatic rings (polystyrene). Thermoplastic polymers differ from thermosetting ones (cured resins; vulcanized rubber) as they can, unlike thermosetting polymers, be remelted and remoulded. Many thermoplastic materials are produced by polymerization such as polyethylene and polypropylene. Engineering plastics belong to another group of plastic materials that exhibit superior mechanical and thermal properties which enable them for prolonged use in structural applications over a wide temperature range, under mechanical stress and even in aggressive chemical environments (polyoxymethylene). The engineering plastics usually refer to thermoplastic materials rather than thermosetting ones.

Thermoplastic materials generally fall within two classes of molecular arrangement, namely amorphous and semi-crystalline. This classification is based on the existence of a long range order with respect to molecular arrangement. The molecules occupy definite positions within the crystal lattice and this well-defined arrangement is repeated several times in all the three dimensions of the crystal to give rise to long-range order of the crystalline solids.

Amorphous

A polymer which does not possess long-range order is never crystalline. It is non-crystallisable or amorphous, and exists in the glassy, rubbery or liquid states. At low temperatures, where it does not possess either segmental or molecular mobility, it exists as a glassy solid. On heating beyond a certain temperature, segmental mobility comes into play and the polymer becomes rubbery. This temperature at which the amorphous polymer passes from the glassy state to a rubbery state is the glass transition temperature (T_g). On further heating the rubbery polymer (much above its T_g) reaches a temperature is beyond which molecular motions become activated and the polymer starts flowing. The temperature at which the molecular mobility sets in

and the polymer passes from the rubbery state to the liquid state is called its flow temperature (T_f). This is, however, rather a temperature range than a single temperature.

Crystalline and semi-crystalline

A polymer capable of exhibiting long-range order is called crystalline polymer (polymer which is 100% crystalline – in practice does not exist except when grown as single crystal). At low temperatures, when molecular mobility is arrested, it exists in the crystalline solid state. The segments in a crystalline polymer are firmly held in the crystallites by intermolecular forces and, hence, do not exhibit any segmental mobility, even at fairly high temperatures. The crystalline polymer, therefore, does not pass from solid state to rubbery state and thus does not possess any T_g. At a sufficiently high the temperature polymer now passes from the crystalline state directly into the liquid state. The temperature at which this transition takes place is called the melting temperature (T_m). Most of the polymers in practical use are, neither fully crystalline nor completely amorphous. They are partially crystalline and consist of both amorphous as well as crystalline regions. Partially crystalline polymers possess both the T_g and T_m. Below T_g, the amorphous regions of the polymer exist in the glassy state and the crystalline regions in the crystalline state. At T_g the amorphous regions pass into the rubbery state, while the crystalline regions remain in the crystalline state. At T_m, the crystalline regions melt and pass into the liquid state. Beyond T_m, the amorphous regions and the crystalline regions become one and the polymer as a whole is in the liquid state [53-54].

The crystalline regions in a polymer neither have a regular shape nor have a perfect lattice structure. The expression ‘highly ordered state of chain molecules in the crystalline regions in a polymer’ has been used to suggest that in these volume elements of the polymeric substance, the chain segments are so arranged as to form ordered bundles or aggregates. These orderly regions in a polymeric substance are called ‘crystallites’. This can be visualized as regions composed of imperfect crystal-like chain aggregates. A partially crystalline polymeric material consists of several such crystallites co-existing with amorphous regions of disorderly placed chain segments. No sharp boundaries exist between the crystallites and the amorphous

regions. The former are connected to the latter by polymer chains running through both the regions (Figure 1.1).

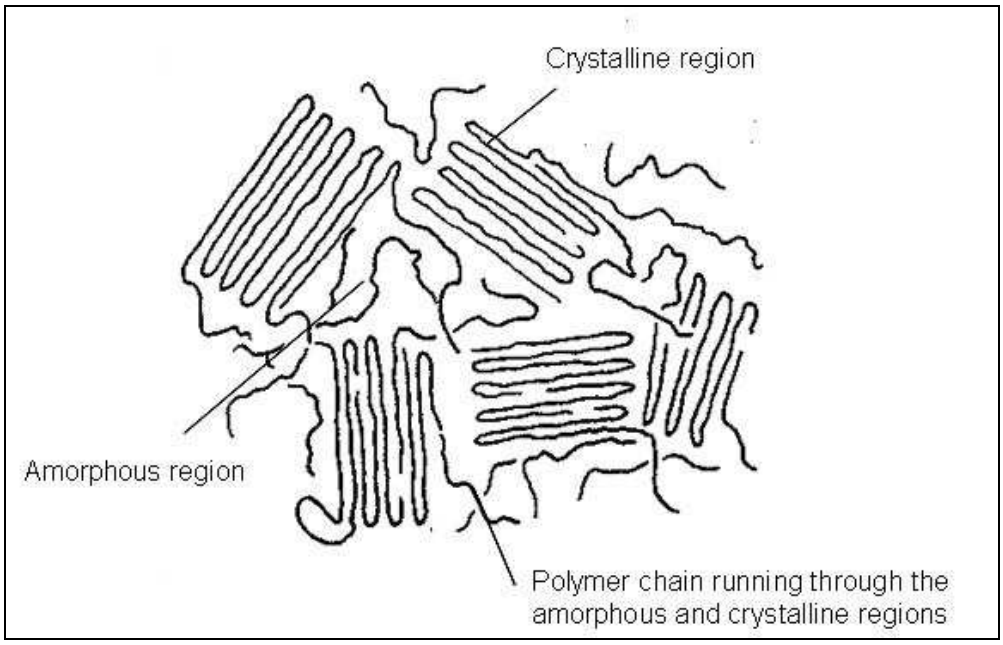

Figure 1.1: Schematic macromolecular structures of a semi-crystalline polymer

1.2.2 Nanoreinforced and Toughened Polymer Composites

1.2.2.1 Nanofillers of interest

Recent researches have shown that particles on the nanometer-scale have many physico-chemical effects that differ greatly from those on the macroscopic scale. Nanofillers are often defined as small particles with at least one dimension less than 100 nm. Different organic/inorganic fillers are used in various composite materials for specific purposes [55]. Inorganic fillers such as metals (Al, Fe, Au, Ag), metal oxides (ZnO, Al_2O_3, $CaCO_3$, TiO_2) and nonmetal oxide (e.g. SiO_2) have been dispersed in different polymers in nanoscale range. Nanoscale fillers are available in many shapes and sizes (cf. Figure 1.2). They are classified into three groups as follows [56]:

a) Fibre or tube fillers having a diameter smaller than 100nm and an aspect ratio of at least 100 (e.g. carbon nanotubes, CNT, may have an aspect ratio of ca. 10^5).

b) Nanoplates showing a thickness of about 1nm and at least an aspect ratio of 25 in the other two dimensions (layered silicates).

c) Three dimensional (3D) nanofillers which have relatively balanced edge lengths being smaller than 100 nm in their largest dimension (e.g. silica, carbon black).

Incorporation of nanofillers may cause a dramatic change in the properties of the material depending on the shape of the nanofillers. The selection of nanoparticles depends on the desired materials properties, such as improvement of mechanical, thermal and electrical, as well as, barrier properties and flame retardancy. For example, metal fillers are chosen to improve high temperature creep properties, hardness and conductivity while the dispersion of a filler of photocatalytic activity (e.g. TiO_2) can confer a continuous, long lasting antibacterial activity on the surface of polymer. For nonmetal oxides, silica nanofillers are used because of their extremely high thermal stability. In addition, SiO_2 possesses a very low thermal expansion coefficient.

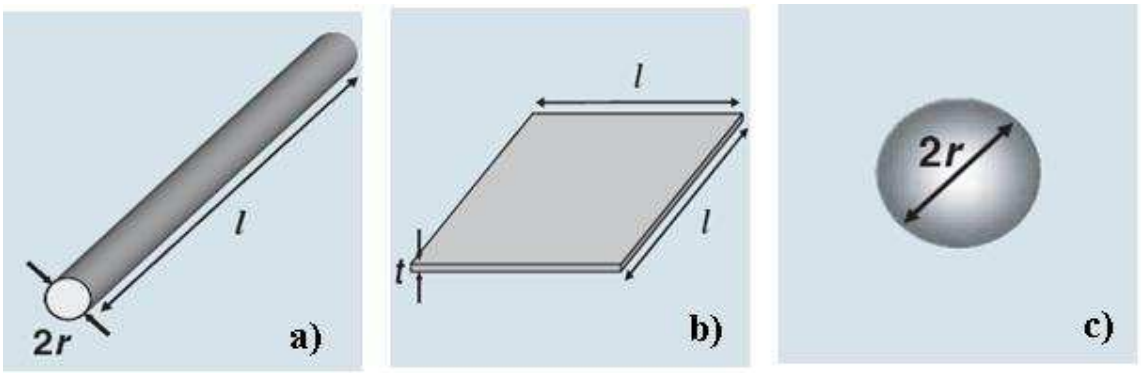

Figure 1.2: Classification of common particle reinforcements/geometries. a) fibrous material , b) layered material and c) particulate material [56]

1.2.2.2 Toughness of Polymers

Incorporation of nanofillers in organic polymers can result in a brittle composite material with limited application possibility. Blending the thermoplastic with elastomeric modifiers is a successful way to overcome this problem and to improve the toughness characteristics. Many works have documented the effect of various parameters of the modifiers on the toughness response including rubber particle size [57-58], rubber concentration [57, 59] and interparticle distance [60-61]. These studies revealed that the rubber concentration should be above a critical level in function of its particle size. To improve the toughness of a polymer, the interparticle distance should fall below a critical value which depends on the volume fraction and the particle size of the rubbers. In this case, namely, the stress fields of neighboring particles overlap (cf. Figure 1.3) and a larger volume fraction of the matrix supports an average load higher than the applied load. Multiple localized plastic deformations are hereby initiated in the plastic zone ahead of the crack tip. Typical rubber loading is up to 10 wt.-% and particle sizes for effective toughening should range between 100 nm and 10 µm. Only particles larger than 100 nm produce an adequate stress concentration effect. Smaller particles cannot store sufficient elastic energy. Rubber particles with diameters larger than 10 µm have been found to be relative inefficient, although they might be active in crack bridging.

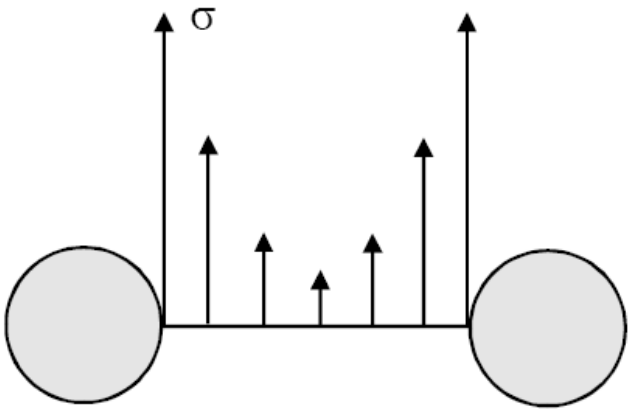

Figure 1.3: Schematic diagram of the stress field overlapping between rubber particles

1.2.3 Composites and their Compounding Techniques

A composite material is consisting of several components. The base, the continuous phase, is called matrix and the discontinuous one is termed filler. Considering the formulation of a compound for a particular type of application, it is important to consider the effect that the constituent exert on the compound. In this case special attention was paid on polymer composites with polyoxymethylene (POM) and polystyrene (PS) matrices, due to their excellent physico-mechanical, thermal and promising functional properties in presence of various nanoparticles [62-66].

To prepare polymeric nanocomposites different methods have been followed, such as in-situ polymerization, melt blending and solution/dispersion techniques. Note that in the corresponding nanocomposites nanoscaled fillers are present. It was early noticed that the preparation technique of the nanocomposites has a strong impact on the dispersion of the nanoparticles [67]. In situ polymerization is a challenging one, as it allows us to adjust the chemistry to optimize the affinity between filler and the resulting polymer. Different types of polymerization methods have been used to prepare polymer nanocomposites, such as solution [68], suspension [69] or emulsion [70], and free radical polymerizations [71]. This variety to prepare polymer nanocomposites by in situ polymerization was mostly explored with clays. However, this process is cumbersome and also costly. If the organophilic modification of inorganic fillers could be eliminated, the procedure might be simplified and the production cost substantially lowered compared to state-of-art processes.

The use of conventional melt compounding techniques to prepare nanocomposites is usually more practical and economical than in situ polymerization. For that purpose common polymer processing equipments, such as extruders and internal mixers are suited. The shear, accommodated in the melt during processing may also be helpful to support the clay dispersion. However, it is not always enough to break up big clay agglomerates as the resulting clay dispersion may remain further poor.

An alternative way to prepare composite materials is the latex compounding/latex coagulation technique. Latex compounding is a promising technique compared for example to in-situ polymerization and solution techniques which are used to produce nanocomposites. It is becoming more and more important because of the following benefits: simple many polymers are available in latex form, latex can be introduced in

polymer melt during compounding in line. In an aqueous polymer latex, microscopic solid polymer particles are suspended in water. During drying they form a film through coalescence. When combined with nano-sized filler, the polymer particles and the filler create a segregated network. This may show excellent properties at very low filler concentration [72], compared to a melt blended version containing the same polymer and filler. So, Grunlan et al. [73] demonstrated in their early work, the formation of segregated network during drying (cf.-Figure 1.4). The advantage of this latex compounding process is that the expensive chemical modification of the fillers, giving the necessary affinity to the polymer, can be avoided. Moreover, when the nanofiller is well dispersed in the polymer latex, the latter can be used as a master-batch (in both dry and liquid forms) for subsequent melt compounding. In addition, nanofiller containing latices or slurries can be injected in the melt during continuous melt compounding. Exactly, these are those options which have been explored in this work.

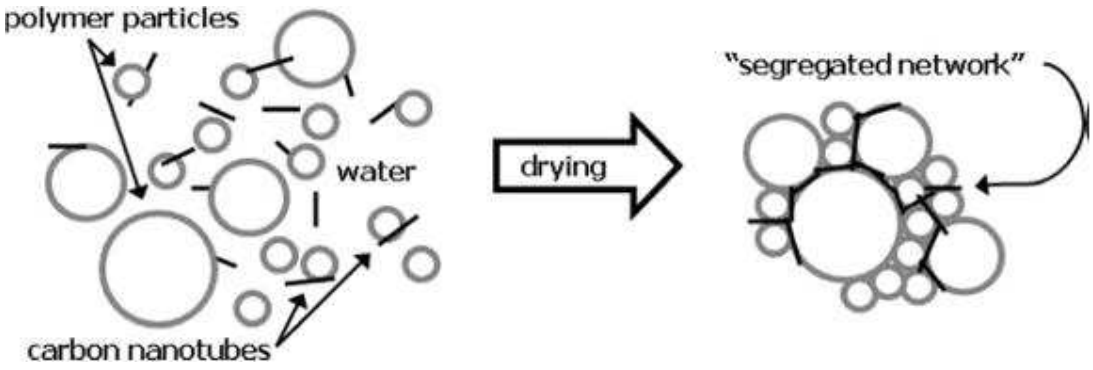

Figure 1.4: Schematic illustration of a segregated network of carbon nanotubes [73]

1.2.4 Viscoelastic Behavior Analysis

Composite materials used for structural applications of practical interest may exhibit viscoelastic behavior which has a profound influence on their performance. Viscoelasticity is of interest in materials science and engineering since it is causally linked to a variety of microphysical processes and can be used as an experimental probe of those processes. The causal links between viscoelasticity and microstructure are explored in various viscoelastic tests. The viscoelastic behavior of polymers and related composites is usually characterized in creep test (whereby the creep strain is measured in time under a constant load) or dynamic mechanical test (where the variation in storage and loss moduli is observed as a function of the temperature) [74-75].

Creep Analysis

To describe the creep results, phenomenological models, composed of spring and dashpot elements, are frequently used, cf. Figure 1.5. A spring element (elastic) behaves exactly like a metal spring, stretching instantly when stress is applied, maintaining the stress indefinitely, and returning to its original dimension instantly when stress is removed. In a dashpot (viscous) under stress, the plunger moves through the fluid at a rate that is proportional to the stress. In a creep experiment, the stress is kept constant and the change in the deformation of the polymer as function of time is recorded.

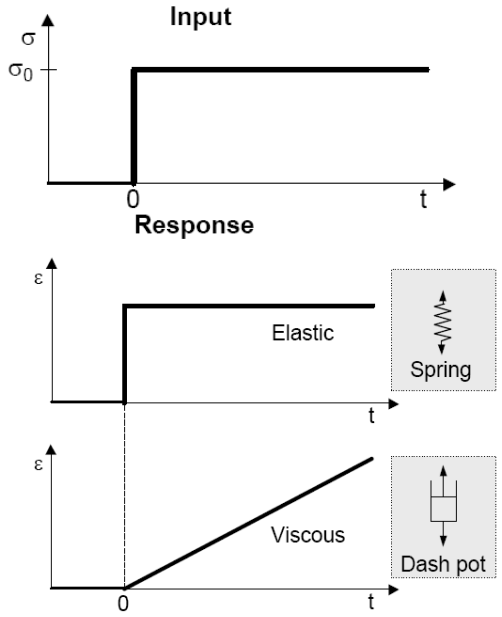

Figure 1.5: Behavior of a Hookian spring and a Newtonian dashpot under excitation of constant load

In the linear viscoelastic range, the parameters of this series do not depend on the level of the applied load. For creep under applied constant stress σ_0, the material response is:

$$D(t) = \frac{\varepsilon(t)}{\sigma_0} \tag{1.1}$$

where D(t) is the viscoelastic creep compliance and ε(t) is creep strain at time, t.

In the nonlinear range the dependence upon the level of the applied load can be expressed by multiplying the linear parameters by so-called nonlinearity factors, which, of course, are load, time and temperature dependent [76-77]. The nonlinear creep compliance is given by:

$$D(t,\sigma(t),T) = \frac{\varepsilon(t,\sigma(t),T)}{\sigma_0} \tag{1.2}$$

where σ (t) is the real stress at time, t and T is temperature. This equation can be simplified with:

$$\varepsilon(t,\sigma(t),T) = \varepsilon(t,\sigma_0,T) = \varepsilon(t,T)c\sigma_0 \qquad (1.3)$$

Thus, the following equation can be also expressed in terms of creep compliance

$$D(t,\sigma(t),T) = D(t,\sigma_0,T) = c\varepsilon(t,T) \qquad (1.4)$$

where c is a constant. In the above equation creep compliance is only a function of the time and temperature.

Time-temperature-superposition

In order to predict the long-term creep behavior based on short-term creep measurements, it is generally assumed that the polymer does not change its structure with time. So, the Time-temperature-superposition (TTS) principle can be adopted. TTS has been used to obtain the master curves for creep compliance against time. According to TTS the creep at a given temperature (T_0) is related to the creep at another temperature (T) by considering the shift factor (a_T) along the time scale (t):

$$D(t,T_0) = \frac{D(t,T)}{a_T} \qquad (1.5)$$

To illustrate the shifting process more clearly two individual creep curves are considered in Figure 1.6. The creep curves obtained at different temperatures are superposed by horizontal shifting along a logarithmic time scale.

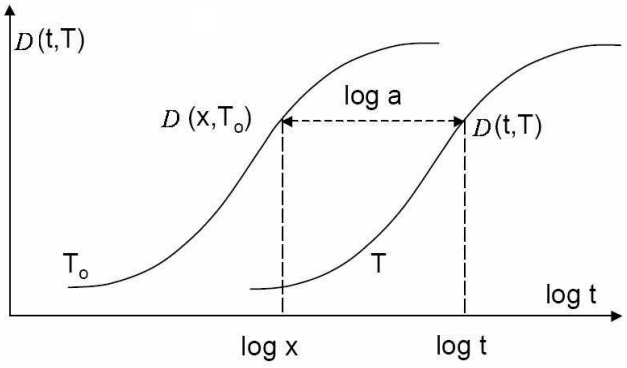

Figure 1.6: Scheme of the shift process according to TTS

The shift factors can be correlated with temperature via the Williams-Landel-Ferry (WLF) or the Arrhenius equations (e.g. [78-79]):

$$\log(a_T) = \frac{-C_1(T - T_0)}{C_2 + (T - T_0)} \tag{1.6}$$

where C_1 and C_2 are constants and T_0 is the reference temperature.

From the temperature dependence of the shift factor the activation energy (ΔH) can be the following Arrhenius equation – e.g. [80-81]:

$$\ln a_T = \frac{\Delta H}{R}\left(\frac{1}{T} - \frac{1}{T_0}\right) \tag{1.7}$$

where R is the universal gas constant.

Modeling approach

Polymeric materials exhibit behaviour that is dependent, at a given temperature, on both time and stress. For each load level, a different curve is obtained and thus different set of material parameters can be defined. Generally, the long-term creep behavior of material is predicted by some empirical models (Burgers model and Findley power law) [82]. These creep models proved to be successfully applicable for many polymers, therefore their applicability will be checked in this work.

Burgers model

The simplest way to simulate the viscoelasticity of a material is the use of mechanical analogies that include viscous (dashpots) and elastic elements (springs). The spectra once determined allow us the calculation of other viscoelastic functions which are obtained when the time history of excitation in the experiments is changed. A schematic representation of creep retardation spectrum of the spring-dashpot approach, being the sum of three parts, is detailed in Figure 1.7. This model is used to evaluate the effect of rubber particles and fillers in composites prepared by different methods. The creep experiment can be calculated from a discrete retardation spectrum of the Burgers model consisting of a Maxwell and a Kevin units connected in series (cf. Figure 1.7) by the equation [83]:

$$D(t) = D_0 + \Psi(t) + \frac{t}{\mu_0} \tag{1.8}$$

$$\Psi(t) = \sum_{k=1}^{N} D_k * \left[1 - e^{-t/\tau_k}\right] \tag{1.9}$$

where t is the time, D_0 is the instantaneous compliance, $\Psi(t)$ is equilibrium compliance part of creep compliance, μ_0 is viscosity and τ is different retardation times of the Kelvin unit D_k.

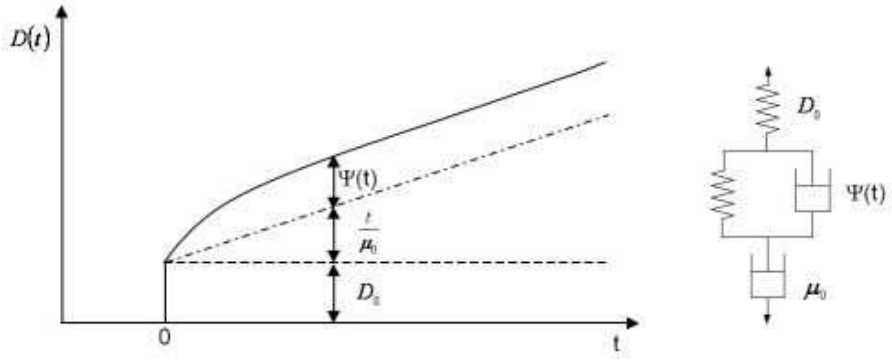

Figure 1.7: Schematic of the creep behavior and Burgers model

Power law

In order to simulate the creep behavior, several researchers have preferred to use the Findley power law model. Note that the related power function is given [e.g. 82, 84]:

$$D_F = D_{F0} + D_{F1} * t^n \qquad (1.10)$$

where n is a stress independent constant, D_{F0} is the time-independent compliance, and D_{F1} is the coefficient of the time-dependent term.

Curve fitting can be used for parameter estimation (for Eqs. 1.8 and 1.10) based on experimentally obtained creep curves. In fact, for the time frame corresponding to the test, the result of curve fitting will be satisfactory regardless of which equation is selected [85]. However, the predictions by the equations 1.8 and 1.10 for longer times will differ from one another. The creep behavior of semicrystalline polymers depends, among above factors, on the level of loading. It has been experimentally observed that under lower levels of loading the behavior is characterized by initial creep which decays with the time, and hence the viscoelastic behavior becomes elastic with time. This type of behavior can be well modelled using the Burgers approach with properly selected relaxation times.

In creep test under higher loads, the creep behaviour changes and strains continue to grow under these higher loads. The creep compliance does not approach an asymptotic value but grows continuously with the time. Therefore, the power law will better reflect actual physical behavior of the material at longer time [85-86].

Dynamic Mechanical Thermal Analysis

In addition of creep experiments, dynamic mechanical thermal analysis (DMTA) is quite common method understand better some of the added complications that arise from the time and temperature dependence of the modulus of viscoelastic materials. Usually, the viscoelastic behaviour can be determined by measuring the storage modulus and the loss modulus over a wide range of frequencies and temperatures. The storage modulus is proportional to the degree of elasticity of the system. The loss modulus is proportional to the dissipation or loss energy as heat in a cycle deformation, reflecting a certain degree of the viscosity of the system [87]. Figure 1.8 illustrates a schematic of dynamic experiment which shows graphically the nature of the two sinusoidal signals against time.

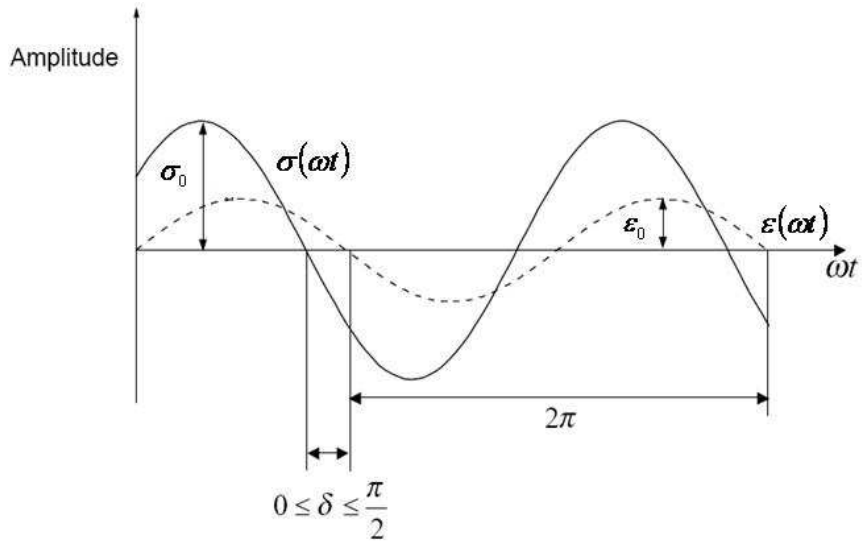

Figure 1.8: Schematic of the dynamic mechanical experiment

Consider the application of a sinusoidal strain, which can be presented by:

$$\varepsilon(t) = \varepsilon_0 \sin \omega t \tag{1.11}$$

where ε_0 is the maximum amplitude of the strain, ω is the angular frequency and t is time. The phase of the strain is arbitrarily set at zero, which can be done without loss of generality (perfectly elastic).

Tthe resulting stress σ(t) is given by:

$$\sigma(t) = \sigma_0 \sin(\omega t + \delta) \tag{1.12}$$

A complex Young's modulus (E*) reflects the contribution of both storage (E') and loss (E'') components to the stiffness of material, as follows:

$$E^* = \frac{\sigma_0}{\varepsilon_0} = E' + iE'' \tag{1.13}$$

According to Figure 1.8, the modulus at these two points can be calculated from equations 1.12 and 1.13. The storage modulus (E') gives directly:

$$E' = E^* \sin \delta \tag{1.14}$$

And in term of loss modulus (E''):

$$E'' = E^* \sin(\pi/2 + \delta) = E^* \cos \delta \tag{1.15}$$

The ratio of the loss modulus to the storage modulus is the tangent of the phase angle shift δ between the stress and strain vectors, thus:

$$\tan \delta = \frac{E''}{E'} = \frac{\sigma''}{\sigma'} \tag{1.16}$$

As Time-temperature-superposition (TTS) discussed in above creep analysis, in a thermorheologically simple material, the characteristic times are mutually proportional if all the elastic modulus show the same dependence on temperature. In other word, using the storage modulus E' as an example, and considering it as function of time changing of temperature is seen to be equivalent to apply the shift factor (a_T) to the time scale [e.g. 88].

$$a_T = \frac{E'(t,T)}{E'(t,T_0)} \tag{1.17}$$

Fitting the experimentally determined shift factors to a mathematical model permits the creation of a master curve in form of storage modulus vs. frequency. The shift factors are linked with temperature via the Williams-Landel-Ferry (WLF) equation (e.g. [78]), as follows:

$$\log(a_T) = \log\left(\frac{f}{f_0}\right) \tag{1.18}$$

2 Objectives of the study

The properties of thermoplastic-reinforced nanocomposite are mostly influenced by the state of agglomeration of the filler which is strongly affected by preparation methods. In this work the influence of the addition of nanoparticles and/or rubber particles on the properties of amorphous polystyrene (PS) and semi-crystalline polyoxymethylene (POM) are investigated.

The objectives of the present investigations are manifold:

- The primary objective is to prepare the composites of PS and POM using two different nanofillers, such as, Boehmite Alumina nanoparticles (25 and 220 nm) and Sodium fluorohectorite layered silicate. Two methods have been used for the preparation of composites, the first method is a discontinuous method involving direct melt compounding in a Brabender mixer, while the second is a continuous method, in which twin extruder is used.
- To investigate the effect of rubber latex which plays a dual role: first, to improve the dispersion of the fillers, and second, to improve the toughness of the formed composites.
- To study the microstructure of the composites formed.
- To study the effect of these fillers on the crystallization behavior of POM.
- To study the structure property relationships.
- To study the viscoelastic properties of the composites in the solid as well as melt state.
- To study the thermal stability of the composites.

Following techniques have been used to characterize the composites:

- The microstructure of the layered silicate nanocomposite is evaluated using X – ray diffraction.
- Dispersion of Alumina and layered silicate particles using Scanning Electron Microscopy and Transmission Electron Microscopy.
- Melting and crystallization is studied using Differential Scanning Calorimetry.
- Spherulitic morphology by Optical Microscopy.
- Viscoelastic properties in the solid state by Dynamic Mechanical Analyzer.

- Viscoelastic properties in the melt state by Advanced Rheological Expansion System.
- The thermal stability of the nanocomposites is evaluated using Thermogravimetric analysis.

Major aims of this work were to produce micro- and nanocomposites with both amorphous and semi-crystalline matrices and determine their structure-property relationships. In order to elucidate possible “nanoeffects” considerable attention was paid that the micro- and nanocomposites contain the same filler. The microcomposites were prepared by direct melt blending, while the nanocomposites by water mediated predispersion of suitable fillers (boehmite, fluorohectorite) followed by melt blending.

3 Experimental

3.1 Selection of Materials

3.1.1 Polymer Matrices

Granulated PS (Polystyrol 158 K Glasklar, BASF, Ludwigshafen, Germany) was utilized as polymeric matrix for PS/FH and PS/alumina composite systems. Its volumetric melt flow rate (MVR at 200 °C/5 kg) was 3 cm^3/10 min. The glass transition temperature (T_g) was 105 °C (measured by DSC).

PS latex with 50 wt.% dry content (Baystal SX 1160) was supplied by Polymer Latex GmbH (Marl, Germany). Note that this PS latex acted as swelling and dispersing agent for sodium fluorohectorite and alumina particles in the masterbatch production disclosed later. The PS structure is given in Figure 3.1.

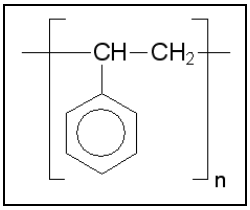

Figure 3.1: The molecular structure of PS

POM (Hostaform C 9021, Ticona GmbH, Frankfurt, Germany) was utilized as polymeric matrix for POM composite systems (cf. Figure 3.2). Its volumetric melt flow rate (MVR at 190 °C/2.16 kg) was 8 cm^3/10 min. The glass transition temperature (T_g) and melting temperature (T_m) was -63 °C (measured by DSC) and 166 °C (according to suppliers' information), respectively.

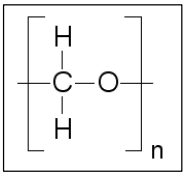

Figure 3.2: The molecular structure of POM

PU latex with 50 wt.% dry content (Acralen U 550) which has the particles in the size range 100 to 1000 nm (according to suppliers' information), was kindly supplied by Polymer Latex GmbH (Marl, Germany). PU structure is presented in Figure 3.3. Note that PU served for impact modification of POM.

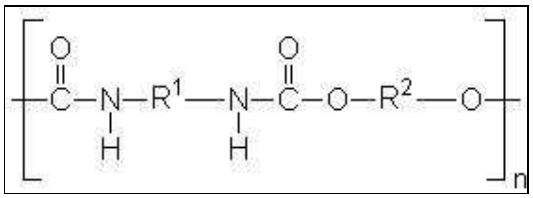

Figure 3.3: The molecular structure of PU

3.1.2 Nanofillers

Sodium fluorohectorite, denoted further on as FH (Somasif ME-100, Coop Chemicals, Tokyo, Japan) was used as reinforcement. FH prepared by heating talcum together with sodium hexaflorosilicate (Na_2SiF_6) (cf. Figure 3.4). This has an interlayer distance of 0.92 nm and a cation exchange capacity of 0.1 equiv/100g.

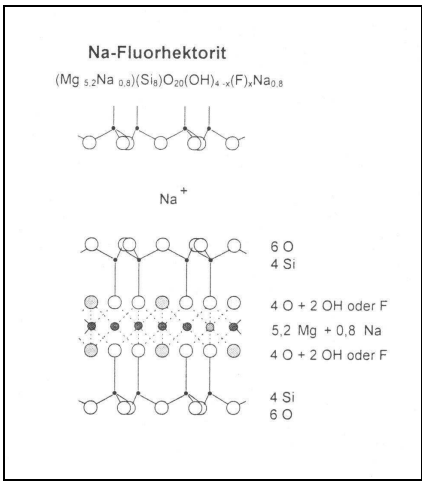

Figure 3.4: The molecular structure of sodium fluorohectorite

Two types of water dispersible boehmite alumina (Disperal® P2 and Dispal®11N7-80 of Sasol GmbH, Hamburg, Germany) served as fillers. The boehmite mineral has a layered structure displayed in Figure 3.5a. The layers are composed of edge-linked octahedrons of oxygen and hydroxide ions with an aluminum ion in the center (cf. Figure 3.5b). Their specifications are listed in Table 3.1.

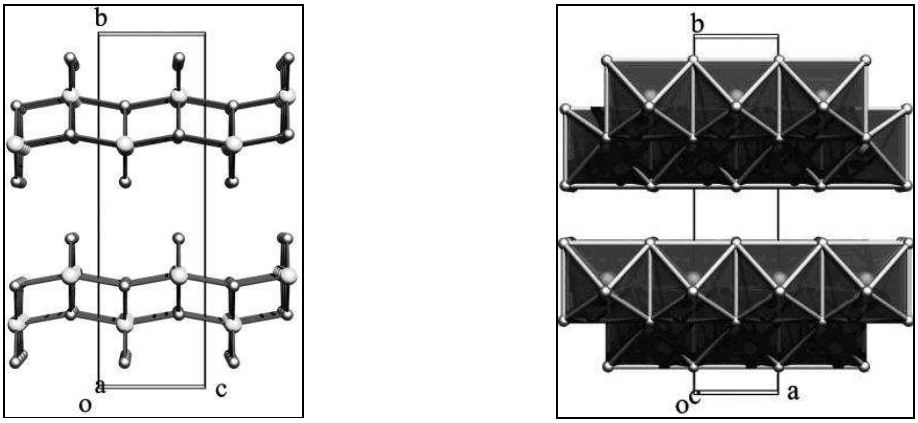

a) b)

Figure 3.5 Structure of the mineral boehmite. a) binding of atoms and b) linkage of AlO_6-octahedrons [89]

Table 3.1: Specification of the water dispersible boehmite aluminas as delivered by Sasol Germany GmbH

Characteristics/type	**Disperal® P2**	**Dispal® 11N7-80**
Al_2O_3 [%]	72	80
Na_2O [%]	0.002	0.002
NO_3 [%]	4.0	0.1
Loose bulk density [g/l]	850	620
Specific surface area [m^2/g]	260	100
Mean powder particle size [µm]	45	40
Mean dispersed particle size in water [nm]	25	220

3.2 Preparation and Processing of Composites

3.2.2 Discontinuous Manufacturing

PS system

PS/FH and PS/alumina nanocomposite systems were prepared by two different methods: a) direct melt compounding (DM) and b) melt compounding using a masterbatch produced from PS latex containing FH or alumina particle (masterbatch technique, MB). The molecular characteristics of the PSs in latex and granulate forms, respectively, were not determined – however they were similar according to suppliers' information. The FH content in the corresponding composites was set for 4.5 and 7 wt.%, respectively. The alumina content in the corresponding composites was set for 4.5 wt.%. Melt mixing occurred in laboratory kneader (Type 50 of Brabender, Duisburg, Germany) at T= 180 °C and rotor speed of 60 rpm. The FH or alumina powder (DM) or FH or alumina -containing PS masterbatch (MB) was introduced after melt mastication (granulates plus dried latex) for 2 min. The duration of the melt mixing for both direct and masterbatch techniques was 6 min. The PS composition and designation of the compounds studied are given in Table 3.2.

As the molecular characteristics of the PS from the latex and granules may be different, attention was paid to set their composition ratio equal in the unfilled and filled composites to be compared. A scheme of the masterbatch technique of PS composite systems is given in Figure 3.6. First, an aqueous FH slurry (10 wt.%) was produced at ambient temperature through mechanical stirring for 5 hours. Similarly, an aqueous alumina slurry (10 wt.%) was prepared at ambient temperature through mechanical stirring for 30 minutes. Then the PS latex was introduced in this slurry and stirred for further 30 min. The resulting slurry was poured in a framed glass plate and dried for 48 h at room temperature and for 12 h at 60 °C. Note that this condition does not produce a void-free film from PS latex as the glass transition temperature (T_g) of PS is much higher. However, a void-free film was no prerequisite owing to the subsequent melt mixing process. For reference purpose a PS containing 25 wt.% PS from the latex was selected. This composition considers the latex-derived PS content of the composites. For reference purpose a PS containing 25 wt.% PS from the latex

was selected. This composition considers the latex-derived PS content of the composites.

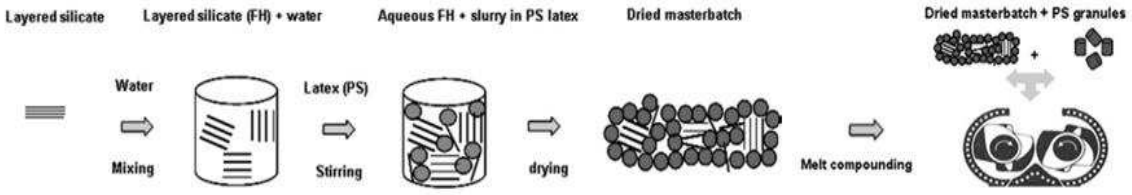

Figure 3.6: Scheme of the preparation of PS/FH nanocomposites via the masterbatch method

POM system

POM/PU/alumina ternary nanocomposites were prepared by two methods: a) direct melt compounding (DM), and b) melt compounding using a masterbatch produced from PU latex containing alumina particle (MB). The alumina and the PU content in the corresponding composites was set for 3 wt.% and 10 wt.%, respectively. Melt mixing occurred in the same laboratory kneader at T= 190 °C and rotor speed of 60 rpm. The alumina powder (DM) or alumina-containing PU masterbatch (MB) was introduced in the POM system after melt mastication of the latter for 2 min. The duration of the melt mixing for both DM and MB was 6 min. POM/PU binary composites were also produced by direct melt mixing by incorporating dried PU. The POM composition and designation of the compounds studied are given in Table 3.3.

A scheme of the masterbatch technique of POM composite systems is given in Figure 3.7. The masterbatch was produced as described below. First, an aqueous alumina slurry (10 wt.%) was prepared at ambient temperature through mechanical stirring for 30 minutes. Then the PU latex was introduced in this slurry and stirred for further 30 min. The resulting slurry was poured in a framed glass plate and dried for 5 days at room temperature (RT). This resulted in a PU film as the glass transition temperature (T_g) of PU is much lower than RT.

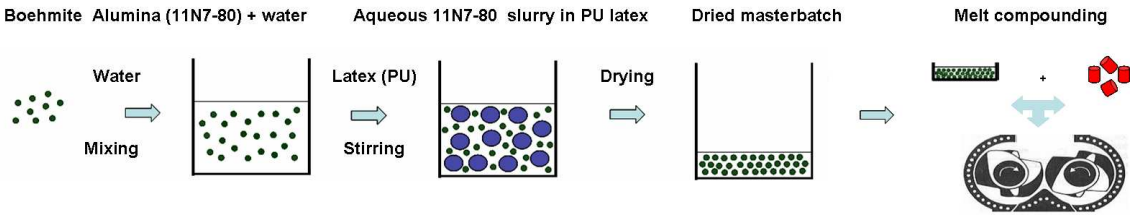

Figure 3.7: Scheme of the preparation of POM/PU/alumina composites via the masterbatch method

The compounds, after melt mixing in the Brabender kneader, were compression molded into 1 mm thick sheets at T= 200°C, using a hot press (EP-Stanzteil, Wallenhorst, Germany).

Table 3.2: Recipe and designation of the PS-based systems

Sample Designation	Masterbatch technique (MB)			Direct melt mixing (DM)		
	FH (wt.-%)	11N7-80 (wt.-%)	P2 (wt.-%)	FH (wt.-%)	11N7-80 (wt.-%)	P2 (wt.-%)
PS	-	-	-	-	-	-
PS/FH(4.5)=>MB	4.5	-	-	-	-	-
PS/FH(4.5)=>DM	-	-	-	4.5	-	-
PS/FH(7)=>MB	7	-	-	-	-	-
PS/FH(7)=>DM	-	-	-	7	-	-
PS/11N7-80(4.5)=>MB	-	4.5	-	-	-	-
PS/11N7-80(4.5)=>DM	-	-	-	-	4.5	-
PS/P2(4.5)=>MB	-	-	4.5	-	-	-
PS/P2(4.5)=>DM	-	-	-	-	-	4.5

Table 3.3: Recipe and designation of the POM-based systems

Sample Designation	PU content (wt.-%)	Masterbatch technique (MB)		Direct melt mixing (DM)	
		11N7-80 (wt.-%)	Alumina content (wt.-%)	11N7-80 (wt.-%)	Alumina content (wt.-%)
POM	-	-		-	
POM/PU (10)	10	-		-	
POM/PU(10)/11N7-80(3)=>MB	10	3		-	
POM/PU(10)/11N7-80(3)=>DM	10	-		3	

3.2.2 Continuous Manufacturing

In this method, different PS and POM–based composite systems were prepared continuously in a twin-screw extruder –cf. Table 3.4. For compounding of the composites a conventional mixing screw was used the design of which is given in Figure 3.8. First, alumina particles were dispersed in water at ambient temperature under continuous mechanical stirring for 30 minutes to obtain the aqueous alumina slurry, in which the alumina content was 30 wt.%. The rubber particle and/or alumina content in the corresponding composites was set for 10 and 3 wt.%, respectively. POM and PS–based composite systems were supplied so that sum totals were set to 10 kg/h. PU latex and aqueous alumina slurry were injected into the extruder at a rate of 2 L/h, 1 L/h, respectively, using pump.

Online melt compounding process

A co-rotating twin-screw extruder ZSK 25 P8 (Werner & Pfleiderer GmbH & Co.KG) was used to prepare nanocomposites. The extrusion temperature was selected between 150° C and 190 °C systems from hopper to the die for all composite (barrels section 1: 150 °C and section 2-9: 190 °C). Figur e 3.8 shows a schematic picture of the extruder configuration for preparing the composites using the water injection system.

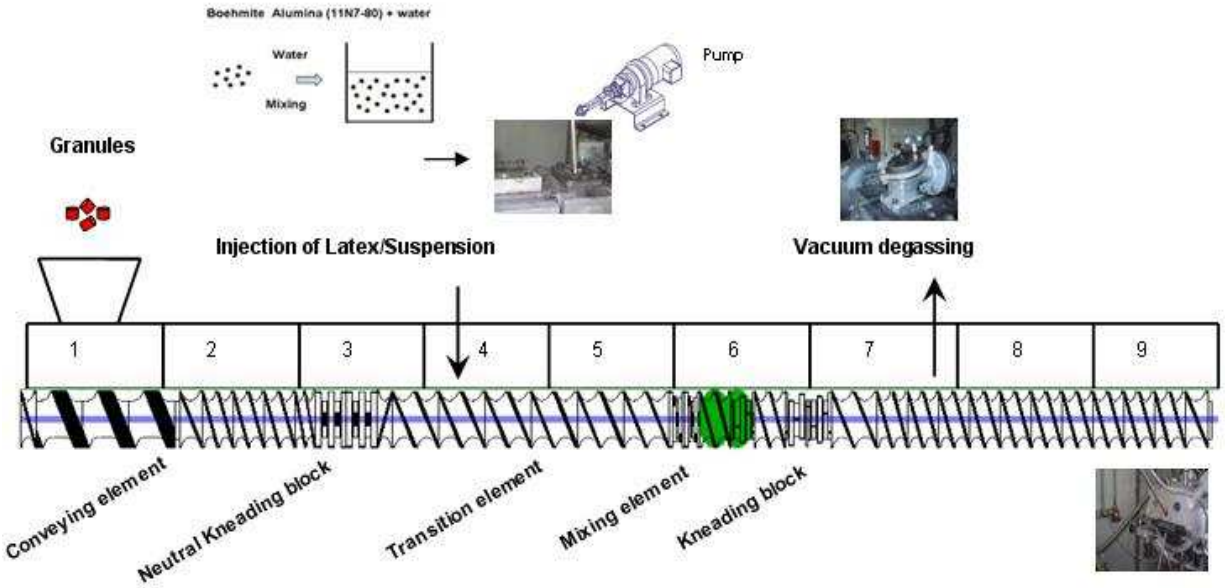

Figure 3.8: Twin-screw configuration and extruder barrels sections used to produce polymer/nanocomposites continuously

Polymer pellets were charged in feeder in the first zone of the extruder. As shown in Figure 3.8, the PS or POM composites and POM/PU blend were prepared by using a pump: the resulting alumina slurry/rubber latex was injected in the melting zone into the extruder. A second pump was used to produce the POM/PU/alumina ternary composite, whereby the PU latex was introduced also in the barrels section 4. The rotation speed of screw was fixed at 200 and 150 rpm for PS and POM, respectively. The water was eventually degassed in the transport zone (barrels section 7-9) of the screw and the evaporation was completed using a vacuum pump. The strands that were obtained were cooled in a water bath, pelletized with a cutter and dried for 24 h at 70 °C in a thermostatic oven.

Injection molding process

Granulates obtained from the continuous process was used to produce standard tensile dumbbell-shaped specimens (160x10x4 mm^3 (width x length x thickness), according to the German standard of DIN-ISO-527) by an automatic injection molding machine (Alburg Allrounder 320S, Lossburg, Germany). The barrel temperature of the injection molding machine was set at 200 °C and the mold temperature at 90 °C and 50 °C for POM and PS series, respectively. The injection pressure was kept constant (700 bar) and for the injection speed of 55 cm^3/s was selected. The cooling time was 20 sec. before ejection of specimen.

Table 3.4: Recipe and designation of the POM and PS -based systems

Sample Designation	PU content (wt.-%)	Continuous technique (CT)		Direct melt mixing (DM)	
		11N7-80 Alumina content (wt.-%)		11N7-80 Alumina content (wt.-%)	
POM	-	-		-	
POM/PU(10)	10	-			
POM/11N7-80(3)	-	3		-	
POM/PU(10)/11N7-80(3)	10	3		-	
PS	-	-		-	
PS/11N7-80(3) =>CT	-	3		-	
PS/11N7-80(3) =>DM	-	-		3	

3.3 Structural Characterization

3.3.1 Scanning Electron Microscopy (SEM)

The fracture surfaces of PS specimens were subjected to SEM inspection in a JSM 5400 device of Jeol Ltd (Tokyo, Japan). The surfaces were gold coated prior to SEM performed at 25 kV acceleration voltage. For POM specimens were subjected to SEM inspection in a high magnitude Supra™ 40VP SEM (Carl Zeiss GmbH, Oberkochen, Germany). The surface of POM matrix was carbon coated prior to SEM inspection performed at low acceleration voltage. Quantitative elemental analysis in selected spots of the surface was done by electron dispersion analysis by X-rays (EDAX). For that purpose the surface was coated by carbon and the SEM operated at 15 kV acceleration voltage.

3.3.2 Transmission Electron Microscopy (TEM)

TEM measurements were carried out with a Zeiss LEO 912 Omega transmission electron microscopy (Oberkochen, Germany) applying an acceleration voltage of 120 kV. Thin sections (ca. 50 nm) were cut at room temperature with a Diatome diamond knife (Hatfield, PA, USA) using an Ultracut E microtome (Reichert and Jung, Vienna, Austria).

3.3.3 Atomic Force Microscopy (AFM)

A Nanoscope III AFM (Digital Instruments, Santa Barbara, CA, USA) equipped with a microfabricated silicon cantilever with an integral tip was used. AFM images were taken from the surface of compression molded specimens. The specimens were molded by sandwiching the corresponding polymer/composite film between two glass plates in order to get a smooth surface. The surface profile was scanned by AFM in the tapping mode, and the related amplitude- and height-contrast images captured. Commercial silicon cantilever (Pointprobe® NCH) with nominal tip radius of less than 10 nm (120 µm cantilever length, 4 µm thickness, 30 µm width and spring constant at 42 Nm^{-1} of Nanosensors Company) was employed under its fundamental resonance frequency of about 330 kHz. The scan rates were set at 0.5 Hz.

3.3.4 Polarized light Microscopy (PLM)

The spherulite growth was observed by polarized light microscopy. Samples were isothermally crystallized in a hot stage (THMS 600/S, Raczek Analysentechnik, Wedemark, Germany). Thin films with a thickness of 20-30 micron were used. The film was melted at 200 °C for 1 min and then cooled to the isothermal crystallization temperature (T=148 °C) where it was hold for 60 min.

3.3.5 X-ray Diffraction (XRD)

XRD spectra in both reflection (FH powder and FH/water slurry) and transmission mode (compression molded nanocomposite sheets) were collected on a D500 Siemens (Karlsruhe, Germany) diffractometer, operating at 40 kV, 30 mA using Cu K_α radiation and a secondary beam graphite monochromator. The spectra were recorded in the 2θ-range from 1.2^0 to 10^0 in steps of 0.05^0 and at a counting time per step of 10 s.

3.4 Thermal and Thermo-mechanical Characterization

3.4.1 Differential Scanning Calorimetry (DSC)

Differential scanning calorimetry traces were recorded on a Mettler Toledo (Giessen, Germany), DSC 821 device in the temperature range from -100 °C to 200 °C at a heating and cooling rate of 10 °C/min. The mass of samples was cut in the range of 10-15 mg. The crystallinity (X_c) of POM was calculated from the following equation:

$$X_c = \frac{\Delta H_m}{\left(\Delta H_m^0\right)} * 100\% \qquad (3.1)$$

where ΔH_m is the melt enthalpy of the POM in the sample (i.e. net POM content considered), ΔH_m^0 is the theoretical enthalpy of POM for X_c =100% (186 J/g), as reported in Ref. [37].

3.4.2 Heat Distortion Temperature (HDT)

The heat distortion temperature was determined in three point bending mode using the same DMTA device. The stress applied was 0.46 MPa and the heating rate was set for 2 °C/min (similar to ASTM D 648). The sample dimensions were 60x12x3 mm^3 (width x length x thickness).

3.4.3 Thermo Gravimetric Analysis (TGA)

Thermogravimetric analysis was performed on a TG50 Mettler Toledo device (Giessen, Germany). TGA experiments were conducted in the temperature range from 25 to 600 ℃ under oxygen at a heating rate of 10 °C/ min and the weight loss was monitored.

3.4.4 Dynamic Mechanical Thermal Analysis (DMTA)

Dynamic mechanical analysis of PS specimens was made in single cantilever mode at 1 Hz frequency using a DMA Q800 apparatus (TA Instruments, New Castle, USA). The storage- und loss modulus (E', E'') along with mechanical loss factor (tan δ) were determined as a function of the temperature (T= -50 °C…+130 °C). Due to different linear viscoelastic range of POM and PS-based composite systems, the strain applied of PS was 0.01 % and the heating rate was set for 3℃/min. The sample dimensions were 10x35x3 mm^3 (width x length x thickness). POM specimens were tested in tensile mode at 1 Hz frequency in the temperature range of T= -100 °C…+150 °C using the same apparatus. The strain applied of POM was 0.1 % and the heating rate was set for 3° C/min. The specimen was a dumbbell-shaped type (S3A according to DIN 53504).

3.5 Mechanical Characterization

3.5.1 Tensile Test

Tensile tests were performed on dumbbell-shaped specimens: S3A type according to DIN 53504 for discontinuous by produced specimens and according to DIN-ISO-527 for continuous by produced specimens on a Zwick 1474 universal testing machine (Ulm, Germany). Tests were run at RT with v=2 mm/min crosshead speed and the related modulus, strength and elongation at break values were determined.

3.5.2 Impact Test

Impact test was performed on an instrumented impact tester (AFS-MK fracto scope of Ceast, Torino, Italy) according to the standard ISO 179. Striker energy of 4 J, testing time of 4~8 ms and indicate velocity of 2.9 m/s were set. The PS-based specimens were unnotched rectangular bars (4x10x80 mm^3, width x length x thickness). For POM-based specimens, notched rectangular bars were chosen. The notch depth was 1 mm. Measurements were run at RT on at least six specimens.

3.5.3 Creep Experiment

Short-term creep tests of PS composite systems were made in tensile mode at different temperatures using the DMTA Q800 apparatus. The creep- und recoverable compliance were determined as a function of the time (t_{creep} = 30 min. and $t_{recovery}$ = 120 min.). The tensile stress applied was 4 MPa (at 0.5 % strain). This was derived from a test series checking the presence of linear isochronous deformation. The specimens' dimensions were 9x35x0.4 mm^3 (width x length x thickness). The temperature dependence of the creep response of the PS and its composites was studied. In order to get a clearer picture on the creep response of the PS/alumina composites the TTS principle was adopted for short term creep tests performed at various temperatures. The tensile stress applied here was 3 MPa. The temperature dependence of the creep response of the PS and its composites was studied in the range from 20 to 75 °C. In this temperature range isothe rmal tests were run on the same specimen by increasing the temperature stepwise by 5 °C. Prior to the creep measurement (duration 15 min) the specimen was equilibrated for 5 min at each temperature. For POM composite systems were determined as a function of the time (t_{creep} = 60 min and $t_{recovery}$ = 120 min). The applied tensile stress was 6 MPa (at 0.35 % strain). This was derived from a test series checking the presence of linear isochronous deformation. The test was performed on dumbbell-shaped specimens (5B type according to DIN-EN ISO 527). The temperature dependence of the creep response of the POM and its composites was studied in the range from -50 to 80 °C.

Long-term creep tests were performed on POM/PU/alumina ternary systems produced by DM and advanced masterbatch technique (MBa). Recall that during production of MBa is similar in Figure 3.6, but the aqueous alumina slurry in PU latex was introduced directly in the POM melt when masticating in the laboratory kneader. Long-term creep tests were made in tensile mode at 50 °C using the creep rupture Test Machine with double lever system Model 2002 (Coesfeld GmbH, Dortmund, Germany). The static loads were set as 6 MPa, 15 MPa and 20 MPa. A gauge length of 30 mm was marked on each specimen, and the elongation was monitored by a video camera, which was equipped with a program-controlled step motor and connected to a computer imaging analysis system during the whole period of creep testing.

3.6 Rheology

A controlled strain rheometer (ARES of Rheometric Scientific, NJ, USA) was utilized in parallel plate configuration (diameter of the plate: 25 mm) to measure the melt rheology of the PS and POM composite systems at T= 180 °C and 190 °C, respectively. Oscillatory shear measurements were performed on each sample by setting the strain amplitude for 1 %. This was derived from a strain sweep test series checking the presence of the linear viscoelastic region. The gap between the plates was 2 mm.

3.7 Dielectric Characterization

Broadband dielectric measurements were performed in the frequency range of 10^{-3} – 10^{7} Hz, by means of Alpha-N Frequency Analyzer, supplied by Novocontrol Technologies GmbH (Hundsangen, Germany) at room temperature. The employed test cell was a two electrodes gold-coated plate capacitor, BDS 1200, supplied also by Novocontrol, which was suitably shielded.

4 Result and Discussion

4.1 Discontinuously Produced Micro-and Nano Composites

4.1.1 Polystyrene/Fluorohectorite Composites

4.1.1.1 Structure

Figure 4.1 shows that the mean PS particle size is at ca. 200 nm and the particles are present in a very narrow distribution. Figure 4.1b informs us about the dimension of the platy FH. Note that the lateral dimension of the FH platelets may reach 1 µm which corresponds to an aspect ratio of greater than 1000. The layer thickness of FH is less than 1 nm. Figure 4.1b also displays that the FH platelets are likely peeled away from each other supporting that their intergallery space was swollen in water.

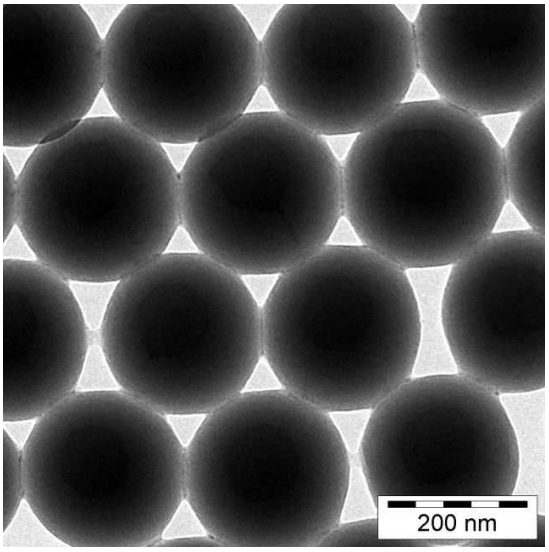

a)

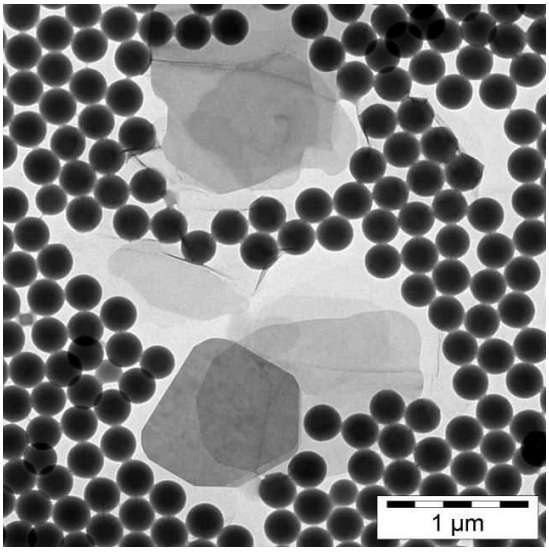

b)

Figure 4.1: TEM pictures of (a) PS latex and (b) PS latex/FH slurry after drying of the latex on TEM grids

To get information about the water swelling of the FH, XRD spectra were taken on powder samples containing different amounts of water. The latter was determined gravimetrically after drying the samples at T=85 °C for constant w eight.

The XRD spectra in Figure 4.2 evidence, in fact, that water acts as “swelling agent” for FH. It is interesting to note that FH populations with different interlayer distance are present at the same water content. This may be due to several effects (structural inhomogeneity of FH, water diffusion in different FH stacks and agglomerates, no equilibrium stage) which were, however, not studied in this case.

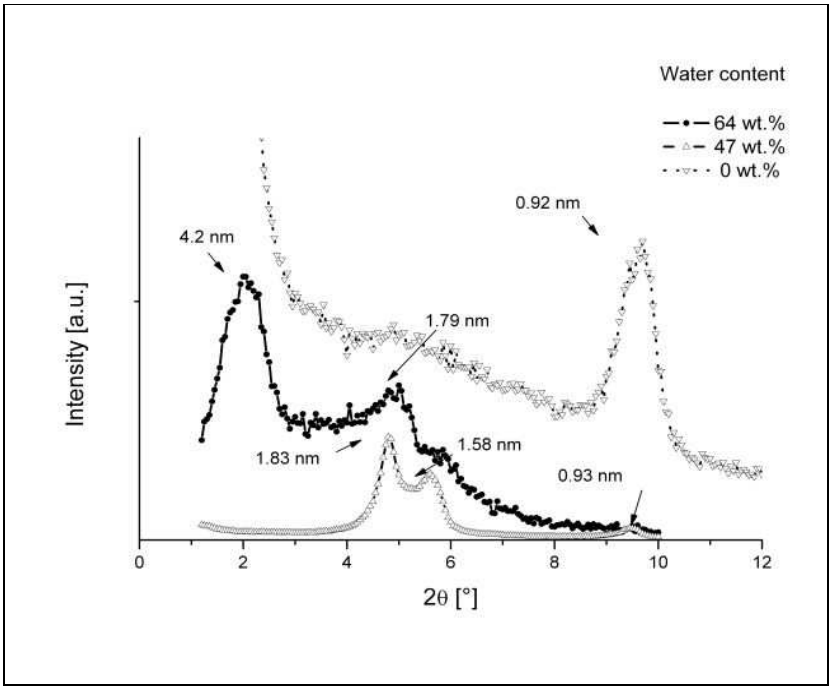

Figure 4.2: XRD spectra of FH as a function of its water content. The spectra were taken in reflection mode

XRD spectra registered on the differently produced PS composites are shown in Figure 4.3. One can clearly recognize that direct melt compounding did not result in a nanocomposite, as the change in the intergallery distance (d spacing) of FH is negligible (0.96 instead of 0.92 nm). This finding is in agreement with literature results (e.g. [55]). The compound produced by the masterbatch technique has FH populations with different intercalations (2.80, 1.22 and 1.01 nm). Considering the fact that the masterbatch itself contained intercalated FH (d=1.22 nm – cf. Figure 4.3) one can conclude that during its melt mixing with the PS granule both further intercalation (d=2.8 nm) and confinement (d=1.01 nm) occurred. The latter can be assigned to

some reordering of the FH layers during hot pressing. This suggestion is in accord with experimental results achieved mostly on rubbers (e.g. [90]).

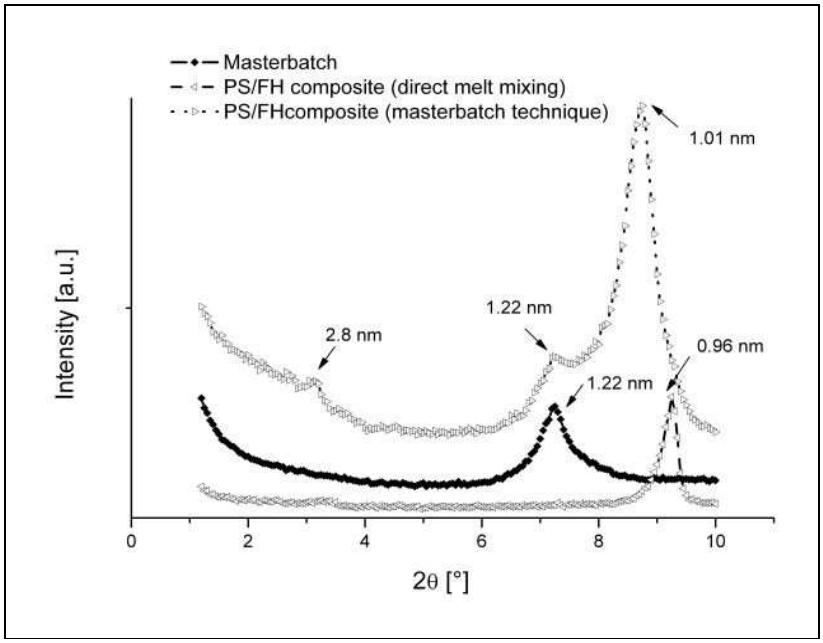

Figure 4.3: XRD spectra of PS/FH nanocomposites produce by various methods

The course of the XRD traces in the low scattering angle range hints for possible FH exfoliation in the masterbatch and related PS nanocomposite in contrast to the direct melt compounded version. The TEM pictures in Figures 4.4 and 4.5 corroborate this presumption. The FH stacks are hardly delaminated when the composite (which should be termed correctly as microcomposite) is produced through melt blending – cf. Figure 4.4. The FH layers are far better delaminated and dispersed when the nanocomposite has been produced by the masterbatch method (cf. Figure 4.5). Pronounced bending and undulation of the FH layers suggest that the platelets are well separated (the corresponding stacks are composed of few silicate layers). The TEM pictures in Figure 4.5 clearly show that the FH layers are mostly intercalated in the related nanocomposite.

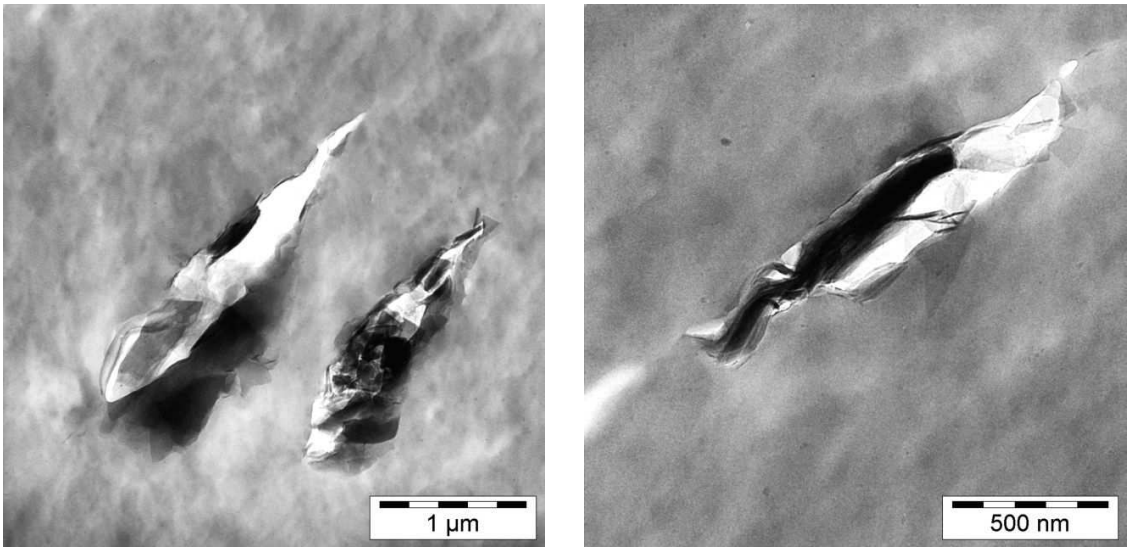

a) b)

Figure 4.4: Characteristic TEM pictures of a PS microcomposite produced by direct melt compounding. The FH content was 4.5 wt.%

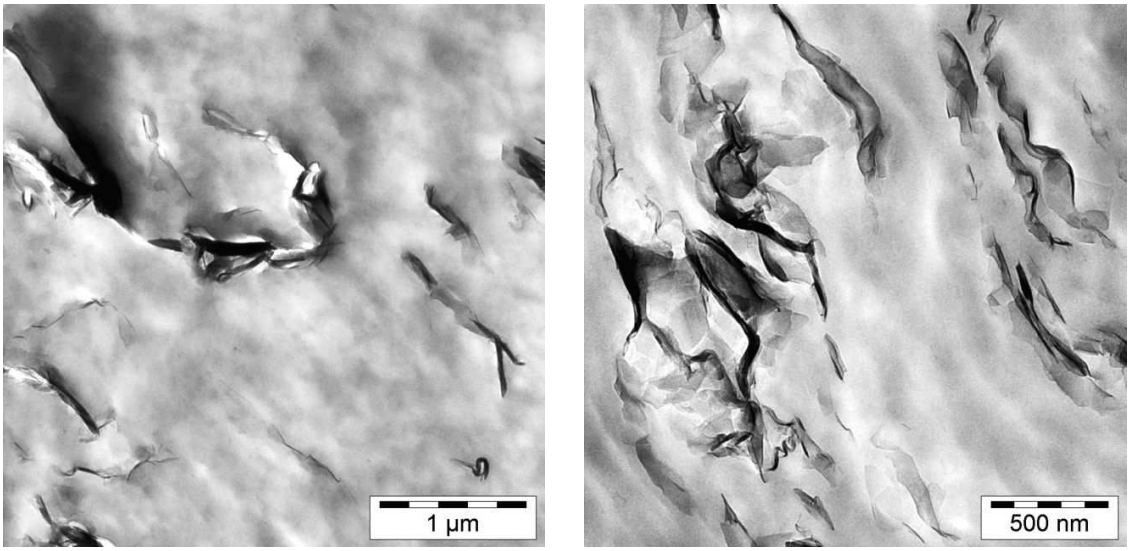

a) b)

Figure 4.5: Characteristic TEM pictures of a PS nanocomposite produced via the masterbatch technique. The FH content was 4.5 wt.%

SEM pictures taken from the fracture surfaces of tensile loaded specimens give further insight in the FH dispersion. Nevertheless, the difference in the FH dispersion in the composites produced by the methods chosen is obvious in Figure 4.6. The FH platelets are far better dispersed in the PS when prepared via the masterbatch instead of the direct melt mixing technique. The well dispersed FH layers trigger some microductile deformation of the nanocomposite compared to the microcomposite in which the large FH particles induce brittle fracture with voiding.

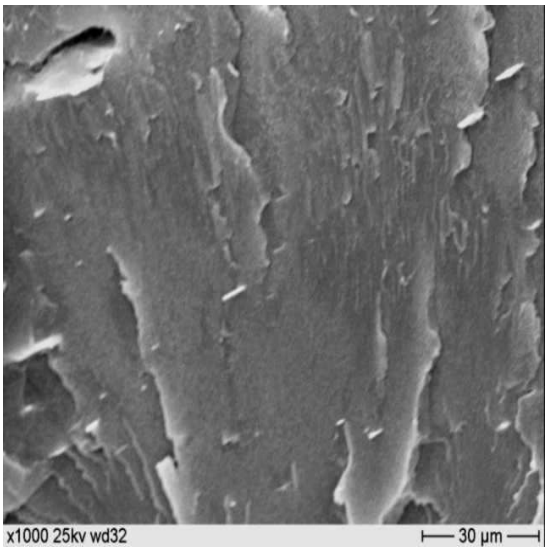

a)

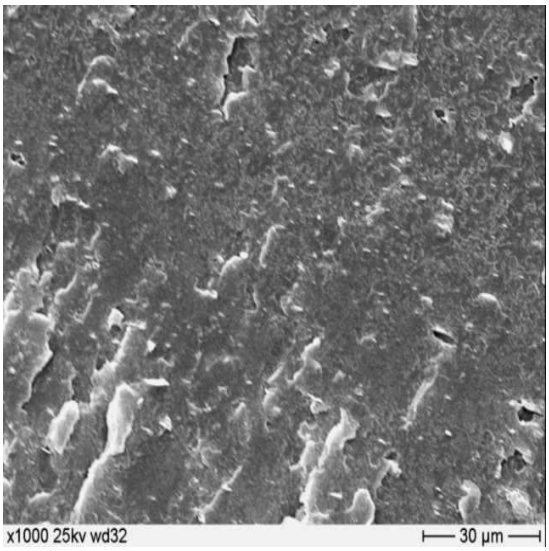

b)

Figure 4.6: Scanning electron microscopy pictures of the tensile fracture surfaces of composites produced by (a) DM and (b) MB

It is well known that “phase imaging” AFM is suitable tool to distinguish between the FH particles and the matrix polymer. Figures 4.7a-4.7b show the “AFM” surface morphology of AFM investigations of PS/FH composites prepared by DM and MB, respectively. Similar to SEM (cf. Figure 4.6) one can observe for larger FH agglomerates after DM compared to the MB. During the section analysis a line was laid over the scanned image to detect the FH particles emerging from matrix plane. The particles proved to be in micro- and nanoscaled when produced by DM and MB, respectively. In order to confirm the FH dispersion of the AFM samples were coated by carbon and subjected to EDAX analysis. Figure 4.8a-4.8b show SEM images of the corresponding composites. In selected spots of the samples (1, 2) as indicated in Figure

4.8 elemental analysis was done. EDAX revealed the major constituents of FH (viz. Na, F, Mg, Si) for the spot 1 whereas mostly carbon (C) was found for spot 2. These findings confirm that the particles emerging from the matrix during AFM were FH stacks, in fact.

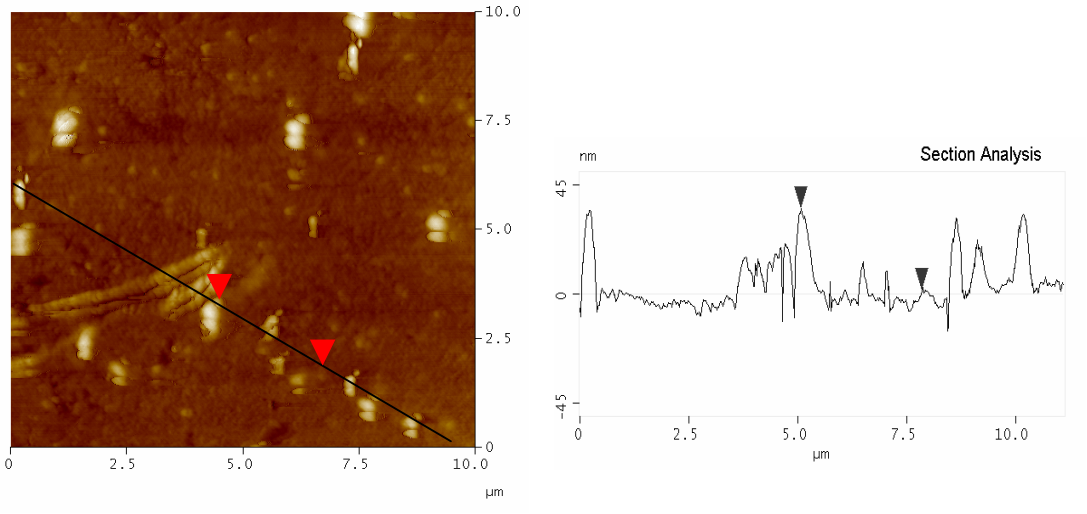

a)

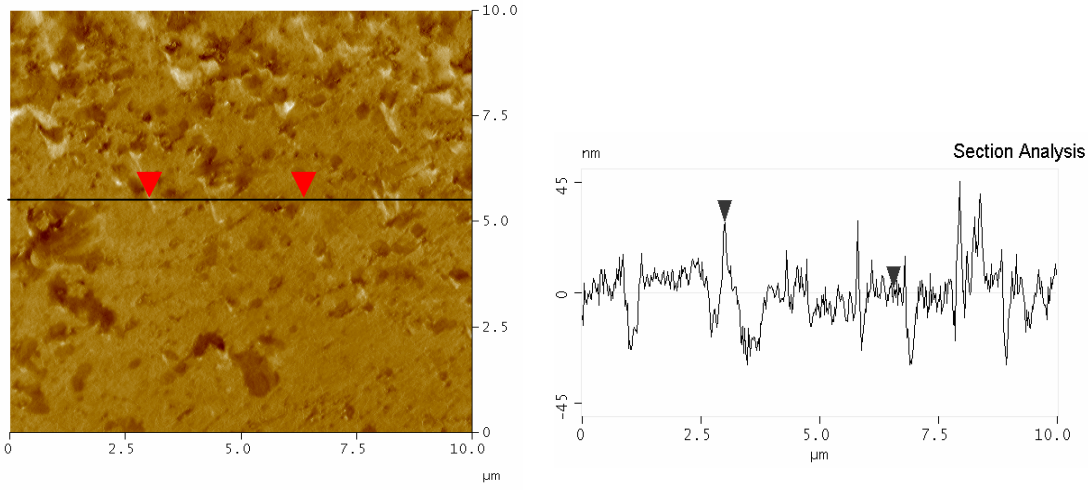

b)

Figure 4.7: AFM pictures taken from the surfaces of the composites produced by DM (a) and MB (b)

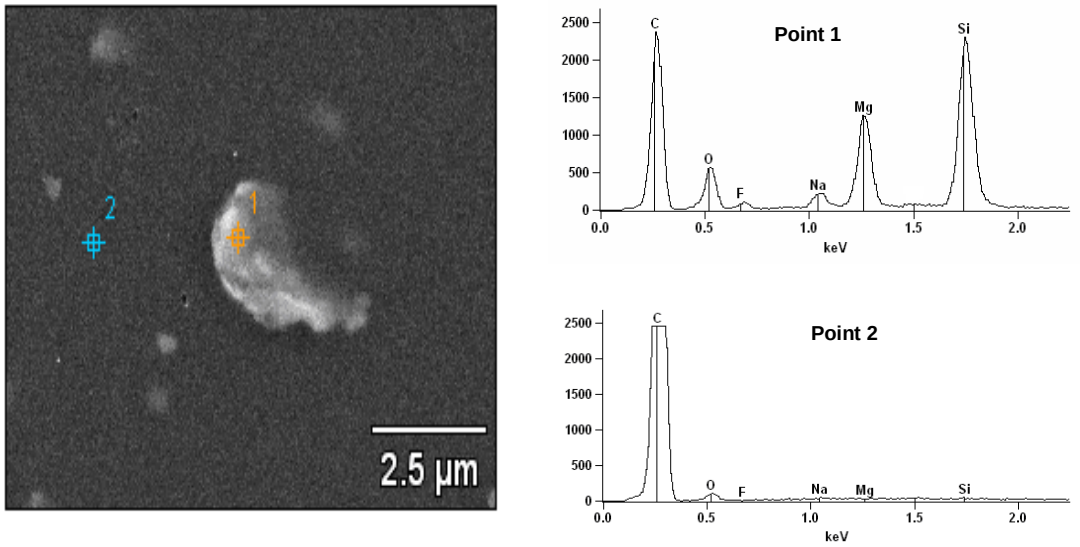

a)

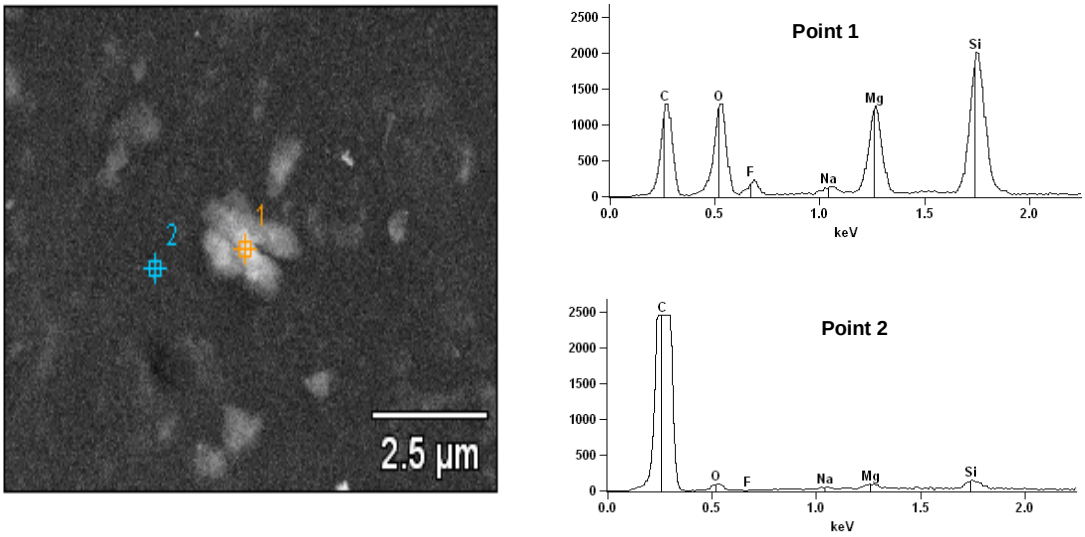

b)

Figure 4.8: EDAX pictures taken from the surfaces of the composites produced by DM (a) and MB (b)

4.1.1.2 Thermal Mechanical Properties

The difference in the FH dispersion is well reflected in the dynamic-mechanical and tensile behaviors as shown below. Figure 4.9 depicts the storage modulus (E') and mechanical loss factor (tan δ) as a function of temperature for the composites produced by various methods and containing different amounts of FH. Note that incorporation of FH in PS resulted in a pronounced stiffness enhancement below the T_g. This reinforcing effect was accompanied with a shift in the T_g towards higher temperature which is in line with the expectation (formation of an interphase with reduced molecular mobility). It is also well resolved that the stiffness of those composites which were prepared by DM is always inferior to those produced by the MB. This can be explained by considering the dispersions of the FH platelets in the related composites as discussed earlier.

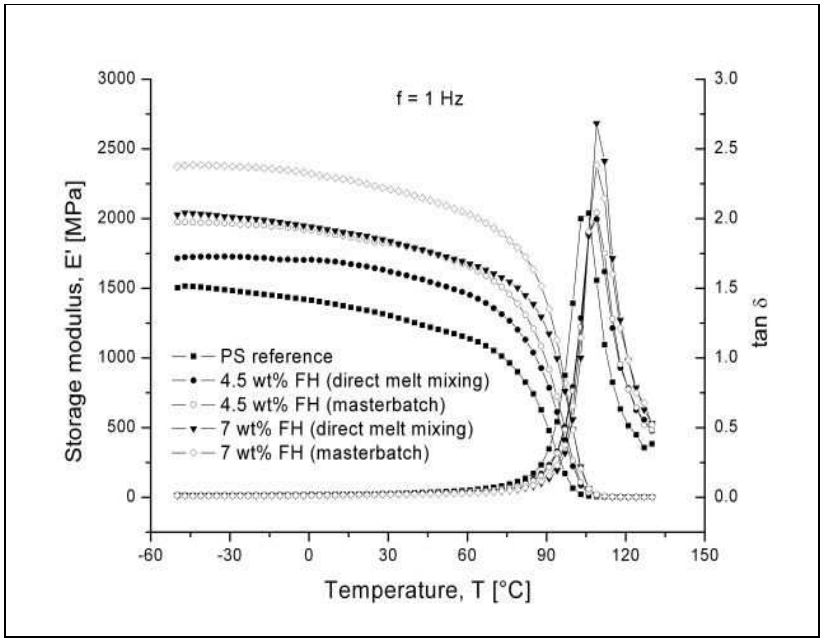

Figure 4.9: Traces of the storage modulus (E') versus the temperature and the mechanical loss factor (tan δ) versus the temperature for PS/FH composites produced by various methods

4.1.1.3 Tensile Properties

The tensile mechanical data are listed in Table 4.1. These data indicate that the improvement in the stiffness and strength was achieved at the cost of the ductility (elongation at break). However, the dispersion state of the FH strongly affected the tensile mechanical response. Intercalation/exfoliation of FH enhances the stiffness and strength and reduces the ductility loss of the related nanocomposites at the same time. Large, poorly dispersed FH particles in the melt mixed "microcomposites" act as stress concentrators and cause premature failure accompanied with low elongation at break values. The fracture surfaces of the dumbbells show characteristics of brittle fracture (cf. Figures 4.6a and b). The dispersion quality is the major reason for the difference in the related ductility values in Table 4.1.

Table 4.1: Tensile mechanical characteristics of the PS reference and FH-reinforced PS composites prepared by various methods

Property	**Material**				
	PS reference	Masterbatch technique		Direct melt mixing	
		PS/4.5wt% FH	PS/7wt% FH	PS/4.5wt% FH	PS/7wt% FH
Tensile strength [MPa]	27 ± 0.9	39±0.7	41±4	33±1.5	35±5.3
Tensile modulus [MPa]	3026±268	4546±173	5440±258	3667±146	4306±203
Elongation at break [%]	5.7±0.9	1.9±0.4	1.2±0.2	0.8±0.04	0.7±0.06

4.1.1.4 Viscoelastic Behavior

The creep curves at 23 °C of PS reference are shown in Figure 4.10a for 4 values of the applied stress. These curves were registered in order to check whether linear viscoelasticity prevails in the applied stress range. An isochronous stress-strain curve was constructed based on the measured strain at various stresses as a function of time. Figure 4.10b shows the stress-strain data after 30 minutes for the PS reference at T=23 °C. As Figure 4.10b, confirmed the presence of linear viscoelasticity, all PS specimens in the subsequent tests were subjected to 4 MPa stress and the strain was recorded as a function of time.

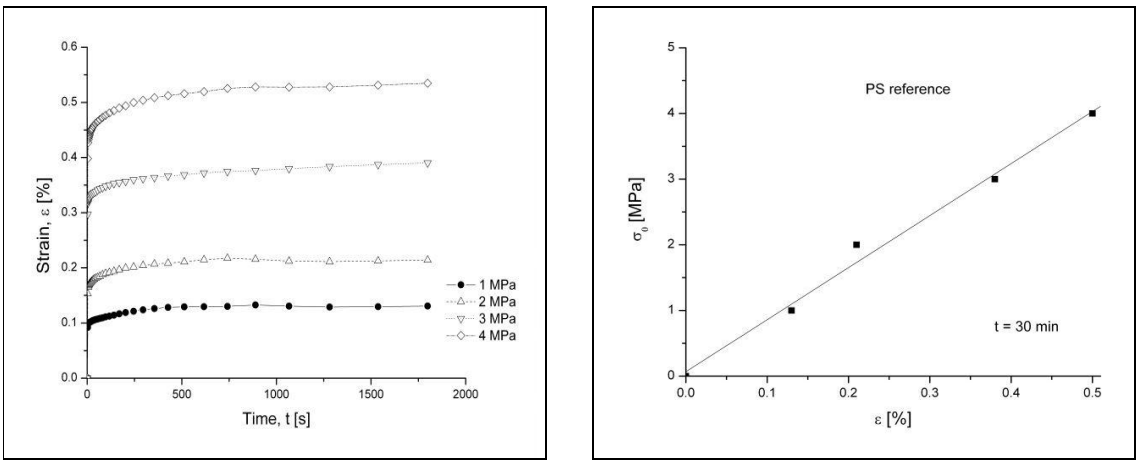

a) b)

Figure 4.10: Creep strain vs. time traces of various stress and the corresponding isochronous stress-strain curve for the PS reference

Figure 4.11 displays the creep compliance values for the PS reference and its composites produced by DM and MB methods. The shape of the creep curves of the composites is very similar to that of the PS reference, but their creep compliance values are much smaller compared to the PS reference. For the composites containing 4.5 wt.% FH for example the creep compliance was reduced by ~ 40 % and 10 % compared to the PS reference when produced by the MB and DM, respectively. The creep compliance values of the composites reflect the dispersion state of the FH: a change from micro- to nanocomposite is accompanied with a significant reduction in the compliances (cf. Figures 4.11 and 4.13).

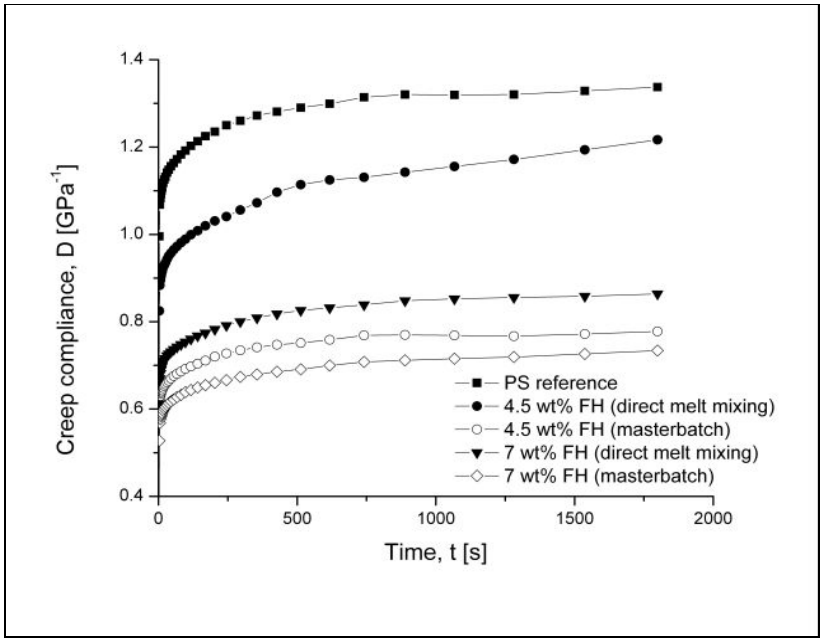

Figure 4.11: Creep of the PS reference and its FH composites prepared by different methods (stress applied for t = 30 min)

The course of the recovered compliance as a function of time (cf. Figures 4.12) indicated that incorporation of FH improved the elastic recovery and decreased the recovered compliance. Again, it was found that the recoverable compliances of the nanocomposites produced by MB are lower in the whole relaxation time range than those of the microcomposites prepared by DM. These findings suggest that creep and creep recovery behaviors are suitable indicators for the dispersion state of the fillers.

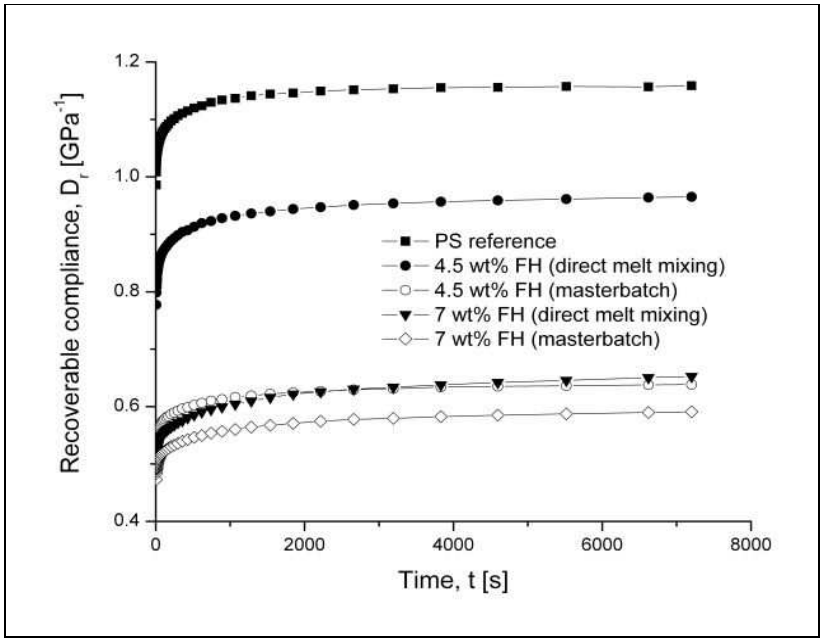

Figure 4.12: Creep recovery of the PS reference and its silicate composites prepared by different methods (stress removal for t = 60 min)

Effect of temperature

The creep response, viscoelastic in nature, depends on the polymer structure and testing temperature. As the temperature increases, the mobility of the chains increases, and this results in an increased creep rate at the same applied stress (e.g. [91]). Figures 4.13a-4.13c demonstrate the effect of increased temperature on the creep response of PS reference, PS/FH micro- and nanocomposites at 4.5 wt.% FH content. The general trend is that the creep compliance, read at a given time, increases with increasing temperature. The creep compliance decreased remarkably with incorporation of FH compared to the PS reference. One can also notice that at all test temperatures, the nanocomposite manufactured by the masterbatch technique proved to be the most creep resistant system.

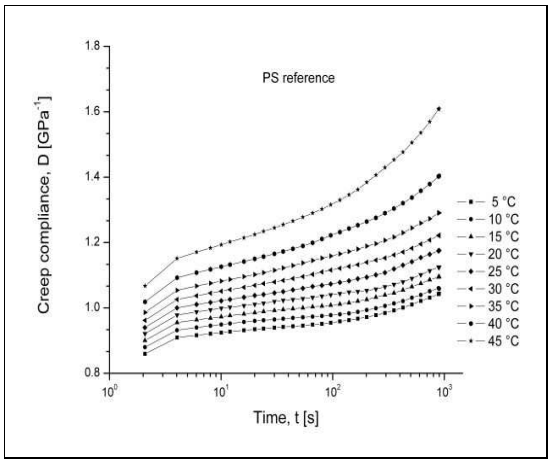

a)

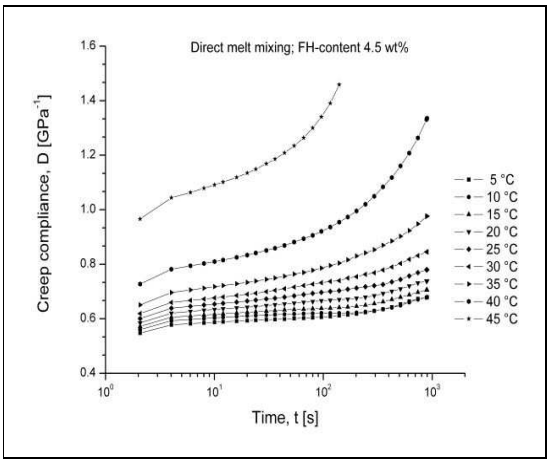

b)

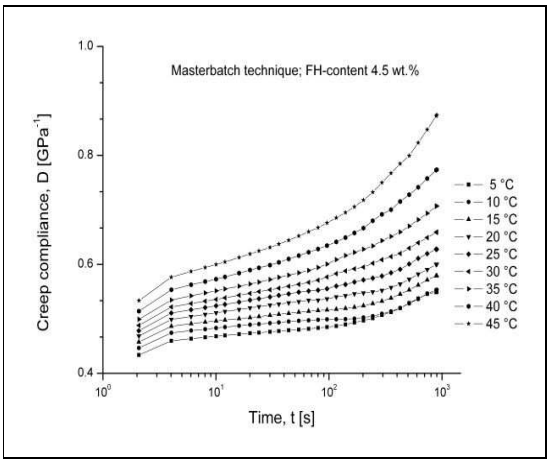

c)

Figure 4.13: Effect temperature on the tensile creep of PS (a) and its composites with 5 wt. % FH (b and c) prepared by different methods (creep conditions: stress = 4 MPa, creep time = 15 min)

Master curves

In order to get a deeper insight in the creep response of the PS systems the applicability of the TTS principle was checked. This was the driving force to perform isothermal short-term creep tests. According to equation 1.5, the related master curves, viz. creep compliance as a function of time, selecting T_{ref}=40 °C as reference temperature are depicted in Figure 4.14. The reinforcing effect of FH, which reduces the tensile creep compliance is obvious in this figure. The most interesting result is that the

creep compliance curves lay parallel to one another, at least until a given threshold (indicated by arrows in Figure 4.14). This means that the creep response in this stable creep range is matrix-dominated. As a consequence, the major effect of the reinforcement is the reduction of the initial compliance. The reduction of the compliance with increasing filler content is due to the development of an interphase in which the molecular mobility is reduced. DMTA spectra indicated that the T_g of the corresponding micro- and nanocomposites was shifted towards higher temperatures. So, the information in Figure 4.14 can be summarized by claiming that the interphase (via the filler dispersion) affects the initial compliance, however its change with time is bulk (matrix)-dominated.

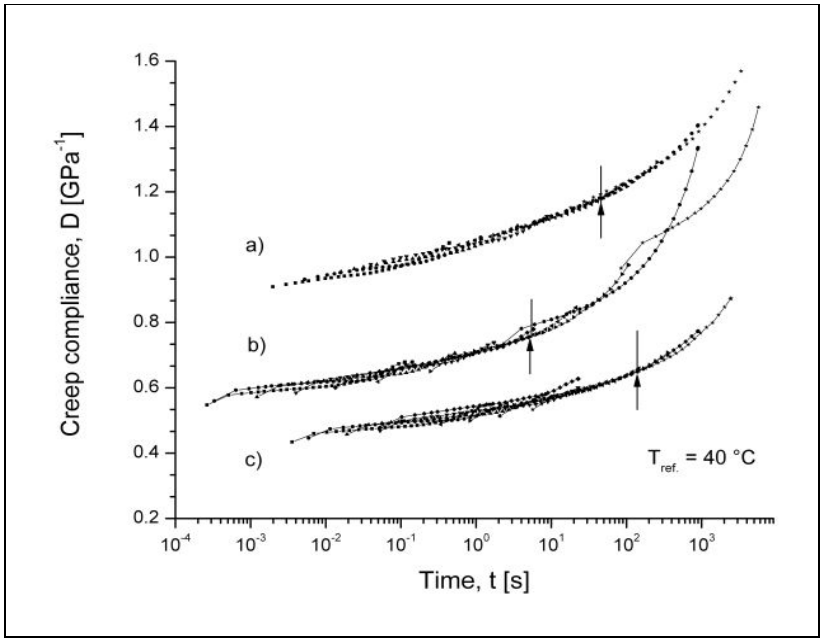

Figure 4.14: Creep master curves (compliance vs. time) constructed by considering T_{ref}= 40 °C for the PS reference (a) and its micro- (b) and nanocomposite (c). Note: FH-content of the composites was 4.5 wt.%

The next question is: Which kind of model description may be valid for the creep response? Note that the dependence of the shift factor as a function of temperature often follows the Williams-Landel-Ferry (WLF) rule -Equation 1.6.

Figure 4.15 demonstrates that the simple WLF-equation adequately describes the temperature dependence of the shift factors for the PS-systems studied. This note holds especially for the nanocomposite (prepared by the masterbatch technique) and PS reference. The deviation from the WLF prediction is higher for the microcomposite (produced by direct melt blending). This was, however, expected based on the corresponding master curve in Figure 4.14.

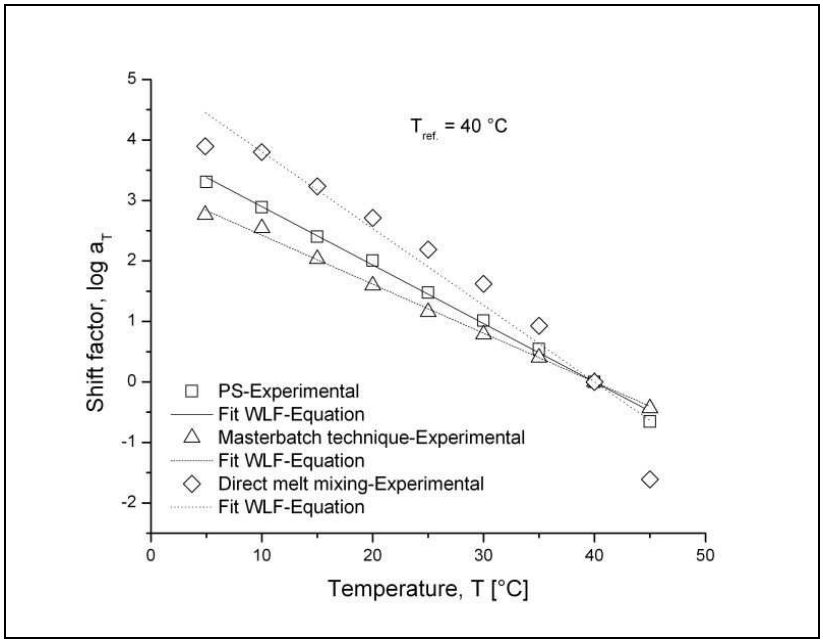

Figure 4.15: Temperature dependence of the shift factor (a_T) based on experimental results and calculation (WLF equation)

As far as the final creep failure concerns the possible scenario is summarized in Figure 4.16. Note that final failure is given by approaching an infinite large compliance value in this representation. Composites with a coarse particle size and poor adhesion to the matrix (i.e. no or limited interphase formation) may undergo extensive debonding. Due to the related voids, which accelerate the creep rate, the related composite may fail even prior to that of the matrix. On the other hand, well dispersed reinforcements with good bonding to the matrix (i.e. strong and well developed interphase) may improve the creep lifetime. Note that the effects summarized in the

scheme in Figure 4.16 are in line with the knowledge deduced from fracture mechanical, fatigue and fatigue crack propagation tests performed on various composites (e.g. [92-94]).

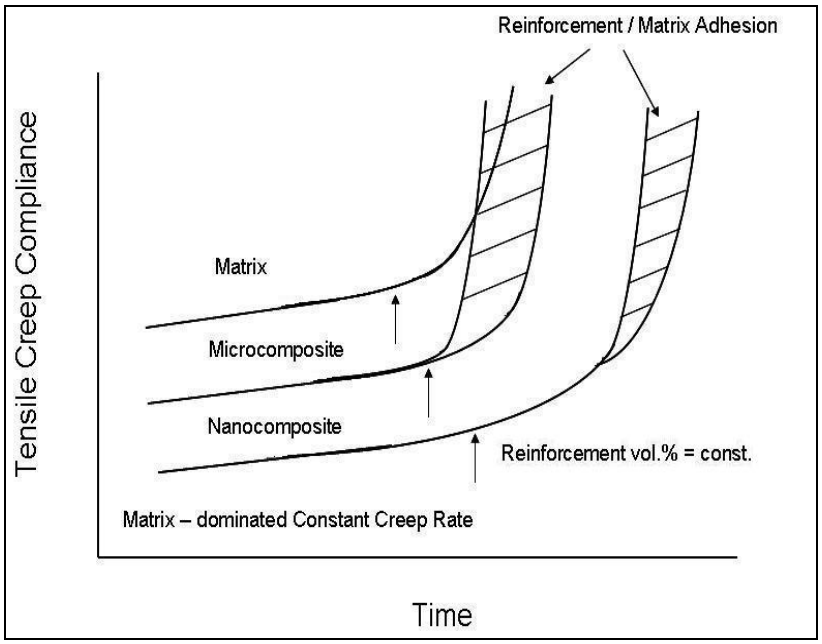

Figure 4.16: Scheme of the change of creep compliance as a function of time for micro- and nanocomposites with an amorphous matrix

4.1.2 Alumina-Filled Polystyrene Composites

4.1.2.1 Structure

The composite sheets produced by the masterbatch technique were more translucent at the same thickness than those prepared by direct melt blending –cf. Figure 4.17. This is the first hint for the difference in the dispersion stage of the alumina particles in the corresponding composites.

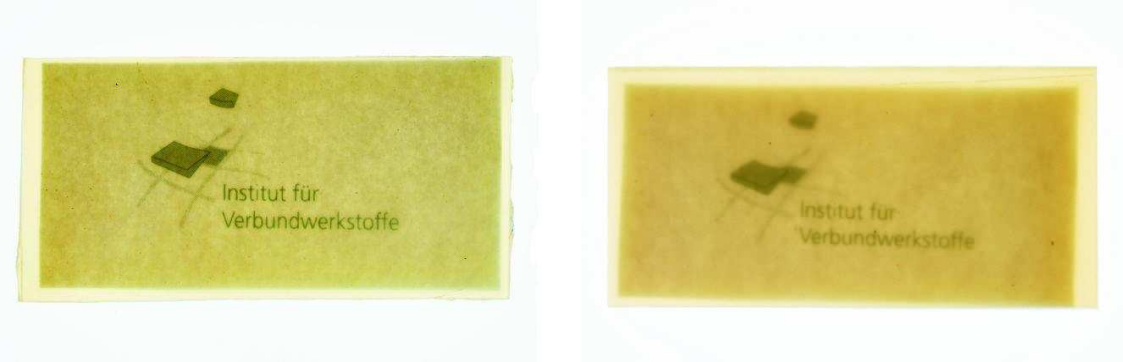

a) b)

Figure 4.17: Macrophotographs showing the difference in the transparency between PS/P2 composites at the same thickness (=1.1 mm) produced by MB (a) and DM (b)

TEM pictures taken from the direct melt compounded PS composites evidence the presence of large, micro-scale agglomerates of the alumina particles. They are thus correctly referred to microcomposites. The only difference between P2 and 11N7-80 particles is that the latter is also dispersed in smaller agglomerates in the PS matrix (cf. Figure 4.18b) by contrast to P2 (cf. Figure 4.18a).

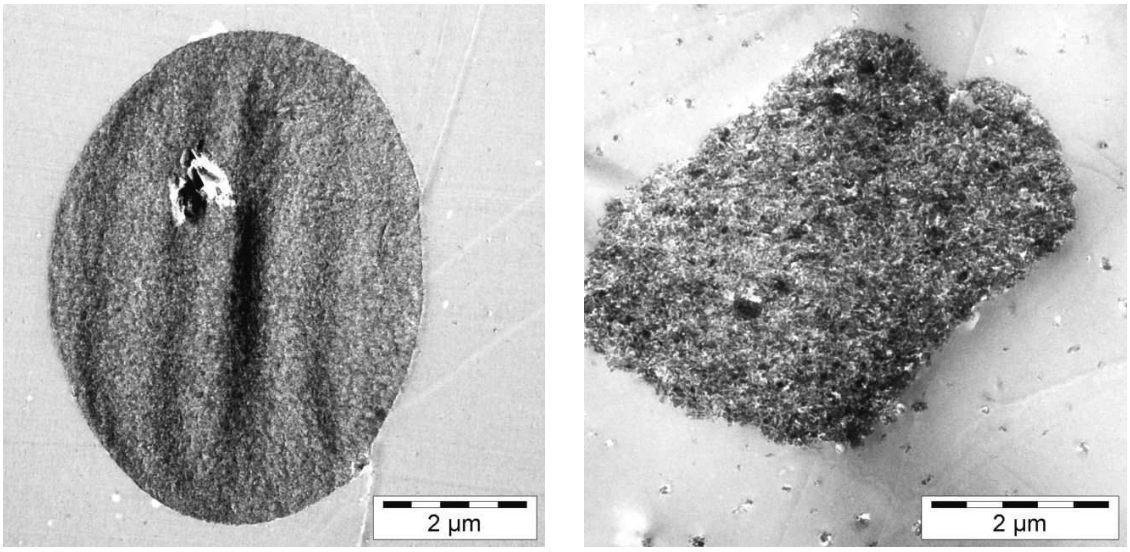

a) b)

Figure 4.18: TEM pictures from the PS/alumina microcomposites produced by melt blending with P2 (a) and 11N7-80 (b) alumina, respectively

Characteristic TEM pictures taken from the composites produced by the masterbatch technique in Figure 4.19 show that the alumina particles are nano-scaled dispersed in them. One can also recognize that the size of the primary particles is much smaller for P2 than for 11N7-80 which is in harmony with the data in Table 3.1. On the other hand, the particles are still agglomerated in the related nanocomposites (cf. Figure 4.19).

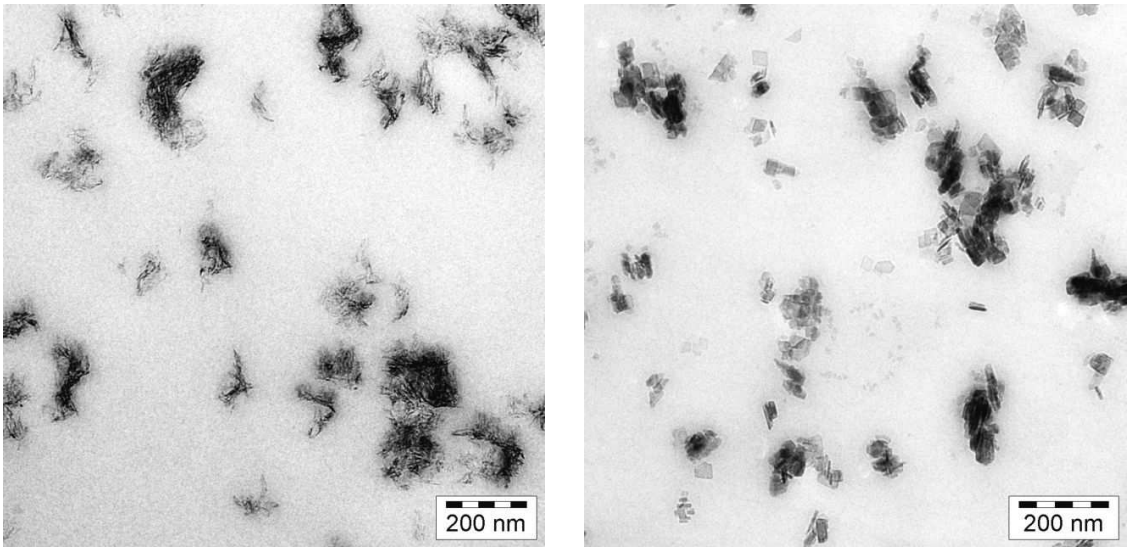

a) b)

Figure 4.19: TEM pictures from the PS/alumina nanocomposites produced by masterbatch technique with P2 (a) and 11N7-80 (b) alumina, respectively

The reason for this agglomeration is due to the PS latex mediated dispersion of the alumina in the PS. By reducing the compounding temperature when combining the PS with the dried PS/alumina from the latex (masterbatch) it could be shown that the alumina particles are located in the boundary layer between the PS latex particles (cf. Figure 4.20). This finding is in analogy with results reported on pristine clay modified natural rubber latices [40, 43]. The alumina particles become further dispersed mostly owing to shear forces in the fused PS during compounding.

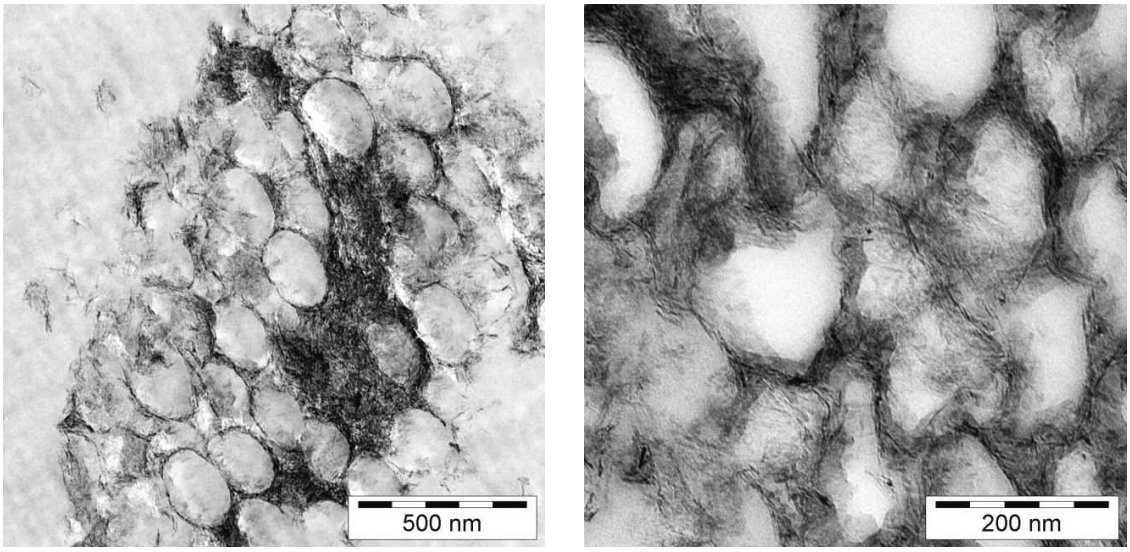

a) b)

Figure 4.20: TEM pictures taken from the PS/P2 nanocomposites produced by the masterbatch technique by setting the temperature of the compounding for T=165 °C

SEM pictures taken from the fracture surfaces of tensile loaded specimens give further insight in the alumina dispersion. This is due to the larger view-field in SEM compared to TEM. Figure 4.21 compares the fracture surfaces of the PS/P2 composites produced differently. Secondary cracking due to the large particles causing microductile deformation of the PS is obvious for the microcomposites (cf. Figure 4.21a). The onset of secondary cracking, manifesting in a characteristic dimple pattern, suggests that the alumina particles in the nanocomposite are homogeneously dispersed (cf. Figure 4.21b). The same statement holds for the PS composites with coarse alumina particles (cf. Figure 4.22). By comparing Figures 4.21a and 4.22a one may conclude that the 11N7-80 particles are better dispersed through direct melt blending in the PS matrix than the P2 particles.

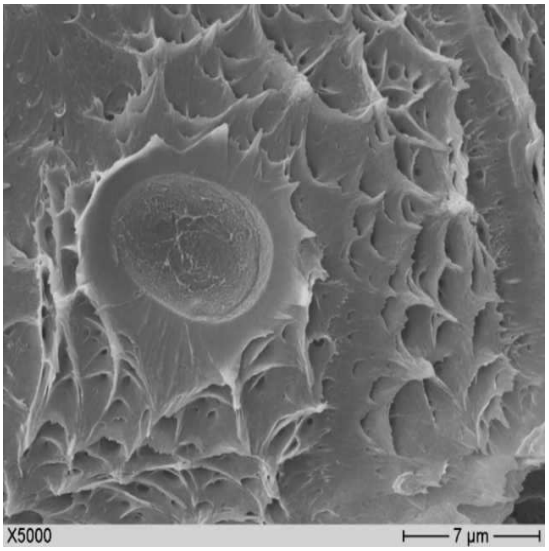

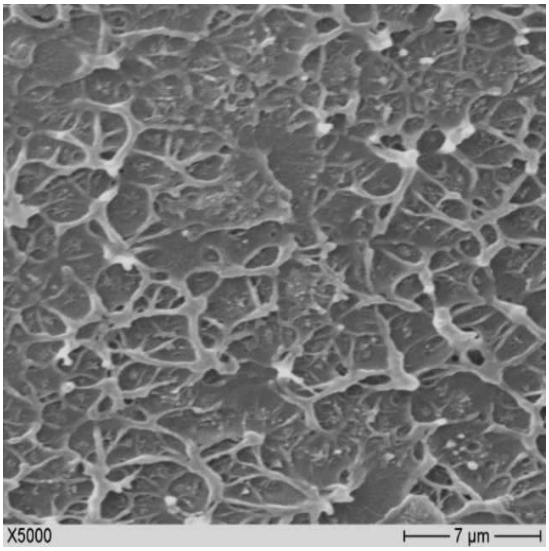

a) b)

Figure 4.21: SEM pictures of the PS/P2 composites produced by DM (a) and MB (b), respectively

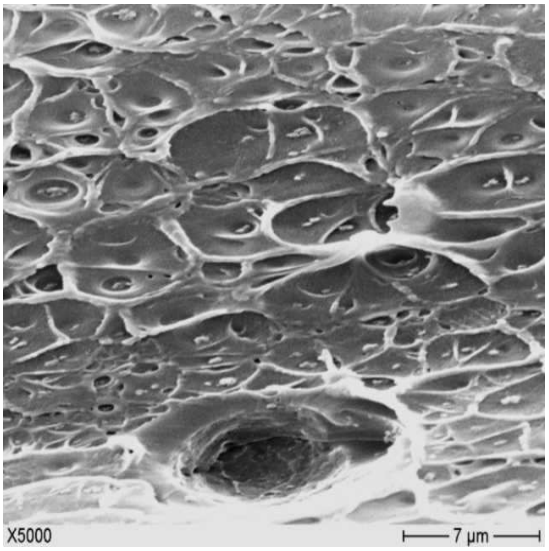

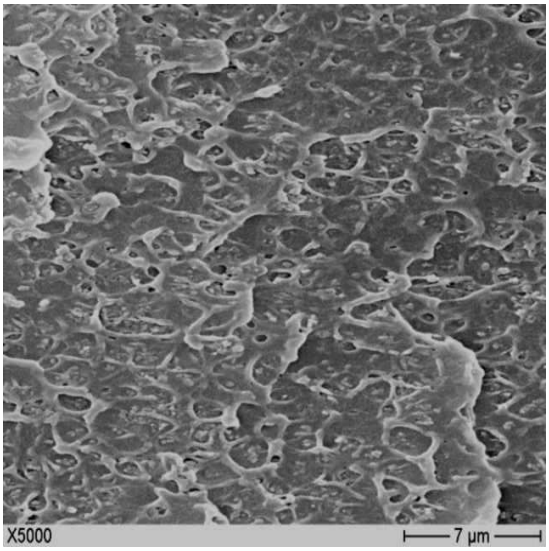

a) b)

Figure 4.22: SEM pictures of the PS/11N7-80 composites produced by DM (a) and MB (b), respectively

4.1.2.2 Thermal and Thermo-Mechanical Properties

Figure 4.23 depicts the storage modulus (E') and mechanical loss factor (tan δ) as a function of temperature for the composites containing 4.5 wt.% of alumina particles produced by various methods. Note that incorporation of alumina particles in PS resulted in a pronounced stiffness enhancement below the T_g. This reinforcing effect was accompanied with a shift in the T_g towards higher temperature. This can be assigned to the formation of an interphase with reduced molecular mobility. It is very surprising that the intensity of the T_g relaxation increases by adding alumina as usually the opposite trend occurs. For this effect the author has no explanation. Figure 4.23 also shows that the stiffness of the composite is governed by their production (yielding micro- and nanocomposites, respectively) and practically not influenced by the primary particle size of the alumina. Recall that under primary particle size that one achievable in water slurry is meant (cf. Table 3.1).

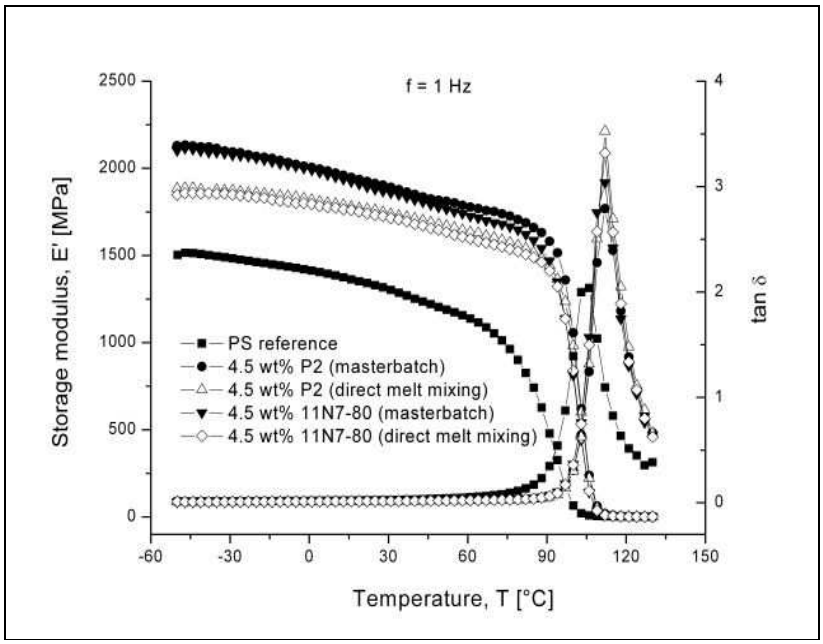

Figure 4.23: E' vs. T and tan δ vs. T traces for the PS/alumina composites produced by various methods

The stiffness of PS/alumina composites which were prepared by DM was always inferior to those produced by MB. An attempt was made to apply the time-temperature superposition principle to the DMTA data measured in function of both temperature (T= -50 °C…+130 °C) and frequency (f = 0.1 … 10 H z). Master curves in form of E' vs. frequency were produced by superimposing the storage modulus vs. frequency traces using the TTS principle. A reference temperature (T_0=70 °C) was used for this superposition process. Note that the related shift factor (a_T) is given in equation 1.17. The shift factors are linked with temperature via the Williams-Landel-Ferry (WLF) as given by equation 1.18.

The traces in Figure 4.24 indicate again that the effect of the preparation method (and alumina dispersion) is more pronounced than that of primary particle size of the alumina used.

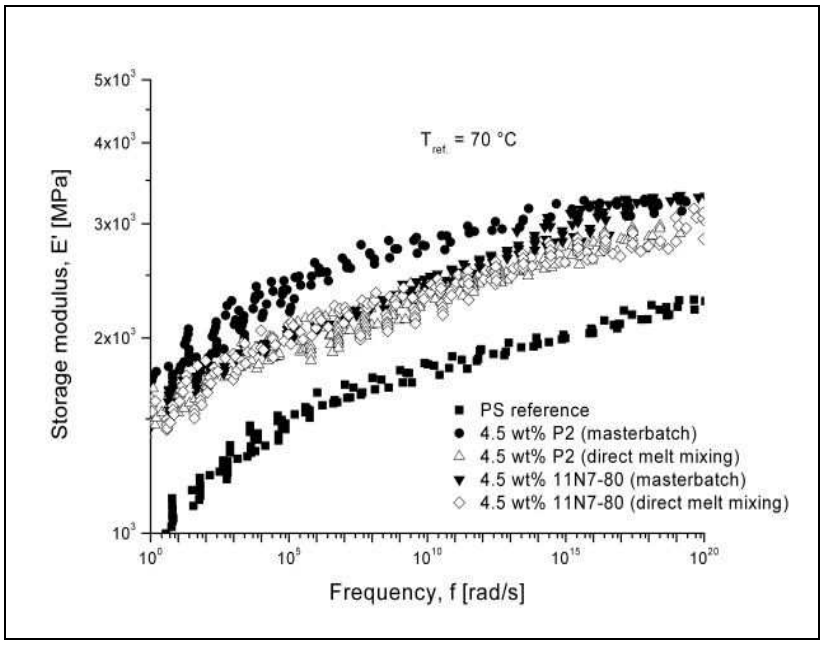

Figure 4.24: E' vs. frequency traces for the PS/alumina composites at $T_{ref.}$ = 70 °C

Figure 4.25 displays the course of the experimentally determined a_T values as a function of the temperature. The temperature range selected agrees with that of the creep tests. One can recognize that the experimental a_T data follow the WLF prediction albeit the latter strictly holds for polymers above their T_g. From the temperature dependence of the shift factor the activation energy (ΔH) can be computed by the equation 1.7. Based on the experimental data in Figure 4.25 the following ΔH values were

derived: PS reference=214 kJ/mol; PS + 4.5 wt.% P2 – direct and masterbatch techniques, respectively: 267 and 281 kJ/mol; PS + 4.5 wt.% 11N7-80 – direct and masterbatch techniques, respectively: 263 and 271 kJ/mol. The increase in ΔH with alumina filling suggests that the mobility of the PS chains was reduced in both PS micro- and nanocomposites. This is in concert with the observed shift in the corresponding tanδ vs T traces (cf. Figure 4.23). Moreover, the change in the ΔH values show the difference between micro- (lower ΔH) and nanocomposites (higher ΔH), and even the difference in the dispersion stage of the nanocomposites (ΔH is higher for the PS/P2 than for the PS/11N7-80 nanocomposite).

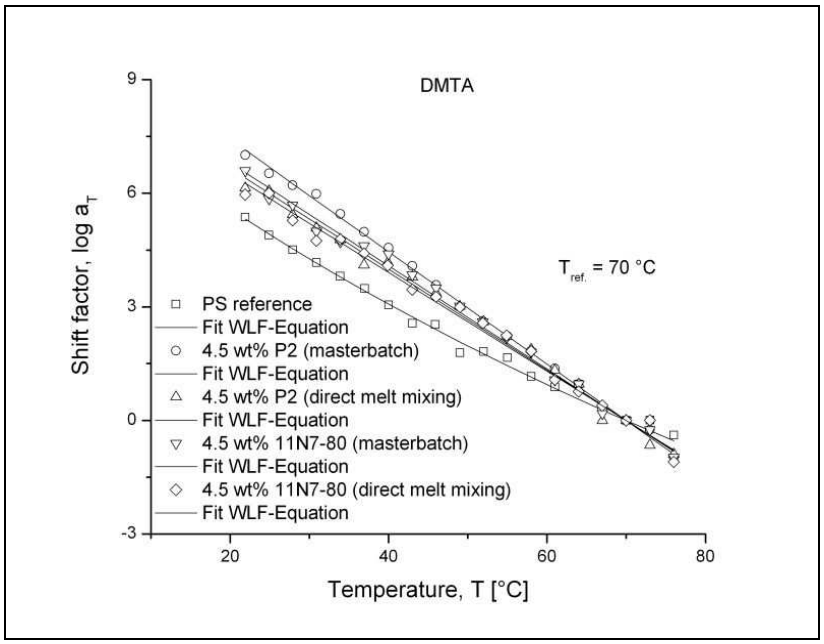

Figure 4.25: Experimental shift factors along with the related WLF fits in the temperature range T= 20 °C…75 °C for the systems stu died

The heat distortion temperature (HDT) is given by that temperature at which the specimen deflection reaches 0.25 mm under a given flexural load (in this case 0.46 MPa). According to the related standard (ASTM D 648) the heating rate is 2 °C/min. Recall that during our measurements in air the heating rate was 2 °C/min. In principle the HDT value represents a point in the flexural creep response when the displacement is plotted against the temperature. Figure 4.26 shows the related traces. One can see that the HDT values of the composites (94-95 °C) are far beyond that

of the reference PS (82 °C). On the other hand, the effects of composite preparation and primary particle size of the alumina are marginal (cf. Table 4.2).

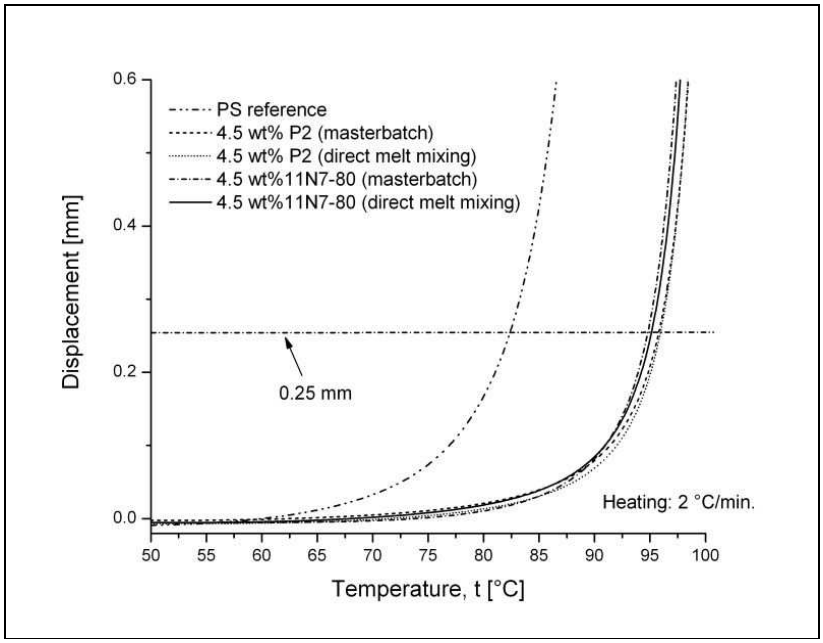

Figure 4.26: Displacement vs. temperature for the PS/alumina composites produced by various methods

4.1.2.3 Tensile Properties

Results of the tensile mechanical tests are given in Table 4.2. One can notice that the stiffness of the composites is strongly enhanced by adding alumina. The preparation techniques, yielding micro- and nanocomposites, have also a great impact on the stiffness. The latter is more than 20% higher for the nano- than for the microcomposites. The tensile strength is less sensitive for the composite preparation than the stiffness. Nevertheless, the strength of the composites was more than 40% higher than that of the reference PS (cf. Table 4.2). Elongation at break values suggests that the improvement in the stiffness and strength was achieved at the cost of the ductility of the composites.

Table 4.2: Tensile mechanical characteristics and HDT data of the PS reference and alumina-reinforced PS composites prepared by various methods

Property	Material				
	PS reference	Masterbatch technique		Direct melt mixing	
		PS/4.5wt% P2	PS/4.5wt% 11N7-80	PS/4.5wt% P2	PS/4.5wt% 11N7-80
Tensile modulus [MPa]	3026±268	4876±159	4789±196	3987±162	3899±206
Tensile strength [MPa]	27 ± 0.9	43±1.3	40±1.8	40±1.8	39±0.9
Elongation at break [%]	5.7±0.9	1.1±0.1	1.3±0.02	0.8±0.04	1.3±0.07
HDT [°C]	82.3±0.4	95.7±0.5	94.3±0.6	95.9±0.4	94.9±0.3

4.1.2.4 Viscoelastic Behavior

Figure 4.27-4.28 display the creep and recovered compliance values for the PS and its alumina composites produced by direct melt mixing and masterbatch methods. The addition of alumina particles into PS matrix resulted in a considerable reduction of the creep compliance, as shown by the plots of creep and recovered compliances against time. The decrease in creep compliance is due to the reinforcing effect of the alumina particles. For the composites containing 4.5 wt.% P2 for example the creep compliance was reduced by ca. 55 % and 30 % compared to the reference PS when produced by the masterbatch technique and direct melt compounding, respectively. The most striking finding is that the primary particle size of the alumina likely affects the creep behavior. Note that the resistance to creep increases with decreasing alumina particle size.

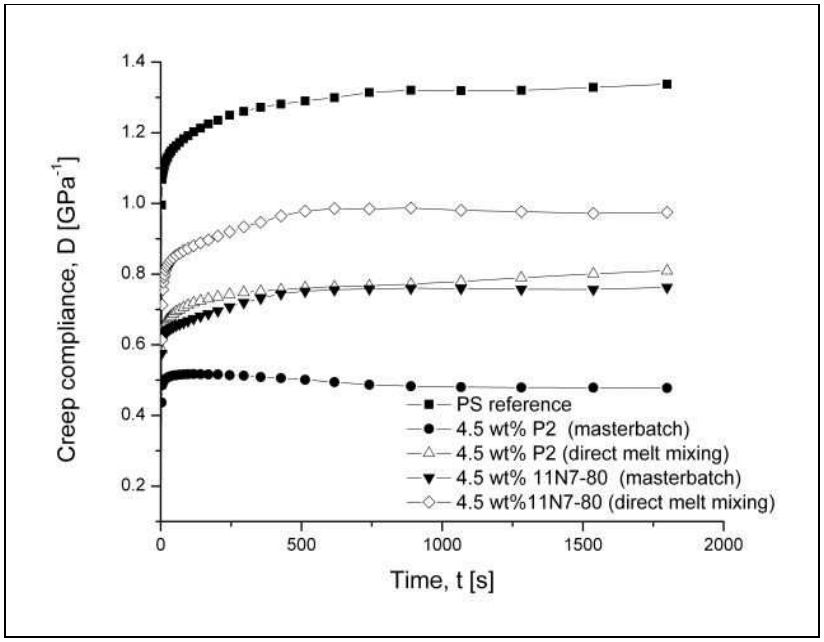

Figure 4.27: Creep of the reference PS and its alumina composites prepared by different methods at RT

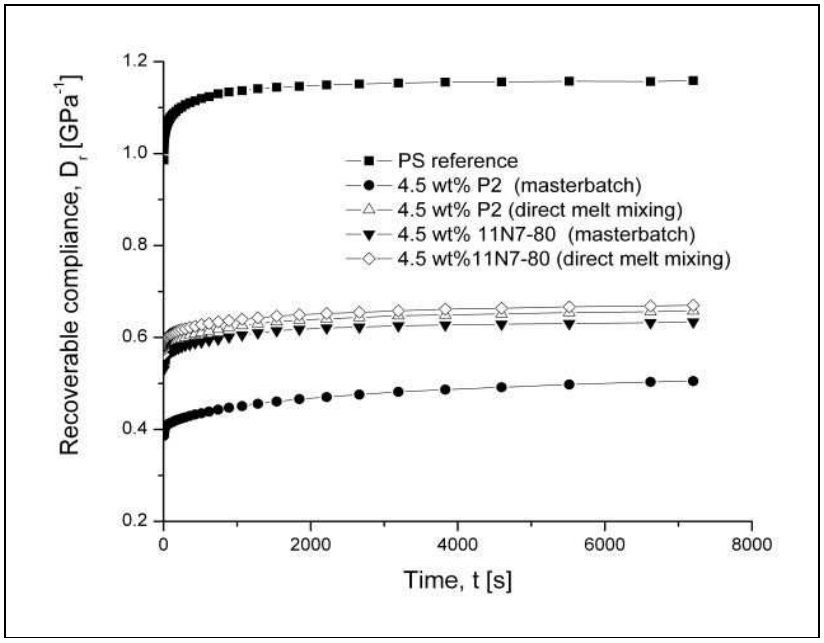

Figure 4.28: Creep recovery of the reference PS and its alumina composites prepared by different methods at RT

Figure 4.29 demonstrates the effect of increasing temperature on the creep compliance of the PS and its nanocomposite with 11N7-80 alumina. Note that the creep compliance increases with increasing temperature. On the other hand, one can recognize that the creep compliance decreased markedly for the PS/11N7-80 nanocomposite, especially at higher temperatures - cf. Figure 4.29a and b.

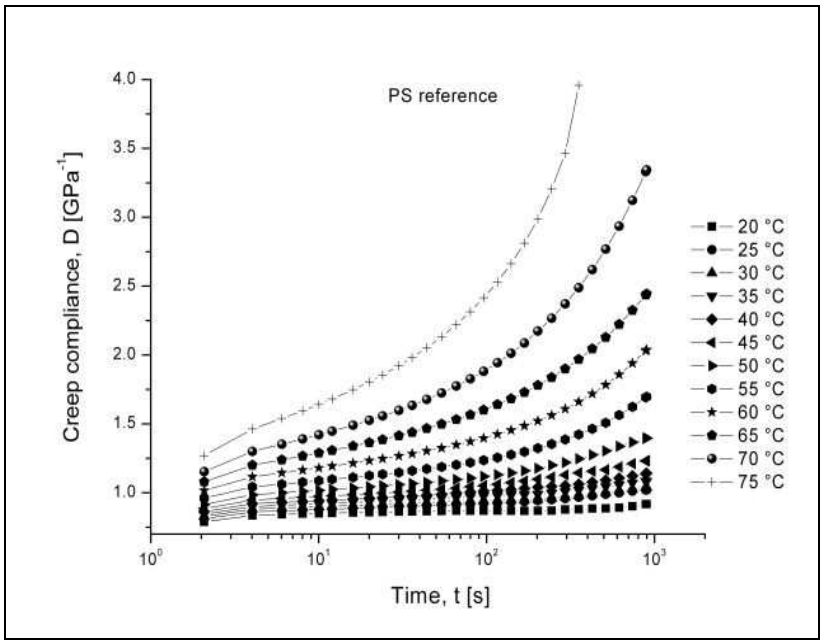

a)

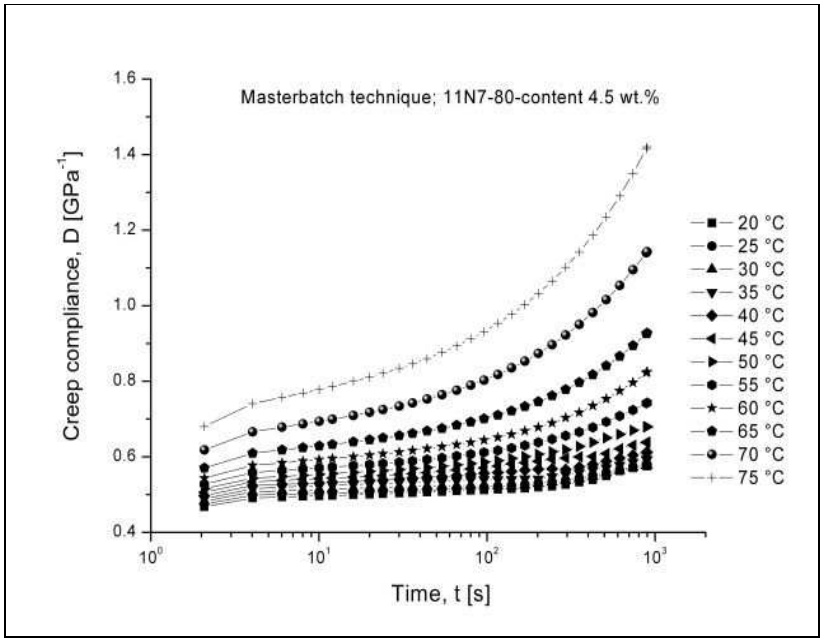

b)

Figure 4.29: Effect of temperature on the tensile creep of PS (a) and its composite with 4.5 wt.% alumina 11N7-80 prepared by the masterbatch technique (b)

Creep master curves were constructed by considering the TTS principle. The shift factors can be also correlated with temperature using the WLF equation (cf. equation 1.6). In order to highlight the differences T=70 ° C was taken as reference temperature. The corresponding master curves are summarized in Figure 4.30. The reinforcing effect of the alumina particles is obvious in this figure.

As, expected according to Figures 4.27 and 4.28, the primary particle size, or more exactly the dispersion state of the alumina, are well reflected in the creep master curves (cf. Figure 4.30). The change from micro- to nanocomposite reduces further the creep compliance. This may be associated with pronounced changes in the creep rate. It was reported that the creep rate is hardly affected by the dispersion state of layered silicates (c.f. section 4.1.1.4). This claim holds for the PS/11N7-80 composites and also for the direct melt blended PS/P2, at least in a given time interval (cf. initial parallel run of the creep curves in Figure 4.30). On the other hand, the PS/P2 nanocomposite exhibits a creep rate differing substantially from that of the PS matrix. It is not known whether this behavior is due to the dispersion of P2, or to other rea-

sons (material inhomogeneity, selection of the reference temperature). It has to be mentioned that such creep behavior was already reported for thermoplastic nanocomposites, however, with a semicrystalline matrix [95].

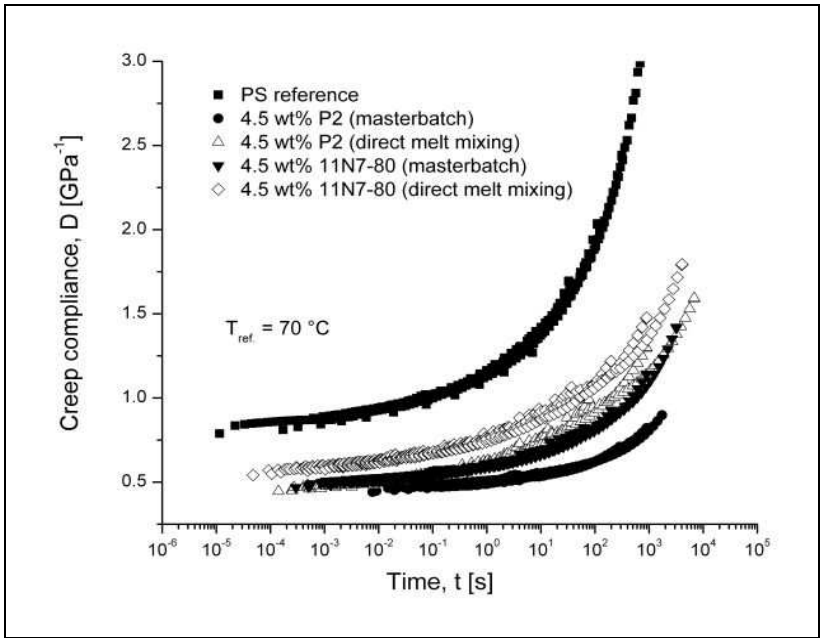

Figure 4.30: Creep master curves (compliance vs. time constructed by considering $T_{ref.}$ = 70 °C for the PS reference and its micro- (direct melt blended) and nanocomposites (produced by the masterbatch technique)

Figure 4.31 depicts the experimentally determined a_T values for the studied creep interval. One can see that the experimental a_T data obey the WLF equation, similar to the DMTA results (cf. Figure 4.25). Equation 1.7 was adopted to compute the creep activation energy values. They were found as given below: PS reference=196 kJ/mol; PS + 4.5 wt.% P2 – direct and masterbatch techniques, respectively: 99 and 198 kJ/mol; PS + 4.5 wt.% 11N7-80 – direct and masterbatch techniques, respectively: 204 and 172 kJ/mol. Comparing these activation energies with those from the DMTA (listed above in section 4.1.2.2) a fair agreement can only be noticed for the neat PS. The large discrepancy for the alumina filled micro- and nanocomposites suggests that the creep response is far more sensitive to the dispersion stage of the filler in the related specimens than in the DMTA test - although both tests were performed in the

linear viscoelastic range. However, the loading configuration (single cantilever vs. uniaxial tensile) and especially the related strain values (0.01 vs. 0.38 % /corresponding to the stress applied, viz. 3 MPa/ for the DMTA and creep tests, respectively) differed considerably from one another. This finding means that numerous parallel tests are required to determine reliable creep master curves.

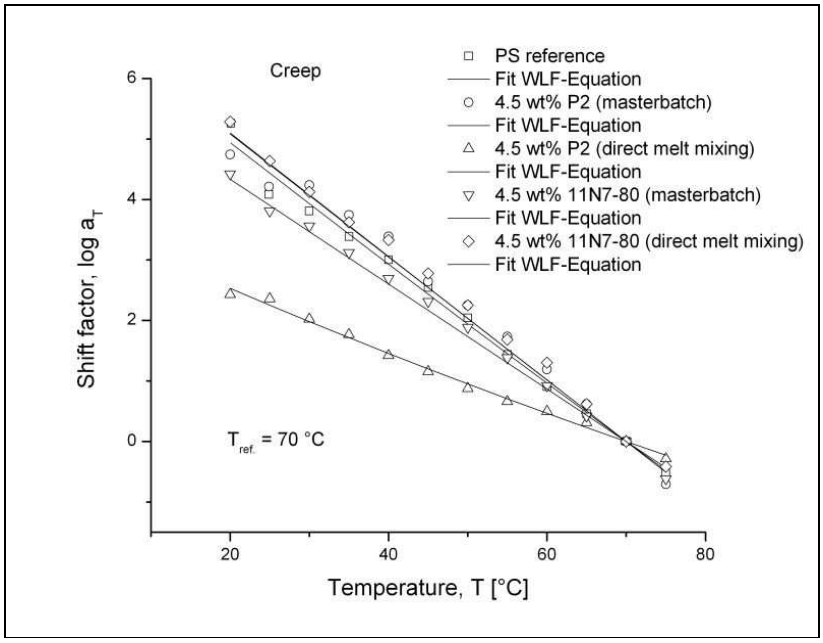

Figure 4.31: Experimental shift factors along with the related WLF fits in the creep temperature range T= 20 °C…75 °C for the systems studied

4.1.2.5 Rheology

The reference PS show clear shear thinning behavior in the viscosity vs. angular frequency curves - cf. Figure 4.32. Note that the viscosity of the nanocomposites is always higher than that of the corresponding microcomposites albeit the difference is relatively small.

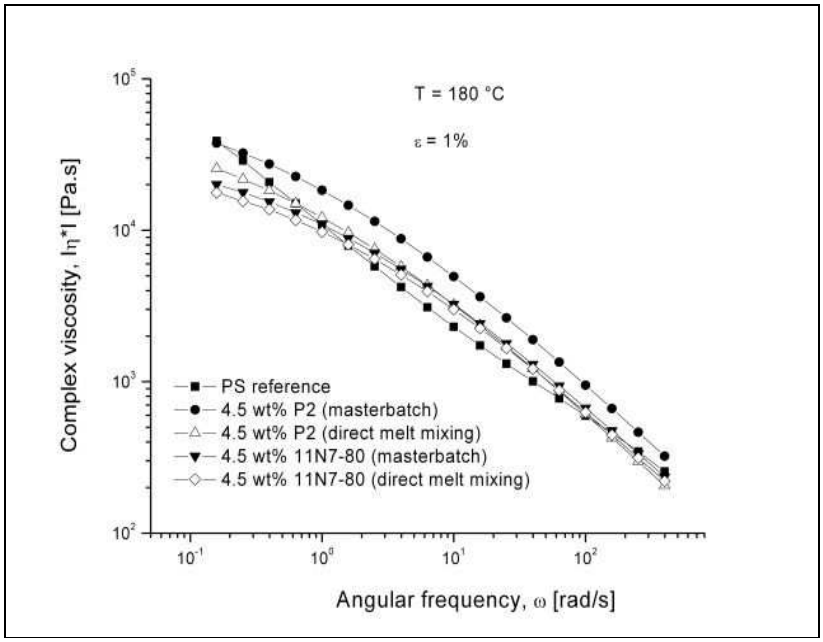

Figure 4.32: Viscosity vs. angular frequency for the reference PS and its alumina composites prepared by different methods at T=180 ° C

4.1.3 Polyoxymethylene/Polyurethane/Alumina Ternary Composites

4.1.3.1 Structure

TEM picture taken from the dried PU/alumina masterbatch (alumina content: 30 wt.%) is shown in Figure 4.33a. When this PU/alumina (MB) is melt mixed with the POM granules, a finer alumina dispersion is achieved (cf. Figure 4.33b). By contrast, TEM pictures taken from the DM compounded POM/PU/alumina ternary composite evidence the presence of large agglomerates of the alumina particles (cf. Figure 4.33c). One can thus state that the alumina particles are nanoscale- and microscale-dispersed using MB and DM, respectively.

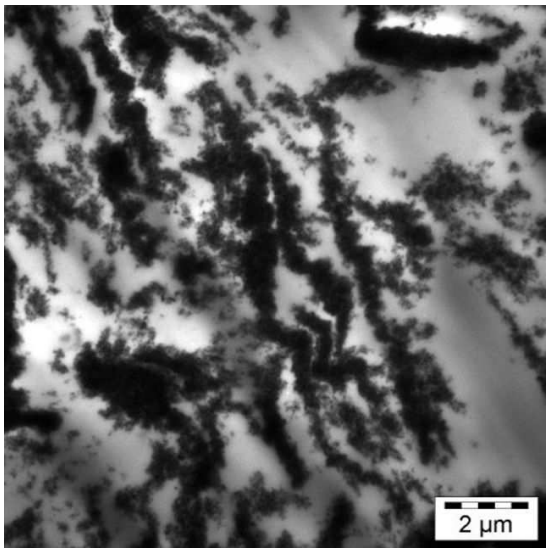

a)

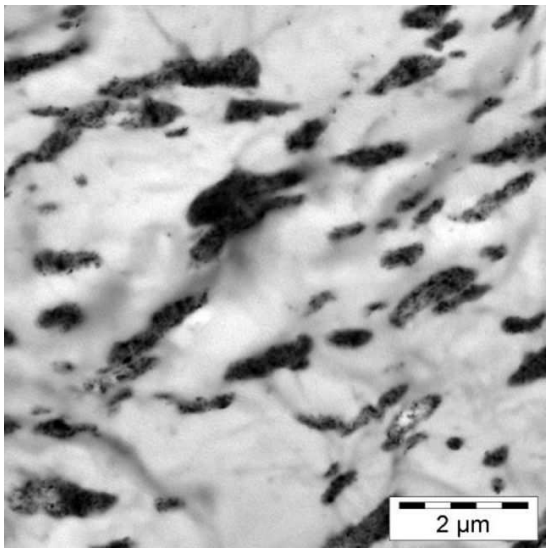

b)

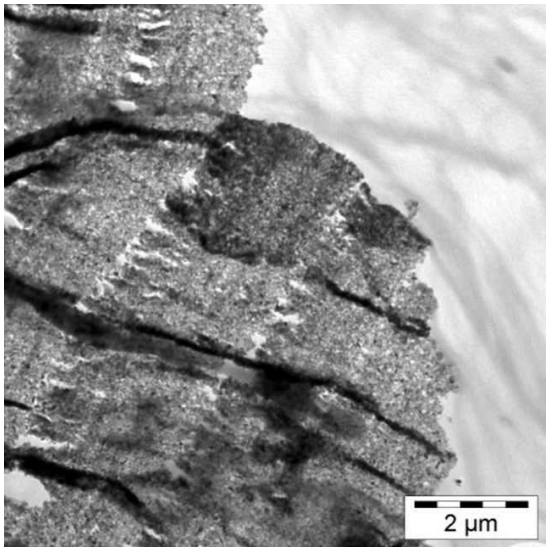

c)

Figure 4.33: TEM pictures taken from PU/alumina (MB-alumina content) (a), the composite composition-POM/PU/alumina produced by masterbatch technique (b) and direct melt compounding (c). Notes: the alumina content of the POM/PU/alumina was 3 wt.%

Similar observations for these ternary systems can be deduced from SEM micrographs taken from the fracture surfaces (Figure 4.34). Alumina agglomerates of several microns can be seen in the POM matrix when produced by DM (cf. Fig. 4.34b). On the other hand, they must be far better dispersed in the composites produced by the route MB (cf. Fig. 4.34a). One can also recognize that the PU domains are in the range of 0.5-2.5 µm irrespective to the production method. Recall that this range is markedly larger than the initial size of the PU particles in the corresponding latex.

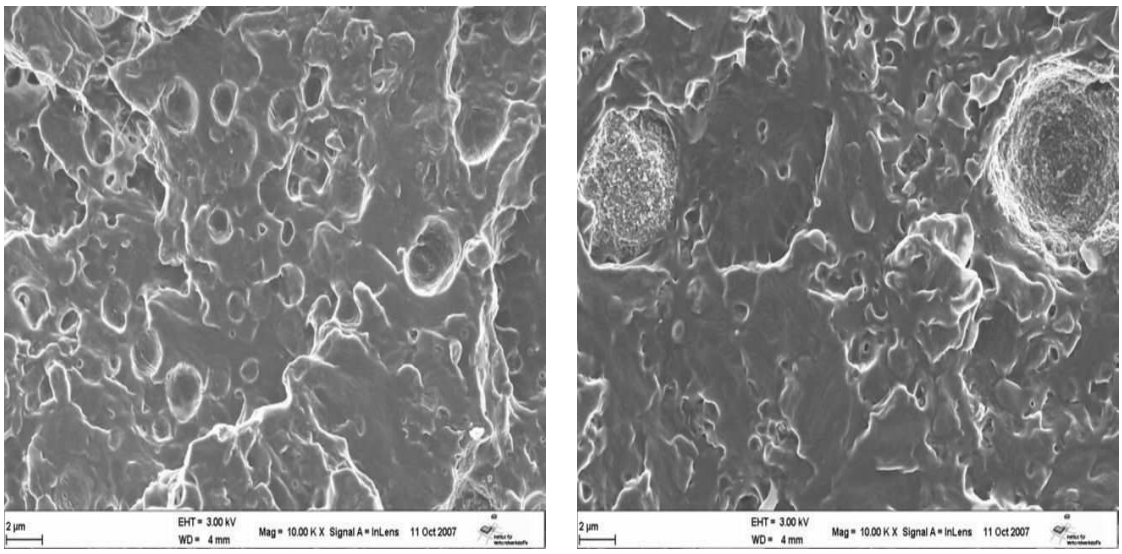

a) b)

Figure 4.34: SEM pictures taken from the tensile fracture surfaces of the composites produced by masterbatch technique (a) and direct melt compounding (b)

PLM is an important method to study the morphology of POM [62-63]. Figures 4.35a-4.35d, compare the spherulitic structures of POM, POM/PU blend and POM/PU/alumina ternary composites prepared by MB and DM, respectively. POM crystallizes in large spherulites (cf. Figure 4.35a). Addition of PU significantly disturbs the spherulitic structure of POM, however, does not influence much the spherulite size. Some slight reduction in the spherulite size of POM/PU/alumina ternary composites prepared by MB and DM can be observed (cf. Figs. 4.35c-4.35d when compared with that of the neat POM (cf. Fig. 4.35a). Interestingly, very regular spherulites appear in the ternary composite produced by MB. In line with the SEM results, the large alumina agglomerates are also obvious in the DM composites on the corresponding PLM picture (cf. Fig. 4.35d).

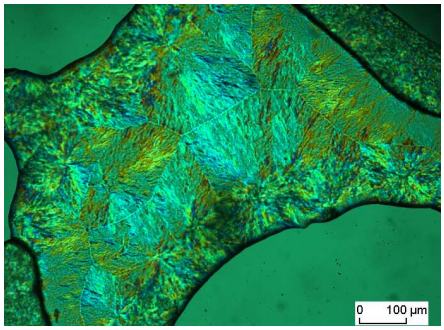

a)

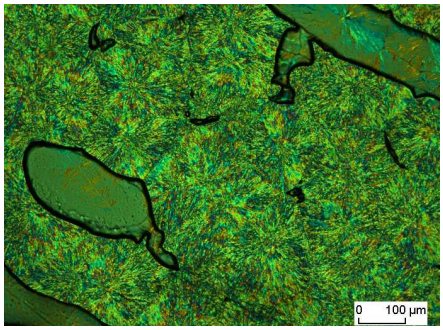

b)

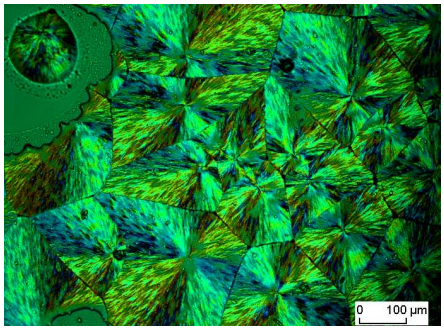

c)

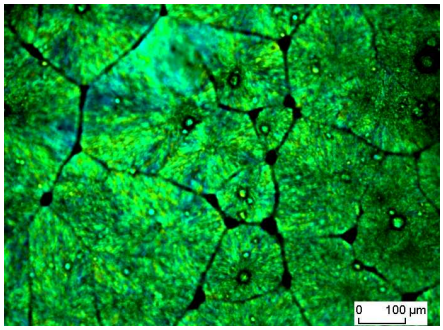

d)

Figure 4.35: PLM pictures of the isothermally (T=148 ° C) crystallized POM (a), POM/PU blend (b), and the composites produced by the masterbatch (c) and direct melt compounding (d), respectively

4.1.3.2 Crystallization and melting Properties

Apart of the spherulite structure, the incorporation of PU and PU/alumina influenced also the crystallinity of POM in the related systems – cf. DSC data summarized in Table 4.3. The related data suggest that PU and alumina marginally increased the crystallinity of POM.

Table 4.3: Crystallization and melting characteristics for the systems studied

Designations: T_m – melting temperature, T_c – crystallization temperature, H_m – melting enthalpy, X_c – crystallinity (based on the net POM content)

Sample Designation	T_m (°C)	T_c (°C)	Delta H_m (J/g)	% X_c (POM)
POM	166.8	145.9	155.2	83.4
POM/PU(10)	168.7	145.9	156.3	84.0
POM/PU(10)/11N7-80(3)=>(DM)	169.3	145.4	158.4	85.2
POM/PU(10)/11N7-80(3)=>(MB)	168.5	146.0	157.1	84.5

4.1.3.3 Thermal and Thermo-Mechanical Properties

Figure 4.36a and b depict the storage modulus (E') and mechanical loss factor (tan δ) as a function of temperature for POM, POM/PU blend and the composites with alumina particles produced by various methods. One can notice that the storage modulus of the composites is enhanced by adding alumina compared to the POM/PU blend. Moreover, the E' vs. T trace of the DM composite was always below that of the MB version. This can be attributed to the difference in the dispersion stage of alumina as discussed before. Figure 4.36 also shows that the highest stiffness exhibited the plain POM in the whole temperature range.

Concerning the relaxation processes, it is well known that pure POM exhibits three transitions [96-98]. The relaxation transition (γ) located at around -60 °C is assigned to the glass transition temperature (T_g; cf. Fig. 4.36b). The two peaks, observed at ambient temperature (β-relaxation) and ca. 130 °C (α-relaxation), respectively, are usually assigned to the motions of long molecular segments in disordered and well ordered crystalline phases, respectively [96]. Addition of PU results in a further relaxation, located at ca. -50 °C, representing the T_g of the PU (cf. Fig. 4.36b). One can notice that the incorporation of PU and alumina increases the intensity of both the α- and β-relaxations. The most prominent change can be noticed for the β-relaxation. The intensity of this β-peak further increases when apart of PU also alumina is present. The related change suggests enhanced segmental motion in the

boundary amorphous layers of the crystals in the disordered crystalline phase. The shift of this peak towards higher temperatures due to alumina indicates for the reinforcing effect of the latter (cf. Fig. 4.36b).

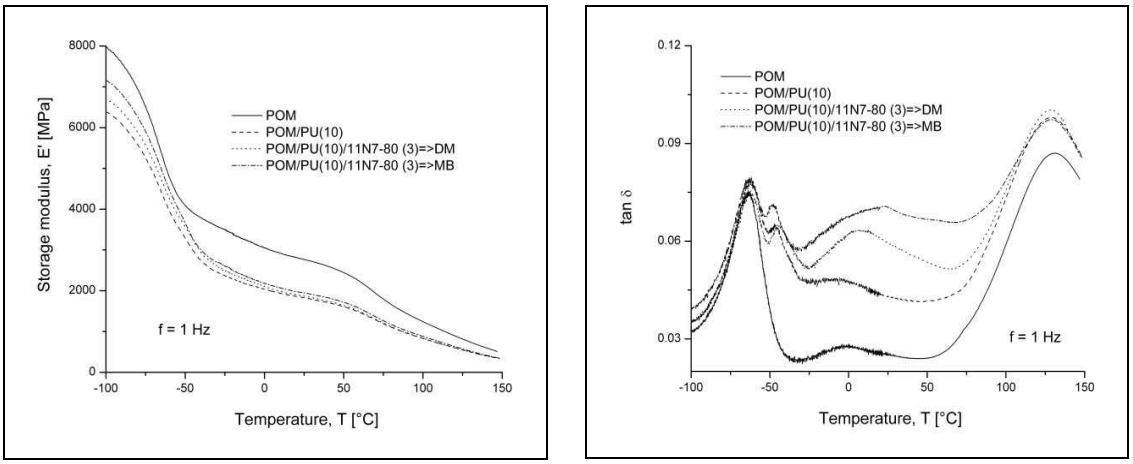

a) b)

Figure 4.36: E' vs. T (a) and tan δ vs. T (b) traces for the POM and its binary and ternary systems studied

It has been reported that by adding PU and inorganic fillers, like organoclay [63], may increase the thermal stability of POM. This is in accord with our TGA observation -cf. Figure 4.37. It can be seen that that the resistance to thermooxidative degradation of the POM/PU blend is slightly lower than that of POM. On the other hand, the POM/PU/alumina ternary composites start to degrade at markedly higher temperature than either POM or POM/PU. There is practically no difference between the TGA traces of the MB and DM composites. Anyway, the incorporation of alumina strongly enhanced the thermooxidative resistance of POM/PU blend when tested in oxygen.

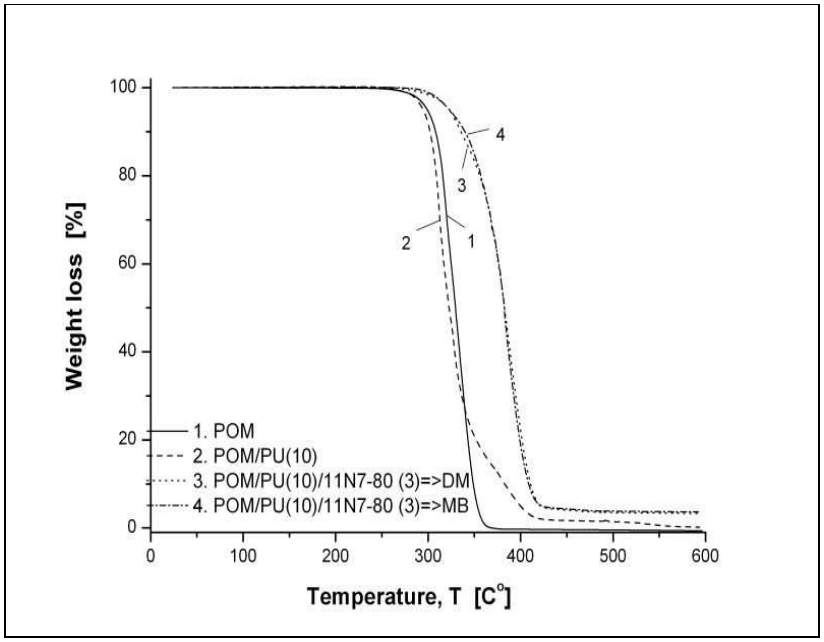

Figure 4.37: Weight loss vs. temperature for the POM and its binary and ternary systems in oxygen

4.1.3.4 Tensile Properties

The effects of PU and alumina on the tensile mechanical data of POM systems are displayed in Figure 4.38. Addition of PU to POM or the combined use of PU and alumina improve the elongation at break, however, at cost of the tensile strength. The POM/PU/alumina ternary composites prepared by the MB method exhibited higher tensile strength accompanied by much higher elongation at break as compared to the composite produced by DM or to the POM/PU blend. Recall that the alumina particles are by far better dispersed in the matrix when prepared via the MB instead of the DM technique (cf. Figs. 4.33-4.34). This is in line with recent reports claiming that the tensile mechanical response is strongly affected by the dispersion state of nanofillers.

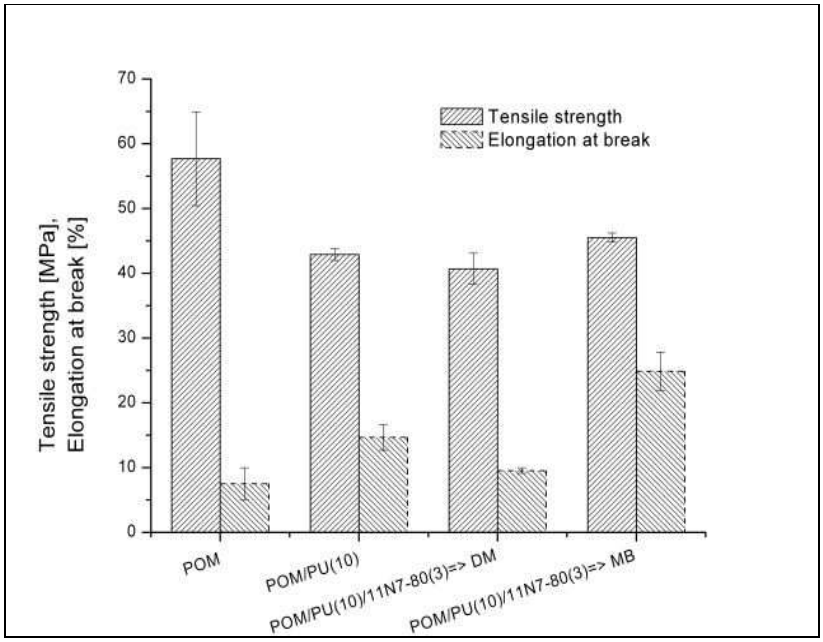

Figure 4.38: Tensile mechanical characteristics of the systems studied

4.1.3.5 Viscoelastic Properties

The creep curves of POM are shown in Figure 4.39a for six values of the applied load. The effect of applied stress was enough that the creep behavior was considered to be linear in this range of applied stress. First, the isochronous stress-strain curve was constructed after tests measuring the strain at various stresses as a function of time. Figure 39b shows the stress-strain data after 30 minutes for the POM at T=30 °C. The related data indicate that even under 6 MPa load the specimen is in the linear viscoelasticity range. In the subsequent tests all specimens were subjected to 6 MPa stress and the strain was recorded as a function of time.

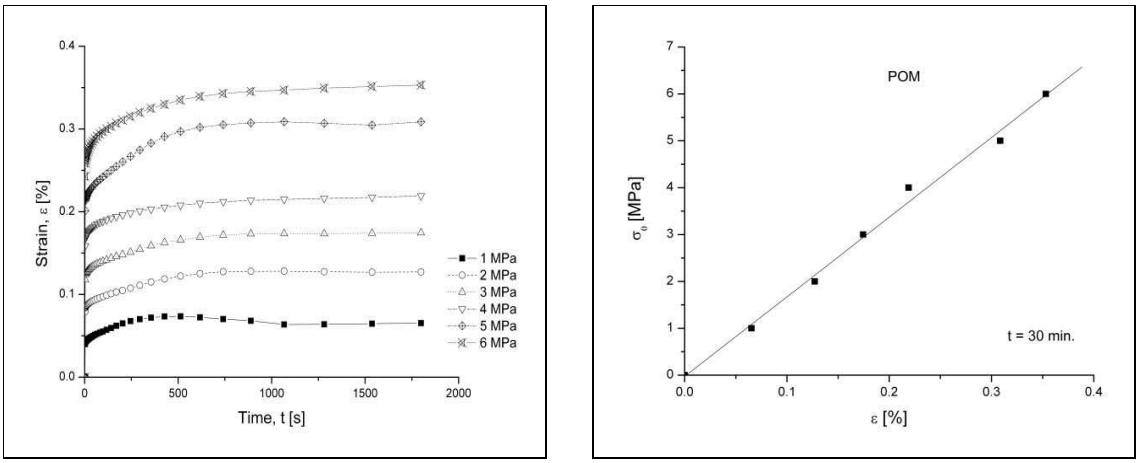

a) b)

Figure 4.39: Constructed isochronous stress-strain curve of POM. a) strain vs. time traces (different stress applied for t = 30 min) and b) stress vs. strain traces after applied load for 30 minutes, at T= 30 °C

Figures 4.40-4.41 display the traces of the creep and recovered compliance as a function of time for the POM, POM/PU blend and the alumina-containing ternary composites produced by DM and MB methods, respectively, at T=30 °C. The addition of PU into POM matrix resulted in a considerable increase in the creep compliance, as expected owing to this rubber modification (cf. Figs. 4.40-4.41). The creep compliance values of the composites are smaller compared to the POM/PU blend showing the reinforcing effect of the alumina. The compliance values were reduced by ca. 23 % and 17 % compared to the POM/PU blend when alumina was introduced by the MB and DM technique, respectively.

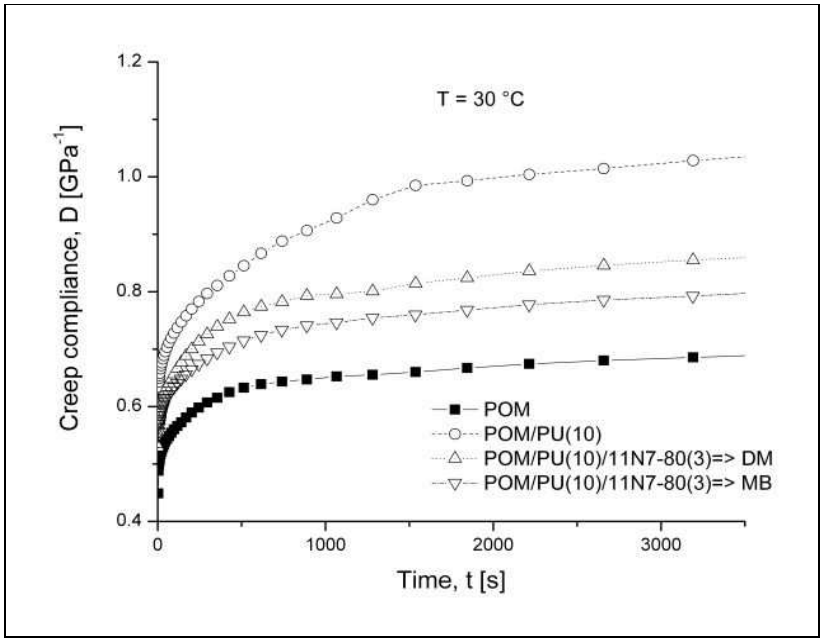

Figure 4.40: Creep of POM, POM/PU blend and POM/PU/alumina composites at T=30 °C (stress, 6 MPa applied for t = 60 min)

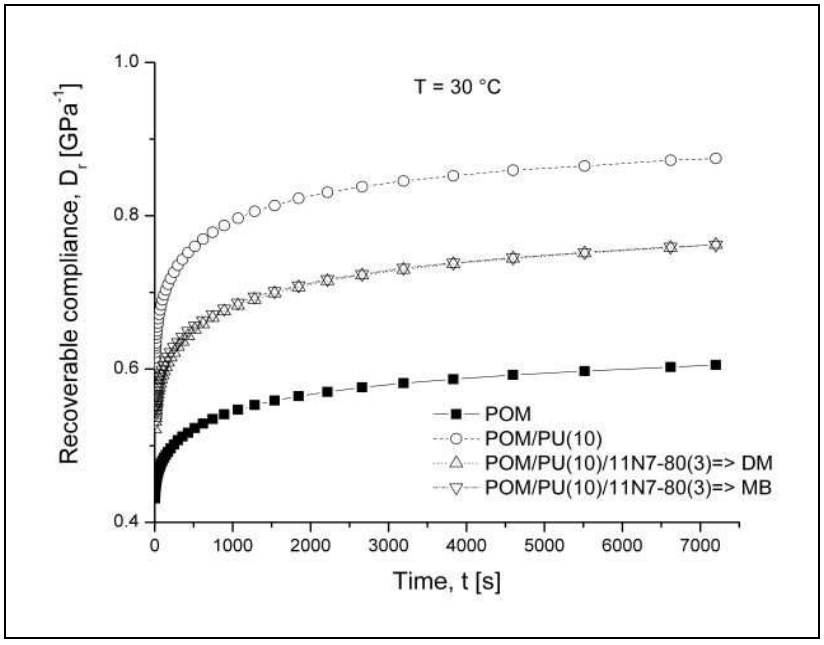

Figure 4.41: Creep recovery of POM, POM/PU blend and POM/PU/alumina composites at T=30 °C (stress removal for t = 120 min)

Figures 4.42a-4.42c demonstrate the effects of increased temperature on the creep response of POM/PU blend and POM/PU/alumina ternary composites produced by DM and MB techniques. One can recognize that the creep compliance decreased remarkably with the incorporation of alumina compared to POM/PU blend at all test temperatures.

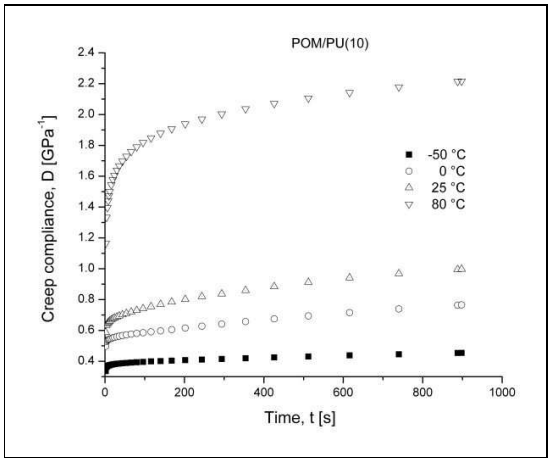

a)

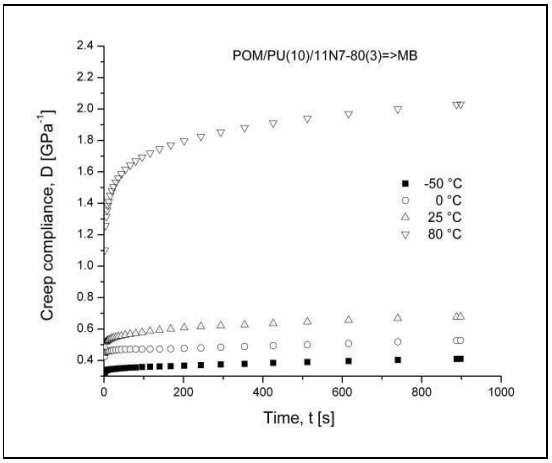

b)

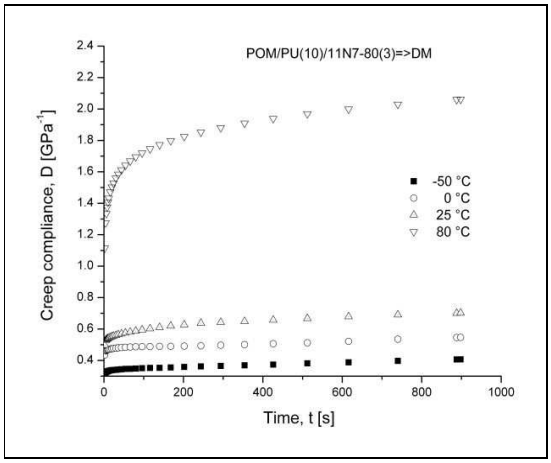

c)

Figure 4.42: Effect of temperature on the tensile creep of POM/PU blend (a), and for the ternary composites produced by MB (b) and DM (c)

The creep data measured in function of both time and temperature (T= -50 °C…80 °C) have been considered to create creep master curves by adopting the TTS principle. The creep response at T_0=70 °C was taken for reference. The WLF equation has been employed for many polymeric materials to fit the creep compliance vs. time curves. The shift factors can be also correlated with temperature using the WLF equation 1.6. Figure 4.43 displays the course of the experimentally determined a_T values as a function of the temperature. Note that the experimental data are well fitted by WLF equation.

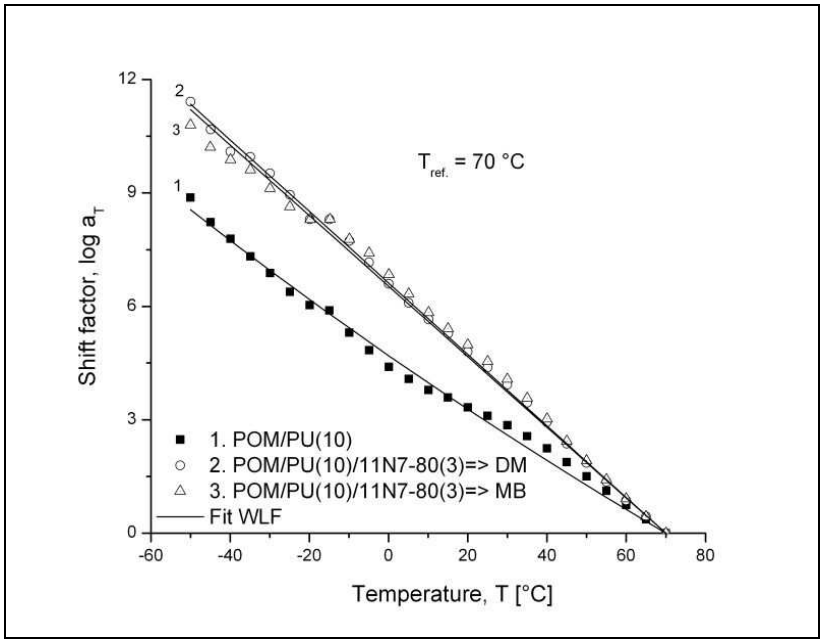

Figure 4.43: Experimental shift factors of the systems studied along with the related WLF fits for the temperature range T= -50 °C…80 °C

Attempt was also made to check whether the Findley power law model predicts properly the creep of our systems. Figure 4.44 depicts the constructed master curves along with their Findley fits. The parameters of the Findley power law (cf. Equ.1.10) were listed in Table 4.4. Figure 4.44 shows that the above power law function holds for the POM/PU binary blends and POM/PU/alumina ternary composites produced by different methods. The creep results, when summarized in compliance vs. time master curves, proved to be slightly different for the DM and MB composites. The MB produced composite exhibited better creep resistance than the DM one for long term.

The rather small improvement in the creep resistance due to the alumina content is likely linked with the fact that the initially high crystallinity of the POM was practically not influenced by the additives (PU and alumina). The related finding suggests further, that the resistance to creep of the ternary systems is mostly governed by the PU phase.

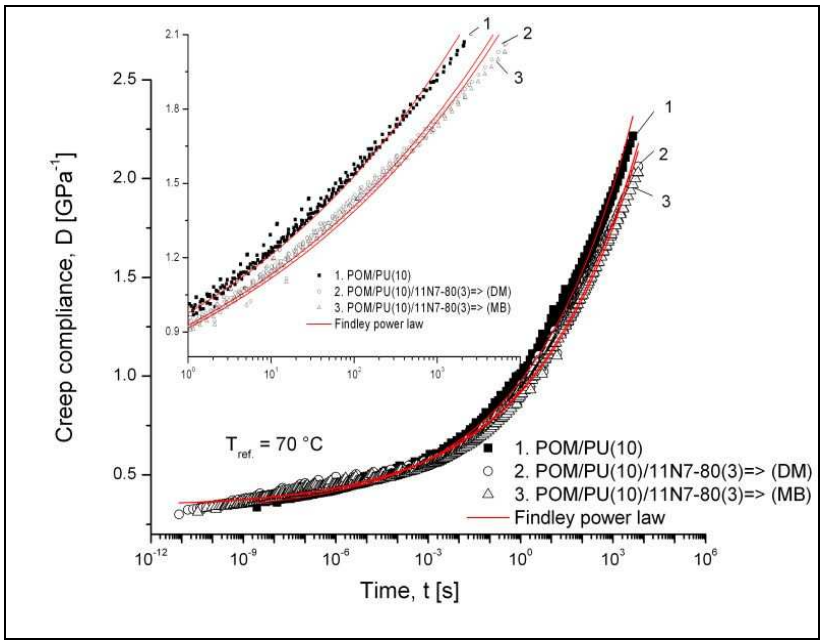

Figure 4.44: Creep master curves (compliance vs. time) constructed by considering T_0=70 °C and the related fits based on the Findley p rediction

Table 4.4: Findley parameters for the creep mastercurves of the POM-based systems studied

Sample Designation	**D_{F0}**(GPa^{-1})	**D_{F1}**(GPa^{-1}s$^{1/n}$)	**n**
POM/PU(10)	0.308	0.667	0.131
POM/PU(10)/11N7-80(3)=>(DM)	0.336	0.590	0.129
POM/PU(10)/11N7-80(3)=>(MB)	0.332	0.583	0.128

4.1.3.6 Rheology

The shear viscosity of POM, POM/PU blend, POM/PU/alumina produced by MB and DM is shown in Figure 4.45. POM shows the presence of a linear viscoelastic region in the viscosity vs. angular frequency curve. The shape of the viscosity curves of the composites prepared by MB is very similar to that of the POM/PU blend. On the other hand, the viscosity values of the composites produced by DM are always higher than those prepared by MB, albeit the difference is relatively high only at low angular frequencies. This is attributed to the large difference in the alumina dispersion between the composites produced by DM and MB, respectively. In the DM microcomposites the alumina particles are separated from PU phase and coarsely dispersed in the POM (cf. Fig. 4.34b). On the other hand, the alumina particles are likely also dispersed in the PU phase in the MB nanocomposite. This assumption is in line with the rheological results in Figure 4.45, which were found reproducible.

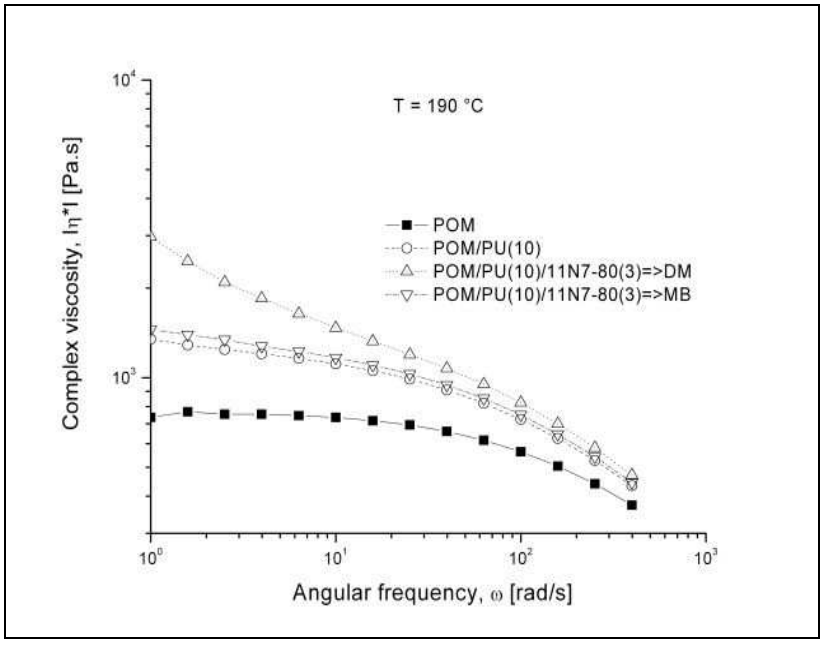

Figure 4.45: Melt viscosity vs angular frequency of the systems studied at T=190 °C

4.1.3.7 Dielectric Properties

Figure 4.46 presents the dependence of the dielectric permittivity (ε') and dissipation factor (tan δ) on the frequency, measured at room temperature for all the examined specimens. The dielectric permittivity and dissipation factor attain high values at the low frequency edge, which are decreasing steeply with increasing frequency. Considering the insulating nature of the examined systems, the enhanced values in the low frequency range indicate the co-existence of electrode polarization and interfacial relaxation phenomena. Electrode polarization is an undesirable effect related to the charged electrode-specimen contacts. Interfacial polarization (IP) or Maxwell-Wagner-Sillars (MWS) effects are present in heterogeneous systems because of the accumulation of mobile charges at the interfaces of the composite [99-102]. Separating the contribution of each effect is not an easy procedure in the dielectric permittivity mode and thus the electric modulus formalism will be employed for the interpretation of dielectric data.

Electric modulus is defined as the inverse quantity of complex permittivity by the following equation:

$$M^* = \frac{1}{\varepsilon^*} = \frac{1}{\varepsilon' - j\varepsilon''} = \frac{\varepsilon'}{\varepsilon'^2 + \varepsilon''^2} + j\frac{\varepsilon''}{\varepsilon'^2 + \varepsilon''^2} = M' + jM'' \qquad (4.1)$$

where ε', M' are the real and ε'', M'' the imaginary parts of dielectric permittivity and electric modulus, respectively. Electric modulus presentation offers some advantages in the interpretation of bulk relaxation processes in complex systems, since the large variation in the permittivity and loss at low frequencies is minimized and difficulties occurring from the electrode-specimen contact due to the injection of space charges and absorbed impurities can be neglected [103-104]. The electric modulus formalism has been successfully employed for the description of electrical relaxation phenomena in both micro- and nanocomposites (e.g. [104]).

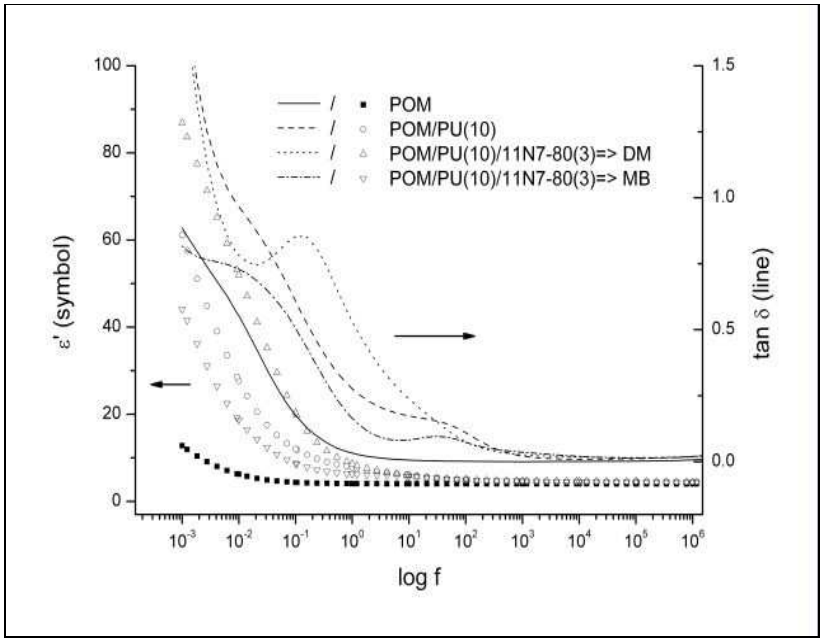

Figure 4.46: ε' (separate symbols) vs. frequency (f) and tan δ (line functions) vs. f traces for the systems studied

Figures 4.47a-4.47b depict the real and imaginary part of electric modulus (M', M'') as a function of frequency for POM, POM/PU blend and the composites of alumina particles produced by various methods. The real part of electric modulus (M') as a function of frequency undergoes a step-like transition from low to high values for POM. On other hand the POM/PU blend and the MB and DM composites exhibit two step-like transitions. These transitions imply the presence of relaxation processes. They become evident as loss peaks in the corresponding M'' vs. frequency curves. In the dielectric spectrum (M'' vs. frequency) of pure POM a single peak is recorded, assigned to the α-relaxation (cf. Fig. 4.47b). In the dielectric spectrum of POM three transitions are expected to occur in accordance to the DMTA results. However, only the slower transition is recorded in the examined frequency range at ambient. Secondary modes (β and γ-relaxations) are characterized by relatively lower relaxation times and thus they should be detected at lower temperatures (in isochronal scans) or higher frequencies (in isothermal scans) [105-106]. The recorded α-relaxation process is often attributed to rearrangements in the crystalline parts of POM, although contributions from the amorphous phase can not be excluded [105, 107]. PU has a peak at 100 Hz (not shown here), related to its glass/rubber transition, and tends to form a second one at the high frequency edge, which is assigned to the re-

orientation of polar side groups of the main chain [52, 108]. The dielectric spectra of the nanocomposites and the blend include the contributions of both polymers. It has to be mentioned that an analogous dielectric behavior has already been reported for alumina nanoparticles dispersed in polyurethane rubber, through latex compounding, systems [52]. Moreover, the peak of neat POM (α-relaxation), recorded in the vicinity of 0.01 Hz, seems to shift towards higher frequencies in all other systems (cf. Fig. 4.47b). By contrast, no such behavior is evident in the DMTA results (cf. Fig. 4.36). Differences between the dielectric and the DMTA traces in crystalline polymers have been reported previously [105, 107]. Finally, in the loss spectra of the complex systems a small hump can be recognized in the low frequency edge, occurring from interfacial polarization.

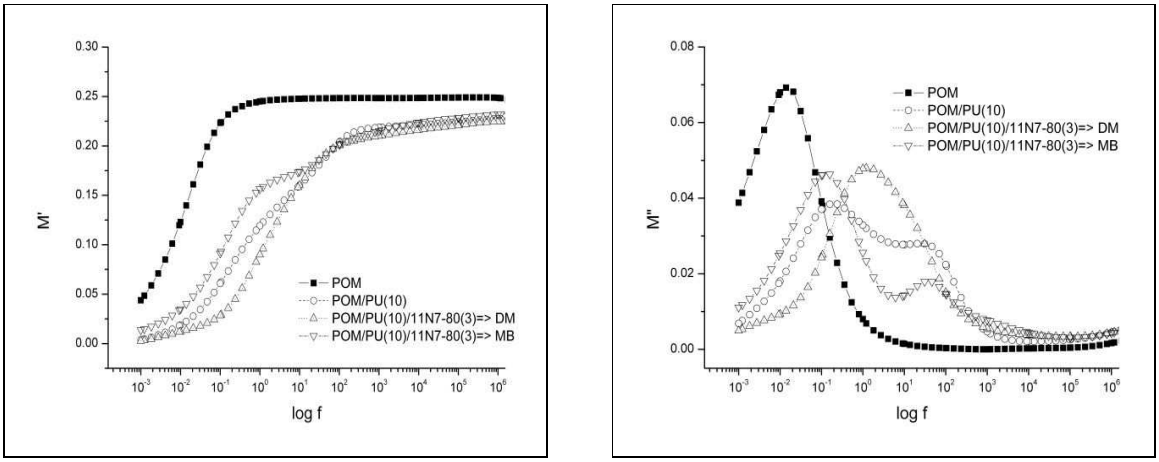

a) b)

Figure 4.47: (a) Real (M') and (b) imaginary part (M'') vs. frequency traces for the POM, POM/PU blends and POM/PU/alumina composites produced by various methods

4.1.3.8 Long-term Creep Behavior

The creep curves of long-term test at 50 °C of POM/PU blend and the alumina-containing ternary composites produced by DM and MBa methods are shown in Figure 4.48 for constant stress at 20 MPa, 15 MPa and 6 MPa, respectively. The creep strain increases with increasing stress level. On the other hand, one can recognize that the creep strain decreased markedly for the POM/PU/11N7-80 composites produced by MBa. The reduction was most prominent at the stress of 20 MPa. Interestingly, when the stress increased from 15 MPa to 20 MPa, the creep strain increased more than 200% for both composites produced by different techniques.

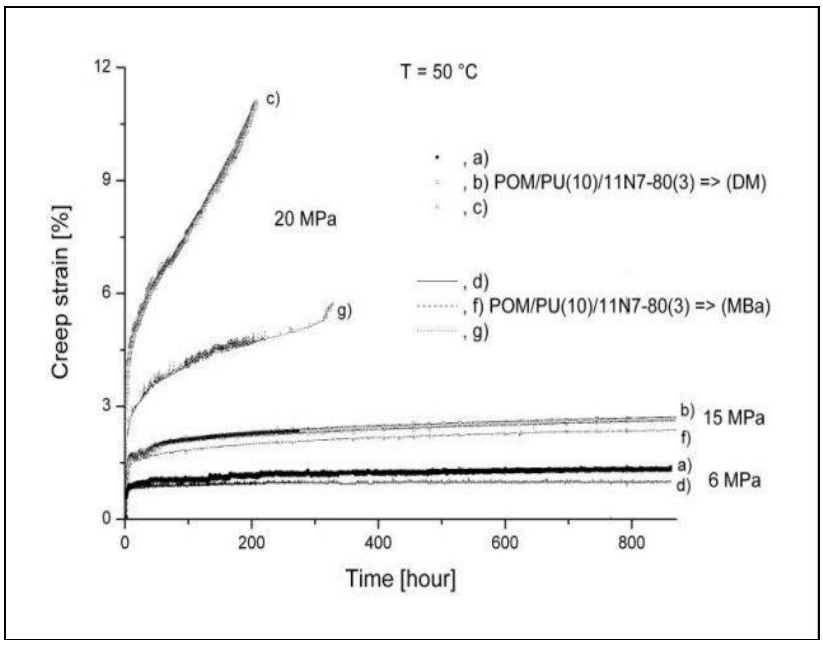

Figure: 4.48: Creep strain of POM/PU/alumina composites produced by DM and MBa at T=50 °C and different of stress levels (20 MPa, 15 MPa and 6 MPa)

By using the power law model from equation 1.10 the creep behavior at 50 °C was described at different stress levels set (cf. Figure 4.49a-4.49c). As continuous line drawn for the creep data indicates that the power law approach is a proper tool to describe the observed results. However, at 20 MPa stress (Figure 49c) the Findley model deviates from the experiment data in case of DM composite in a larger extent, whereas the fit is acceptable line for the MBa. This difference is likely liked with the

dispersion stage of alumina as discussed in section 4.1.3.1 (Alumina agglomerates of several microns were found which effect is amplified at the high stress levels).

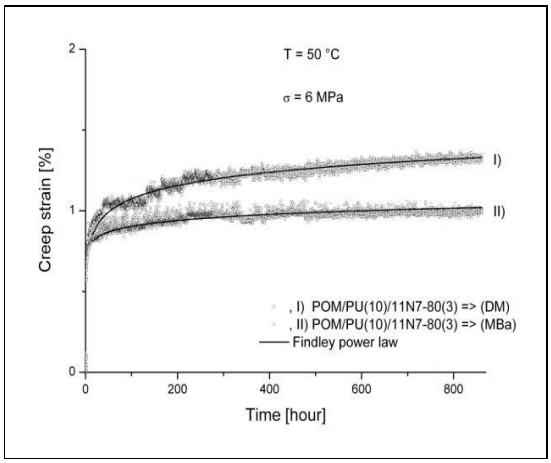

a)

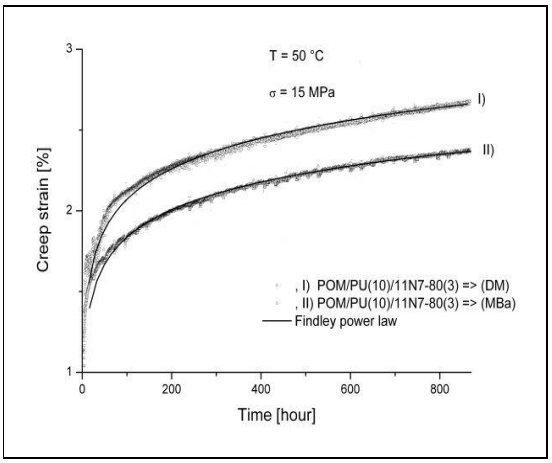

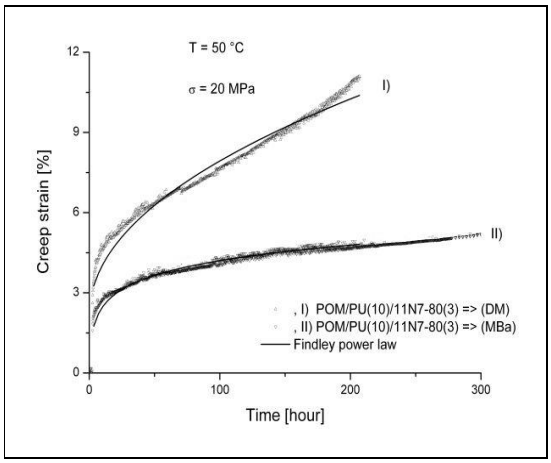

b) c)

Figure 4.49: Effect of stress level on the tensile creep of POM/PU/alumina composites produced by DM and MBa at 6 MPa (a), 15 MPa (b) and 20 MPa stress (c), respectively, and the related Findley fits

In section 4.1.3.5 we have reported both the experimental and the Findley model-predicted creep compliances as functions of time. Note that in that case the TTS was adopted for the experimental short-term creep compliances of POM/PU/alumina composites. Now we have the possibility to compare the predicted (from short-term experiments and experimental from long-term tests) creep responses of the DM

composite at 6 MPa stress. Note that the corresponding specimens were produced by the same techniques (DM), only the dimension of the specimens differed in the short- and long-term creep experiments. Using short-term creep data (section 4.1.3.5) master curves were constructed by considering TTS for T=50 ° C, Figure 4.50. This Figure also contains the long term-tensile creep of POM/PU/alumina composite produced by the same i.e. DM method. The significant departure of the long term response from the model prediction based on short-term creep can be assigned to material-related changes during the corresponding tensile creep tests. Note that the heating rate has also changed the crystallinity and/or the structure of the crystalline phase. Recall that, the proportion of the viscoelastic, elastic, and plastic characteristics depends strongly on the molecular structure including crystallinity. On the other hand, under long-term loading, stiffness will decrease progressively with time and stress and strain levels in the material will be very different from values calculated using property data obtained from tests of short duration. Moreover, during long-term test, the material can suffer substantial physical aging. Except for the actual creep strain value, the theoretical prediction yielded a good agreement with results of the long-term creep tests. However, the difference of ca. 20% between the predicted and test results is still acceptable for engineering purposes.

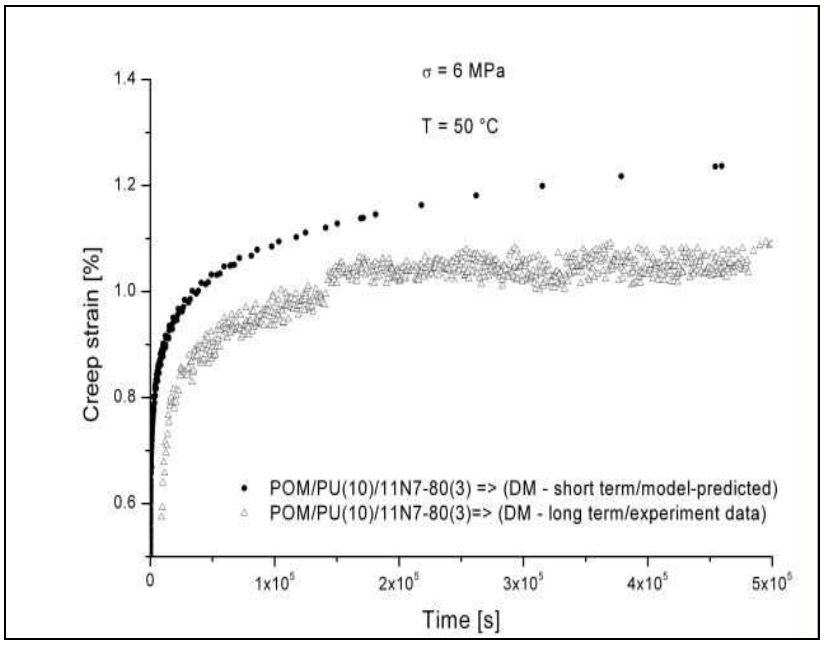

Figure 4.50: Theoretical and experimental creep data for the DM composite at an applied stress of 6 MPa

It is clear from the above results that the masterbatch technique enhances the performance of the nanocomposites and special attention should be paid to its practical relevance. It can be concluded that latex-mediated incorporation of nanoparticles is a straightforward and safe way to produce thermoplastic based nanocomposites with and without additional rubber toughening. Further, this technique is highly suitable for on-line extrusion compounding. By this way one can reduce the production costs of the composite materials by avoiding the expensive chemical modification of the nanofillers. Therefore the next chapter deals with the feasibility of the related processing technology, i.e. with the water-mediated dispersion of nanoparticles and toughness via a continuous extrusion process.

4.2 Continuously Produced Reinforced and/or Toughened Polymer Composites

4.2.1 Alumina-Filled Polystyrene Composites

4.2.1.1 Structure

As already seen from the results in chapter 4.1, the mechanical properties depend on the morphology for multiphase materials. The properties of the final composite material are mostly dependent on the characteristics of the dispersed phase. Figures 4.51a and 4.52a show the microstructure of PS/alumina composite produced by direct melt mixing (DM). Figures 4.51b and 4.52b show the nanostructure of the same composite produced the continuous by extrusion composite technique (CT) whereby the filler was introduced in water slurry in the PS melt. Many large agglomerates (> 1 µm) of the alumina particles could be observed in the samples prepared by DM, indicating that the shear provided during compounding was not effective to break these agglomerates of the alumina particles. On the other hand, the composites prepared via water-mediated technique presented a much better dispersed homogeneous morphology and the particle size was well dispersed in a nanometric scale.

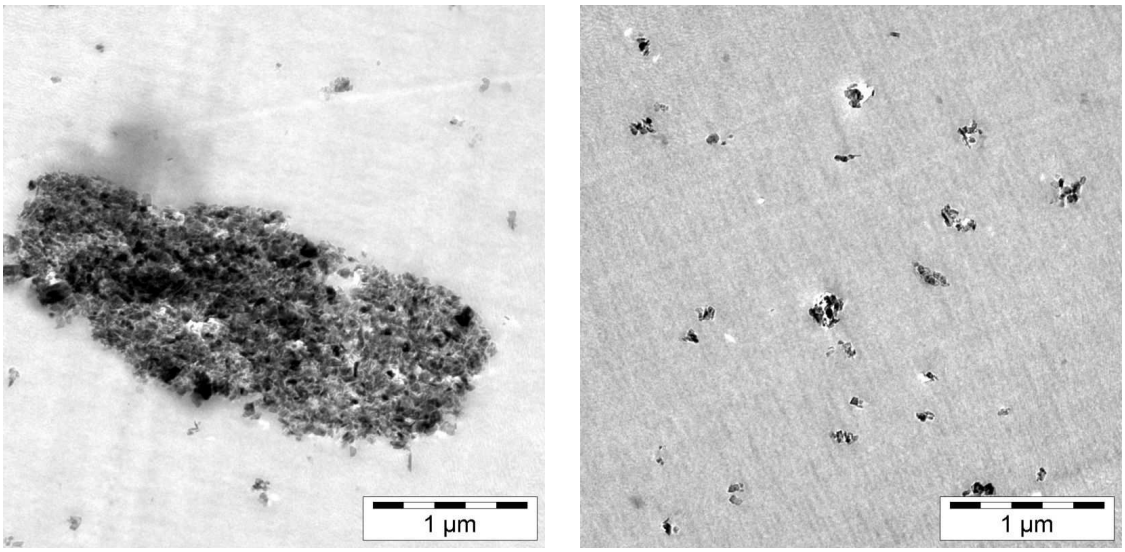

a) b)

Figure 4.51: TEM pictures of PS/alumina (11N7-80) composites produced continuously by (a) direct melt compounding (DM-CT) and (b) water-mediated technique (WM-CT). Note: alumina content was 3 wt.%

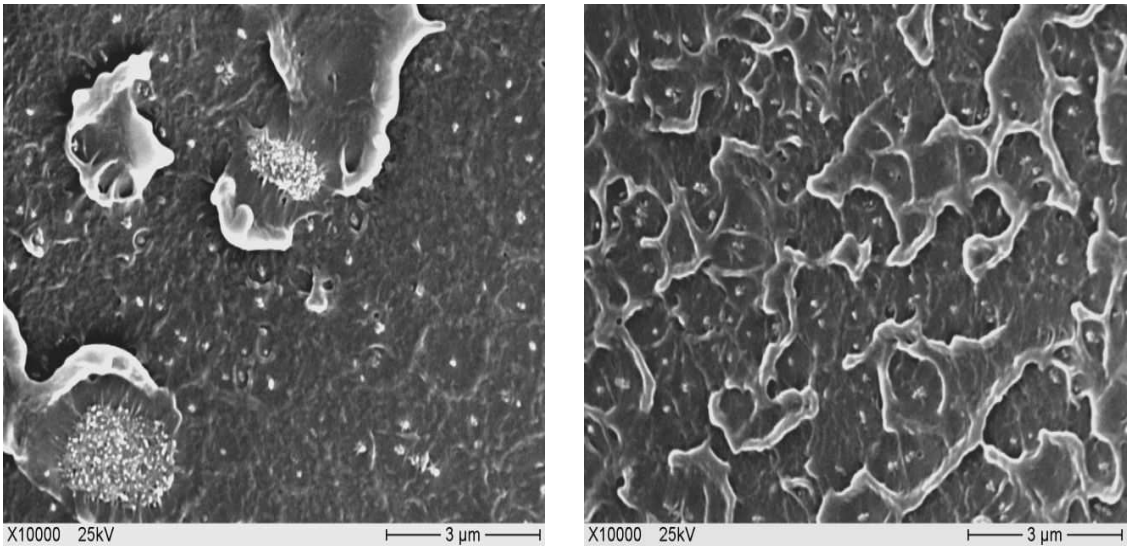

a) b)

Figure 4.52: SEM pictures of PS/alumina (11N7-80) composites produced continuously by (a) direct melt compounding (DM-CT) and (b) water-mediated technique (WM-CT). Note: alumina content was 3 wt.%

4.2.1.2 Thermal Mechanical Properties

Figure 4.53a and b depict the storage (E'), tan δ and loss moduli (E'') as a function of temperature for PS and its composites with alumina particles produced by various methods. One can notice that the storage modulus of the composites is enhanced by adding alumina compared to PS in the whole temperature range. It is also well resolved that the stiffness of those alumina composites produced by WM technique is always inferior to those composites produced by DM. This behavior can be explained by considering the small-sized particle distribution in the PS matrix, as shown in TEM analysis (cf. Figure 4.51b). A higher value of loss modulus is observed in composite produced by CT compared to microcomposite produced by DM (cf. Figure 4.53b). This hike in loss modulus is attributed to the improved interaction between PS and alumina particles by homogeneous dispersion.

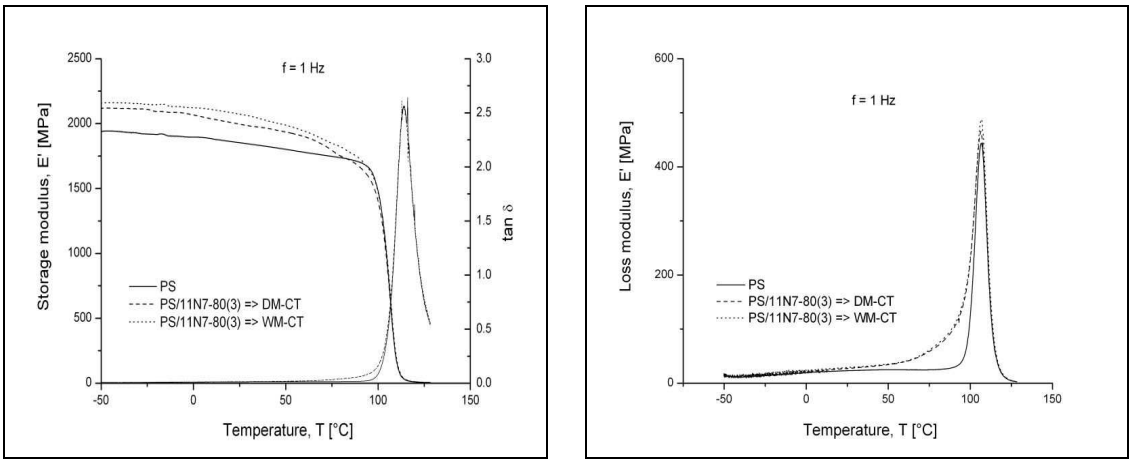

a) b)

Figure 4.53: E' vs. T and tan δ vs. T (a) and E'' vs. T (b) traces for the PS and its alumina composites (3 wt.%) prepared by DM-CT and WM-CT

4.2.1.3 Tensile Properties

Generally, the addition of rigid particles to a thermoplastics material results in increase in stiffness, although by sacrificing of the ductility elongation at break is reduced [109]. A similar behavior was observed by incorporating alumina in PS matrix. The tensile mechanical data i.e. stiffness, strength and elongation at break are listed in Table 4.5. Note that the tensile modulus of the composites is higher than that of the PS. Data in table confirm that the nanocomposites produced by WM-CT possess higher tensile modulus and strength than DM-CT versions. This observation supports again that this WM-CT method can effectively avoid the agglomeration of alumina particles and thus yield improved stiffness and strength. Table 4.5 shows also the HDT values of the composites (93 °C) are enhanced beyond that of the PS (84 °C), however, did not reflect the effects of composite manufacturing.

Table 4.5: Tensile mechanical characteristics of the PS and Alumina-reinforced PS composites (alumina content: 3wt.%) prepared by various methods

Sample Designation	Tensile strength [MPa]	Tensile modulus [MPa]	Elongation at break [%]	HDT [°C]
PS	41± 0.6	3134±156	2.9±0.2	84.7
PS/11N7-80(3)=>DM-CT	47± 0.7	3201±133	1.6±0.1	93.1
PS/11N7-80(3)=>WM-CT	49± 0.9	3362±62	1.6±0.1	93.5

4.2.1.4 Impact Properties

Figure 4.54 displays the impact energy values for the PS and its composites produced by DM-CT and WM-CT. The toughness of the PS composites was markedly reduced (~ 55 % compared to the PS). Moreover, the composite produced by DM-CT exhibits higher impact energy compared to the nanocomposite produced by WM-CT. The reduction in the toughness of the composites is due to the reinforcing effect of the alumina particles and reflects well that the toughness change correlates with that of the ductility (elongation of break) in the first approximation. Moreover, the better dispersion grade of the alumina (WM-CT>DM-CT), the lower the impact toughness is.

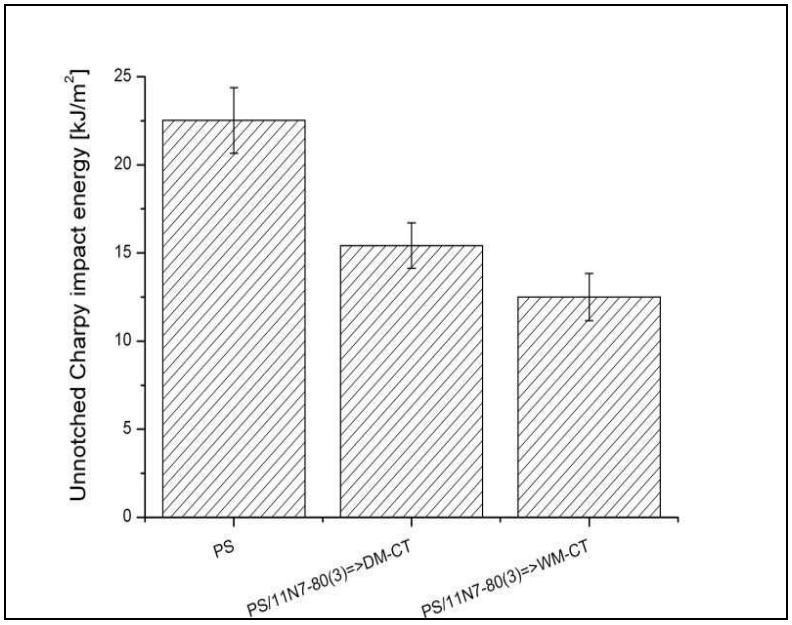

Figure 4.54: Unnotched Charpy impact energy at room temperature for the PS and its alumina composites prepared by different methods

4.2.1.5 Viscoelastic behavior

Figure 4.55 displays the creep compliance and simulated fits according to the Burgers model for the PS and its composites produced by DM-CT and WM-CT. The solid lines appearing in each curve represents the calculated data using the Burgers model. The related parameters derived for each fit using the related software package of the DMTA device (Rheology Advantage Data Analysis) are listed in Table 4.6. For these data, the applied stress was set at 3 MPa. It is clear from the figure that the creep compliance values of composites produced by both techniques are lower compared to the PS. For the composites containing 3 wt.% alumina for example the creep compliance was reduced by ~ 22 % compared to the PS when produced by WM-CT (cf. Figure 4.55). The creep compliance increases with increasing temperature but the shape of creep curves for all the samples remains similar. One can also recognize that the creep of composites decreased remarkably when using WM-CT instead of DM-CT. This may be attributed to a better dispersion of the alumina as discussed before. This should be associated with the formation of an interphase with reduced molecular mobility and thus enhancing the resistance to creep.

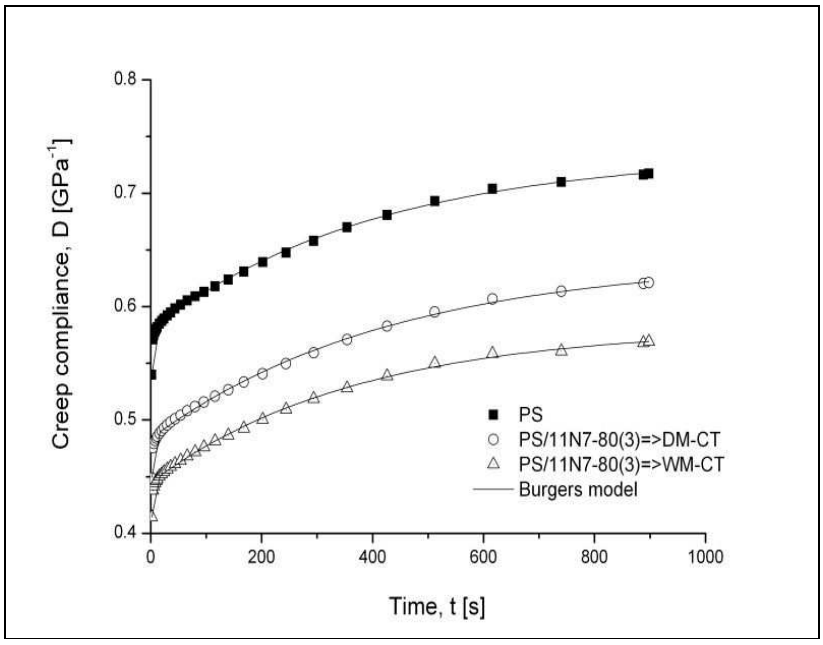

Figure 4.55: Creep of PS and its alumina composites prepared by different methods at temperature of 40 °C. Experimental data were fitted by the Burgers model (solid lines)

Table 4.6: Burgers parameters for the creep of the PS and its alumina composites prepared by different methods studied

Temperature	Parameter	PS	PS/11N7-80(3)=>DM	PS/11N7-80(3)=>CT
40 °C	D_0 (Pa^{-1})	$5.6*10^{-14}$	$1.84*10^{-11}$	$2.27*10^{-10}$
	D_{k1} (Pa^{-1})	$1.39*10^{-10}$	$1.4*10^{-10}$	$1.11*10^{-10}$
	τ_1 (s)	397.4	419.2	309.2
	D_{k2} (Pa^{-1})	$1.37*10^{-11}$	$1.35*10^{-11}$	$6.79*10^{-11}$
	τ_2 (s)	11.10	10.33	2.02
	D_{k3} (Pa^{-1})	$7.83*10^{-11}$	$1.72*10^{-10}$	$1.35*10^{-12}$
	τ_3 (s)	0.03	0.82	0.09
	D_{k4} (Pa^{-1})	$4.46*10^{-10}$	$2.55*10^{-11}$	$1.25*10^{-10}$
	τ_4 (s)	0.69	1.44	0.59
	D_{k5} (Pa^{-1})	$2.33*10^{-11}$	$1.44*10^{-10}$	$1.09*10^{-12}$
	τ_5 (s)	1.36	0.31	0.9
	D_{k6} (Pa^{-1})	$2.1*10^{-11}$	$1.13*10^{-10}$	$2.23*10^{-11}$
	τ_6 (s)	1.29	0.73	1.03
	μ_0 (Pa.s)	$7.27*10^{13}$	$6.67*10^{13}$	$4.24*10^{13}$

Figures 4.56a-b demonstrate the effects of increased temperature on the creep response of PS and its composite produced by WM-CT. The creep compliance increases with increasing temperature. Note that the creep compliance decreased markedly for the PS/11N7-80 composite produced by WM-CT at the all test temperature.

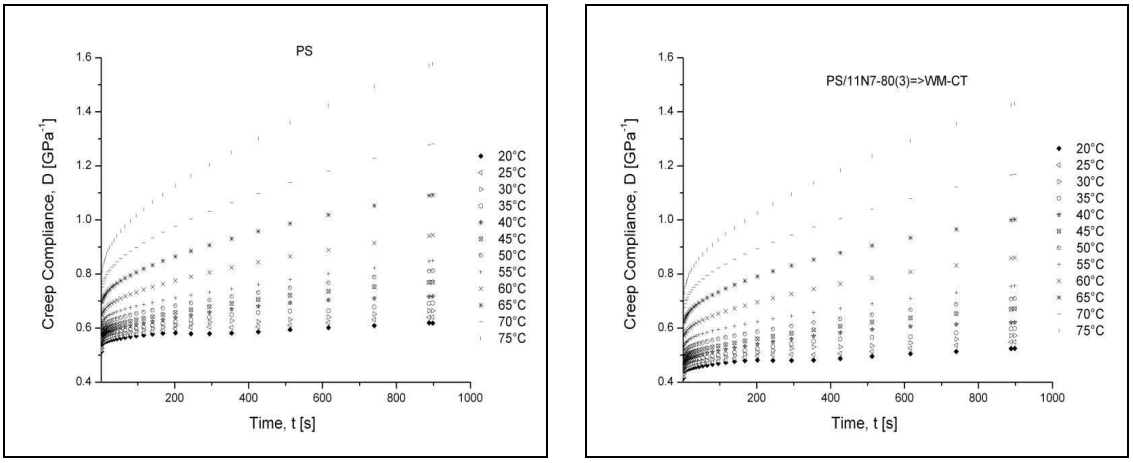

a) b)

Figure 4.56: Effect of temperature on the tensile creep of PS (a), and for the composite produced by WM-CT (b)

The shift factor, a_T was obtained directly from the experimental creep curves as a function of the temperature. Recall that they have been considered to create the corresponding creep master curves by adopting the TTS principle. The shift factors used for the generation of creep master curve are shown in Figure 4.57.

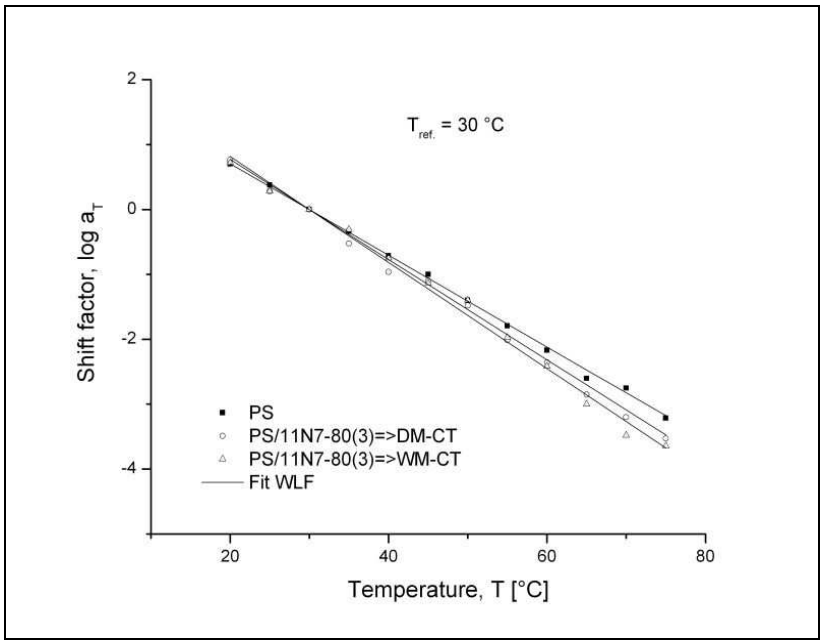

Figure 4.57: Experimental shift factors along with the related WLF fits in the temperature range T= 20 °C…75 °C for the systems studied

A reference temperature (T_0=30 °C) was used for this superposition process. The classical Findley power law used also to describe the creep compliance of experimental data. Figure 4.58 shows the constructed master curves along with their Findley fits. As it was expected, the creep resistance was improved by presence of alumina particles. The parameters of the Findley power law were listed in Table 4.7. It was found that the Findley power law model is suitable to describe the time dependence creep compliance of PS-based composites at least for 200 hours.

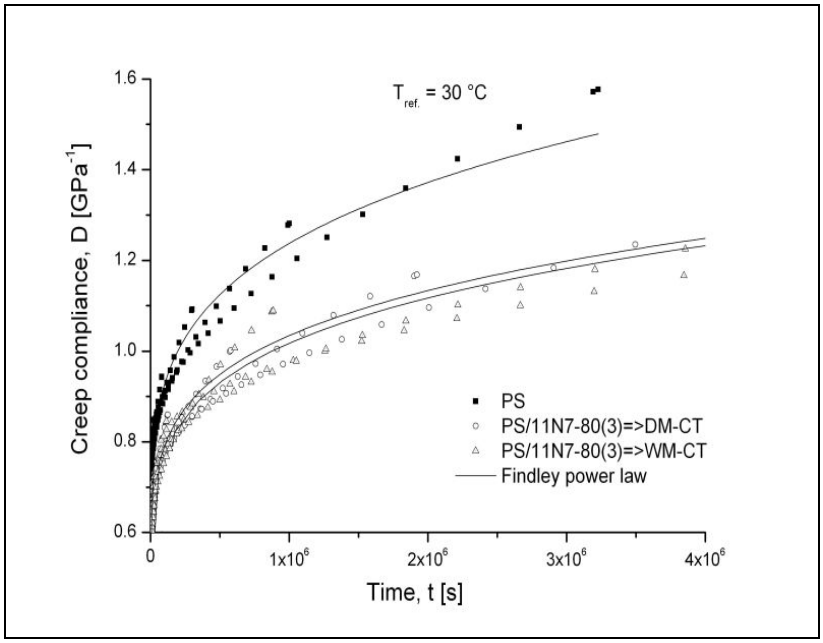

Figure 4.58: Creep master curves (creep compliance vs. time) constructed by considering $T_{ref.}$= 30 °C for the PS based systems

Table 4.7: Findley parameters for the creep mastercurves of the PS-based systems produced by DM-CT and WM-CT, studied

Sample Designation	**D_{F0}**(GPa^{-1})	**D_{F1}**($GPa^{-1}s^{1/n}$)	**n**
PS	0.53	0.02	0.249
PS/11N7-80(3)=>DM-CT	0.41	0.03	0.214
PS/11N7-80(3)=>WM-CT	0.38	0.03	0.208

4.2.1.6 Rheology

The shear viscosity of PS and its composite produced by DM-CT and WM-CT is shown in Figure 4.59. The shape of the viscosity curves of the composites is very similar to that of the pure PS. Note, the viscosity values of the composites with 3 wt.% of alumina particles produced by DM-CT and WM-CT are slightly higher than those of PS. On the other hand, the effect of composite preparation is marginal.

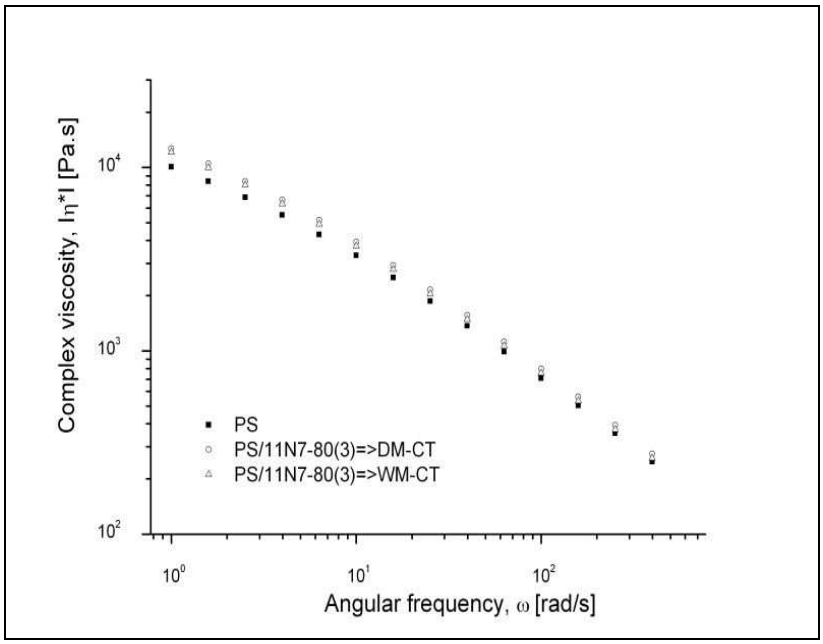

Figure 4.59: Viscosity vs. angular frequency for PS and its alumina composites prepared by different methods at T=180 °C

A discussion overview of PS based composite techniques is given in section 4.2.1. The mechanical and thermomechanical properties of the composites produced by WM-CT were superior to those prepared by DM-CT. In the continuing section we demonstrate the feasibility of the WM-CT concept on the example of the POM based composite system.

4.2.2 Polyoxymethylene/Polyurethane/Alumina ternary Composites

POM/alumina and POM/PU binary, and POM/PU/alumina ternary composites were also produced by the WM-CT method. Their structure-property relationships will be disclosed next.

4.2.2.1 Morphology

The XRD patterns of the POM, POM/alumina produced by DM-CT and WM-CT, respectively, are shown in Figure 4.60. XRD pattern of POM revealed three distinct peaks. Three additional peaks at $2\theta = 14.5$, 28.2 and 38.4 can be observed by the incorporation of alumina particles to POM matrix. Typical intensity of the boehmite signal ($2\theta = 14.5$) was increased for larger crystallite sizes. Most likely, the larger crystallites afforded higher boehmite crystallinity with respect to that of the smaller crystallites [89]. However, no difference was observed between the composites produced by DM-CT and WM-CT.

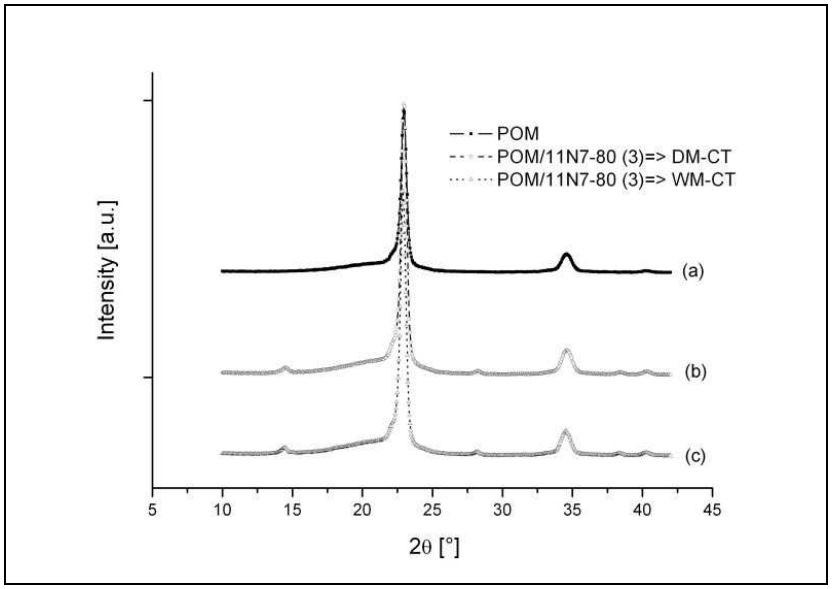

Figure 4.60: XRD spectra of POM (a), the composites produced by direct melt compounding (b) and continuous technique (c)

Figures 4.61a-4.61d, compare the spherulitic structures of POM, POM/PU blend and POM/PU/alumina ternary composites produced by continuous technique. The large spherulitic size of POM is still remarkable which becomes disturbed by addition PU. However, the spherulite structure is similar when compared the POM-based composites produced discontinuously. Therefore, it can be concluded that the crystalline structure of POM was not changed by incorporating the alumina slurry or PU latex though water-mediated technique.

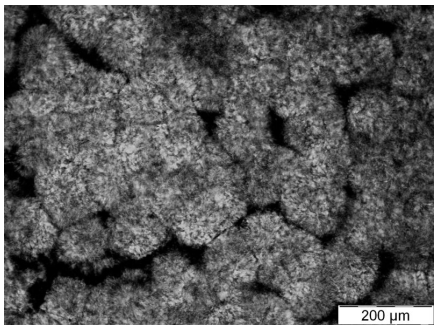

a)

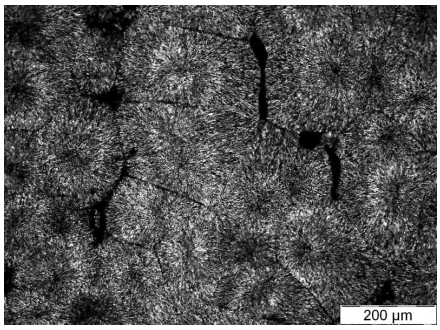

b)

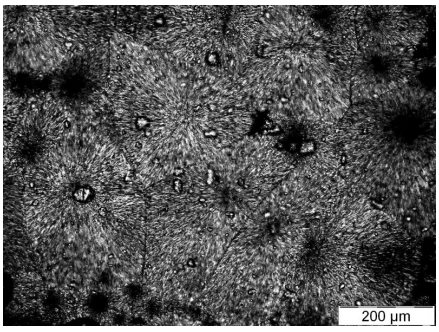

c)

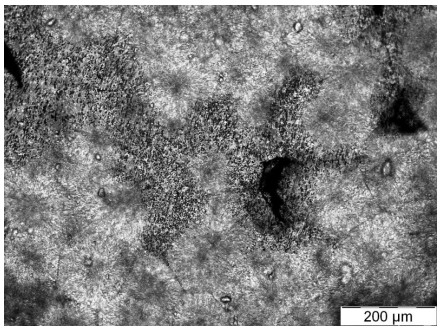

d)

Figure 4.61: PLM pictures of the isothermally crystallized POM (a), POM/PU blend (b), POM/11N780 (c) and POM/PU/11N7-80 (d) composites produced by continuous technique

TEM and SEM photographs taken of the POM/alumina composites, POM/PU blend and POM/PU/alumina ternary composites prepared continuously are shown in Figure 4.62-4.64, respectively. SEM pictures taken from the fracture surfaces of tensile loaded specimens give further insight in the alumina and PU dispersions. This is due to the larger view-field in SEM compared to TEM. Figure 4.62a and b show that the

alumina particles are nano-scaled and homogeneously dispersed in the matrix. Figure 4.63a and b demonstrate that the rubber particles are also well dispersed in the POM matrix. The mean diameter of the PU is between 700 and 900 nm, which is closely matched with the initial size of the PU particles in the corresponding latex. The above mentioned results support the effective dispersion of the alumina and rubber particles in nanoscale range using the continuous on-line compounding. Note that the dispersed rubber particle size in the POM/PU blend produced discontinuously (section 4.1.3) was clearly larger compared to the present on-line technique. In the POM/PU/alumina ternary composites (cf. Figure 4.64a), alumina particles are mainly in the PU. On the other hand, the alumina and rubber particles are also separately dispersed in the POM matrix based on SEM (cf. Figure 4.64b).

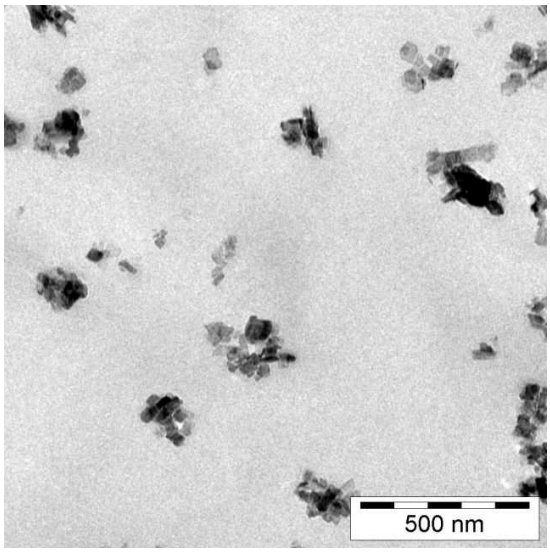

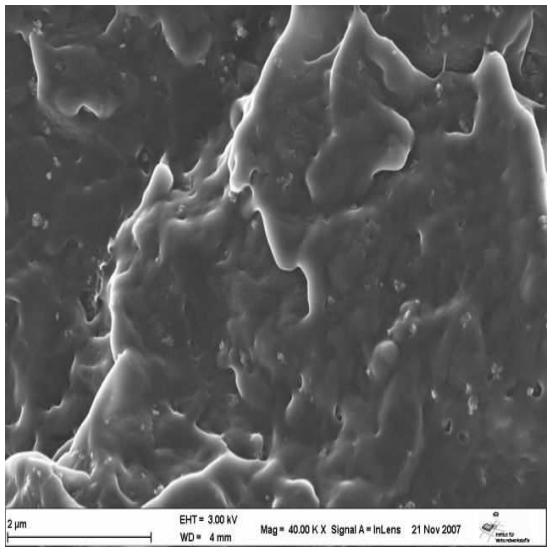

a) b)

Figure 4.62: Structure of the POM/alumina composite produced by WM-CT (a) TEM (b) SEM

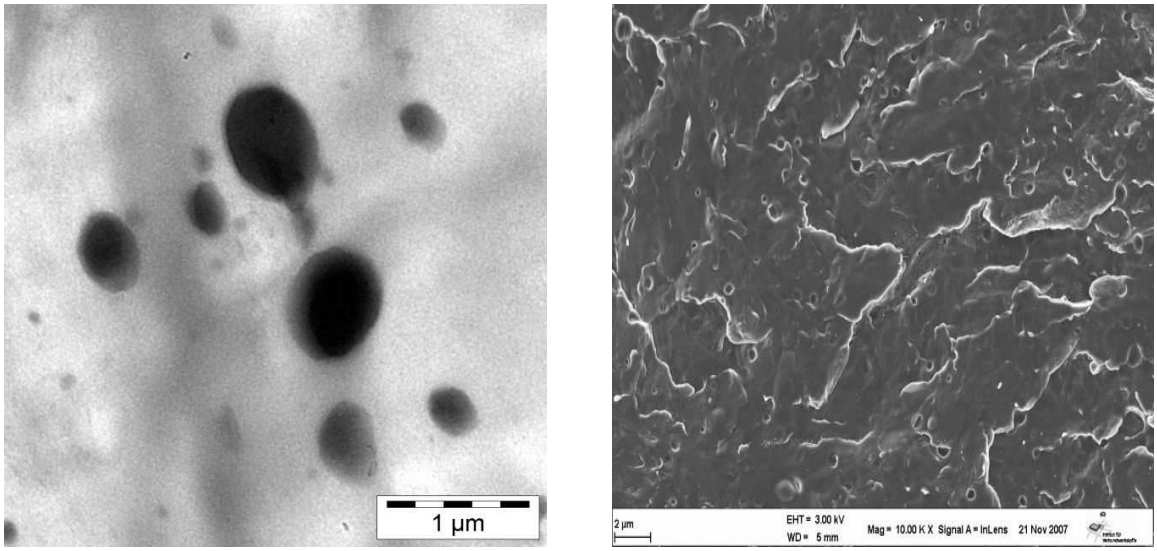

a) b)

Figure 4.63: Structure of the POM/PU blend produced by WM-CT (a) TEM (b) SEM

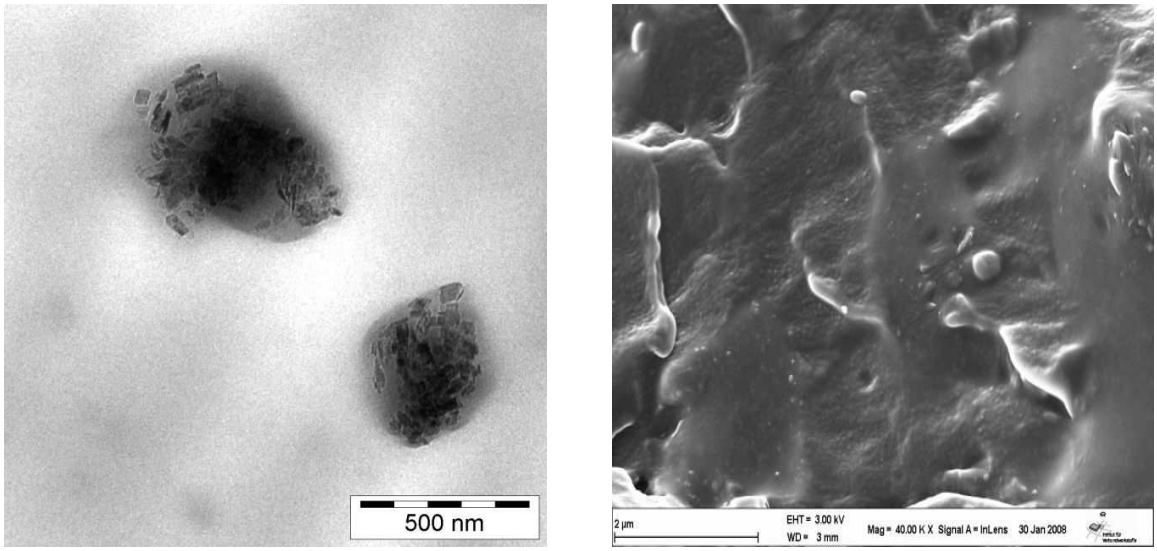

a) b)

Figure 4.64: Structure of the POM/PU/alumina composite produced by WM-CT (a) TEM (b) SEM

4.2.2.2 Thermal Mechanical Properties

Thermal mechanical properties were analyzed using DMTA at fixed frequency 1Hz in the temperature range from -100 °C to 150 °C. The storage (E') storage (E'), tan δ and loss modulus as function of temperature were plotted as shown in Figure 4.65a and b, respectively. It can be seen from Figure 4.65a that the modulus E' of POM systems decreases with increasing temperature and the stiffness of the POM/PU blend was much lower than the POM. However, the incorporation of alumina particles resulted in some increase in the storage modulus in the whole temperature range, compared to that of the pure POM. This can be well explained by reinforcing effect of alumina particles leading to an increased stiffness. Figure 4.65b also shows that the blend containing 10 wt.% of PU exhibited higher loss modulus. The addition of PU, which is an amorphous polymer, to the semicrystalline POM matrix results in increased loss modulus.

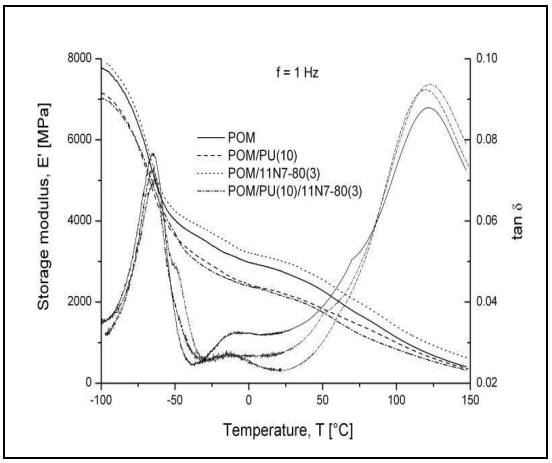

a)

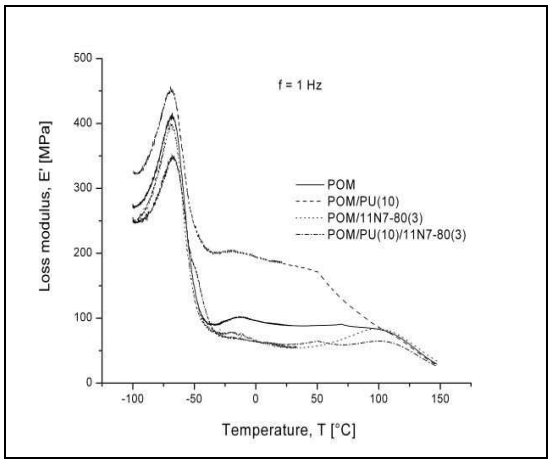

b)

Figure 4.65: E' vs. T and tan δ vs. T (a) and E'' vs. T (b) traces for the POM systems prepared by WM-CT

4.2.2.3 Tensile Properties

Results of the tensile mechanical tests are given in Table 4.8. It is clear by seen that the incorporation of alumina and PU particles strongly affected the mechanical behavior of POM. Adding alumina increased the stiffness, slightly reduced the strength, the elongation at break. Conversely, the ductility of the POM/PU blend increased and the stiffness and strength decreased compared to pure POM. The reduction in the tensile strength may be attributed to the presence of rubber particles acting as stress concentrators and forcing the yielding at lower stresses. The decrease in the tensile modulus in the POM/PU blend may be accounted for the softening effect of PU, since the tensile modulus of rubber is considerably lower than that of the pure POM. The POM/PU/alumina ternary composites exhibited significant decrease in modulus accompanied by much higher elongation at break as compared to the POM, POM/alumina composite and POM/PU blend.

Table 4.8: Tensile mechanical characteristics of the POM and alumina-reinforced/toughened injection molded POM composites prepared by WM-CT

Sample Designation	Tensile strength [MPa]	Tensile modulus [MPa]	Elongation at break [%]
POM	63± 0.2	2646±71	17.8±2.8
POM/PU(10)	55± 0.2	2392±101	31.9±4.5
POM/11N7-80(3)	61± 0.1	2847±143	9.1±2.8
POM/PU(10)/11N7-80(3)	47± 0.5	2323±62	57.1±8

4.2.2.4 Impact Properties

Figure 4.66 shows the impact energy of POM, POM/PU blend and the composites with alumina particles produced by WM-CT. Even though the tensile modulus of POM is increased by the incorporation of rigid alumina particles, the toughness was reduced. However, POM modified with 10 wt.% PU exhibit not only higher elongation at break, but similarly also higher impact energy (~ 22 %) compared to the pure POM. This is due to the submicron dispersion of the rubber particles. So, the incorporation of rubbery particles in a suitable size range increases the impact resistance of POM. Furthermore, the impact energy of POM/PU/alumina ternary composites was marginally decreased compared to the POM/PU blend but remained still higher than POM.

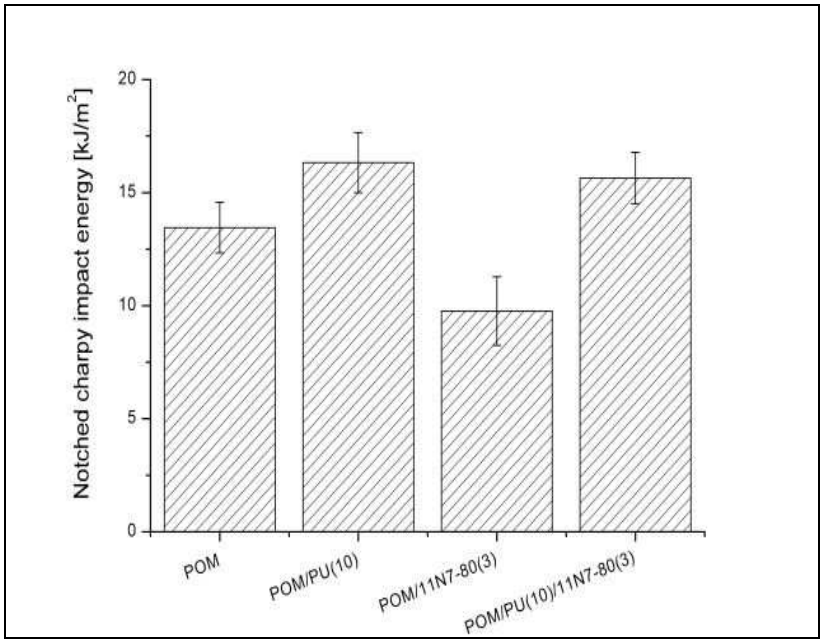

Figure 4.66: Notched Charpy impact energy at room temperature from POM systems prepared by WM-CT

4.2.2.5 Viscoelastic Behavior

Figures 4.67 displays the traces of the creep compliance and its simulated value using the Burgers model, as a function of time at T=30 °C for the POM, POM/alumina composite, POM/PU blend and the alumina-containing ternary composites produced by WM-CT. The incorporation of alumina particles into POM matrix resulted in a considerable decrease of the creep compliance, as expected owing to this reinforcing effect. Conversely, the addition of PU increased the creep of POM. The compliance

values were reduced by approx. 12 % compared to the POM/PU blend when alumina was introduced by the WM-CT. This creep response suggests that alumina particles are partly dispersed in the rubber domains and partly also in the POM matrix. This was supported by the SEM inspection (cf. Figure 4.64b).

Values of the parameters of the Burgers mode were determined for each curve using the related software package of the DMTA device (Rheology Advantage Data Analysis) and listed in Table 4.9. The highest instantaneous compliance (D_0) was observed when PU was added into the POM. As shown in Table 4.9, one can see that the instantaneous compliance of the POM/alumina composite is lower than those of the POM and POM/PU blend. The enhancement in the instantaneous part of compliance is caused by the alumina particles and their dispersed state. This resulted in a decrease in the polymer segments' mobility.

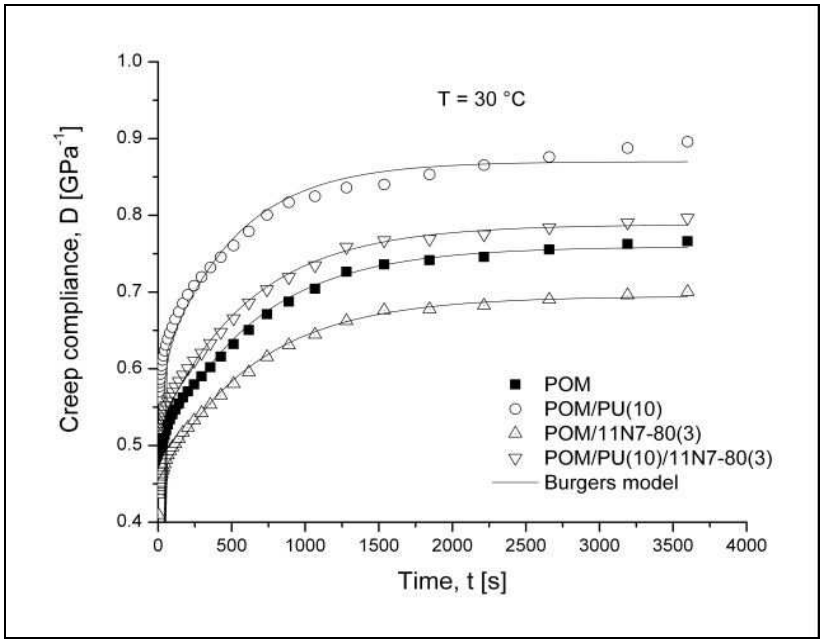

Figure 4.67: Creep of POM, POM/PU blend, POM/alumina- and POM/PU/alumina composites at T=30 °C (stress applied 6 MPa for t = 60 min). Experimental data were fitted also by Burgers approximation (see solid lines)

Table 4.9: Burgers parameters for the creep of the POM-based systems studied

Temperature	Parameter	POM	POM/PU(10)	POM/11N7-80(3)	POM/PU(10)/11N7-80(3)
30 °C	D_0 (Pa^{-1})	$3.63*10^{-10}$	$3.77*10^{-10}$	$2.58*10^{-10}$	$1.39*10^{-11}$
	D_{k1} (Pa^{-1})	$2.22*10^{-10}$	$2.15*10^{-10}$	$2.26*10^{-10}$	$2.39*10^{-10}$
	τ_1 (s)	626	451.6	690.3	615.6
	D_{k2} (Pa^{-1})	$4.01*10^{-11}$	$5.92*10^{-11}$	$5.66*10^{-11}$	$7.41*10^{-11}$
	τ_2 (s)	24.38	17.83	9.52	7.34
	D_{k3} (Pa^{-1})	$7.61*10^{-12}$	$4.24*10^{-12}$	$1.09*10^{-11}$	$3.72*10^{-10}$
	τ_3 (s)	0.15	4.19	0.22	0.04
	D_{k4} (Pa^{-1})	$1.29*10^{-15}$	$2.52*10^{-15}$	$2.09*10^{-11}$	$2.56*10^{-15}$
	τ_4 (s)	0.51	5.31	6.33	0.15
	D_{k5} (Pa^{-1})	$8.63*10^{-11}$	$1.41*10^{-10}$	$3.16*10^{-11}$	$6.98*10^{-11}$
	τ_5 (s)	1.77	1.47	0.07	0.02
	D_{k6} (Pa^{-1})	$9.09*10^{-12}$	$2.89*10^{-11}$	$8.53*10^{-11}$	$5.42*10^{-15}$
	τ_6 (s)	0.11	0.32	0.28	0.005
	μ_0 (Pa.s)	$8.25*10^{13}$	$5.41*10^{13}$	$3.68*10^{14}$	$1.38*10^{14}$

Figures 4.68a-4.68d, demonstrate the effects of increased temperature on the creep response of POM, POM/PU blend, POM/alumina binary- and POM/PU/alumina ternary composites. The creep of all POM system is sensitive to the effect of temperature. A more interesting observation is the relative change in the transient creep with respect to instantaneous creep as the temperature increases. Unlike to pure POM, the incorporation of 3 wt.% alumina particles reduced the creep compliance significantly, even under elevated temperatures.

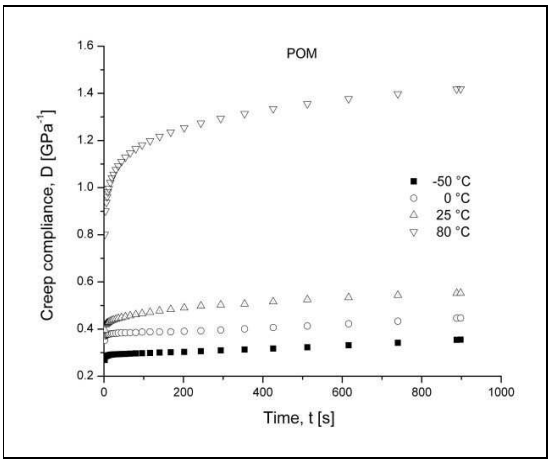

a)

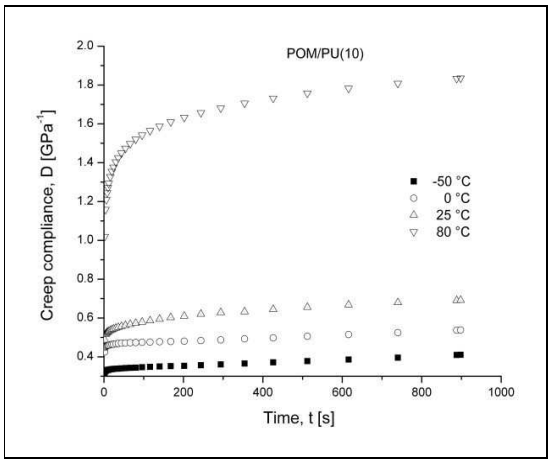

b)

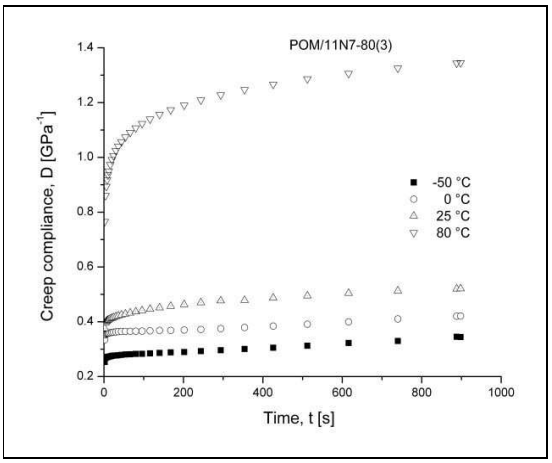

c)

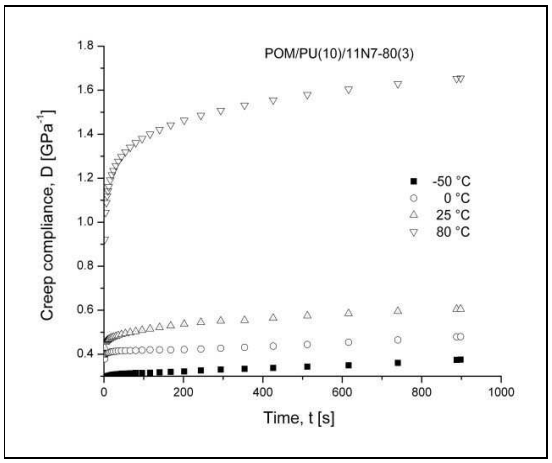

d)

Figure 4.68: Effect of temperature on the tensile creep of POM (a), POM/PU blend (b) POM/alumina binary composite (c) and POM/PU/alumina ternary composite (d) produced by WM-CT

Figure 4.69 displays the course of the experimentally determined a_T values as a function of the temperature. The creep data measured in function of both time and temperature have been considered to create creep master curves by adopting the TTS principle. The creep response at T_0=30 °C was taken for reference.

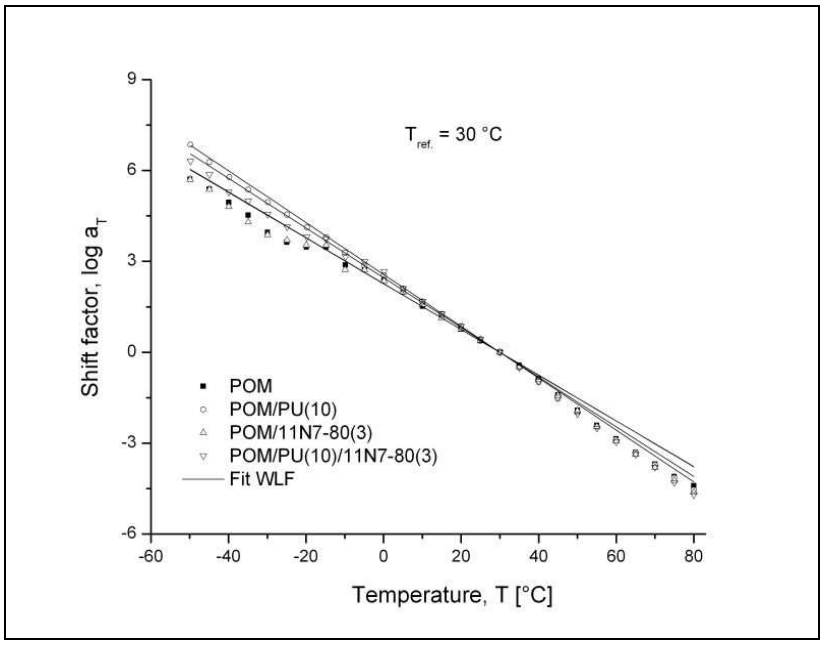

Figure 4.69: Experimental shift factors of the systems studied along with the related WLF fits

Master curves were created by using the same software package of DMTA. Note that this software allows us only horizontal shifting of the creep curves along the time axis. A reference temperature (T_0=30 °C) was used for this superposition process. The empirical formula of creep compliance can be obtained by applying the Findley power law described earlier in section 1.2.4, to the experimental data. Figure 4.70 shows the constructed master curves along with their Findley fits. The parameters of the Findley power law (cf. Equation 1.10) were listed in Table 4.10. The effect of incorporation of alumina particles is that the creep decreased. This was as expected based on the reinforcing effect of the nanoscale disperse alumina. Rubber particles markedly decrease the creep resistance of POM matrix. The POM systems experienced prominent creep by the incorporation of PU for both in POM/PU blend and POM/PU/alumina ternary composite. Figure 4.69 also shows that the power law model fits very well to the creep data for all system up to 3000 hours or at least until a given threshold. It should be noted that the master curves constructed from short-

term creep data at high temperature may not follow the traditional creep behavior pattern, which may be due to increase in the mobility of polymer chains. Thus, the power model is adequate for predicting the creep behavior of materials whose creep modulus may approach zero within a practically limited time. Similar results were reported in the case of PA66/TiO2 nanoparticle system [110]. The authors observed that the power law is good agreement with the experiment for a limited time domain, while for longer time (ln t>13), the calculated data became inadequate.

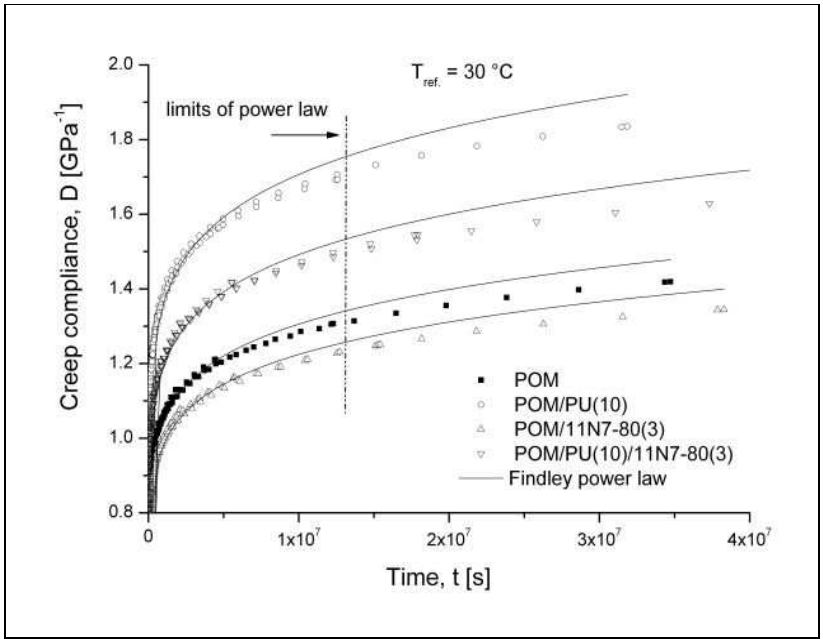

Figure 4.70: Creep master curves (creep compliance vs. time) constructed by considering $T_{ref.}$= 30 °C for the POM based systems. Note: continuou s line represents the Findley fitting

Table 4.10: Findley parameters for the creep mastercurves of the POM-based systems produced by WM-CT, studied

Sample Designation	D_{F0}(GPa^{-1})	D_{F1}($GPa^{-1}s^{1/n}$)	**n**
POM	0.26	0.14	0.122
POM/PU(10)	0.32	0.19	0.124
POM/11N7-80(3)	0.25	0.13	0.123
POM/PU(10)/11N7-80(3)	0.28	0.17	0.124

A creep rate can be quantified as the time derivative (dD/dt) of the creep compliance curves. Figure 4.71 displays the effect of alumina on the creep rate of POM and its blend with PU rubber. Note that the creep rate decreases with increasing time and with addition of alumina particles. It is also clear from this figure that the presence of rubber particles increase the creep rate of POM matrix.

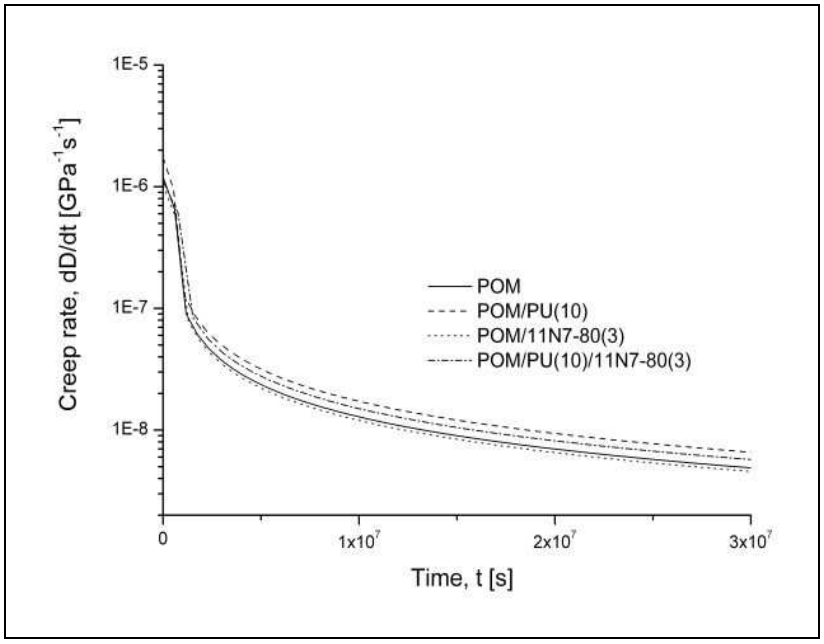

Figure 4.71: Creep rate as a function of time at T=30 °C for the POM systems studied

5 Summary and Outlook

The current work was devoted to develop a novel extrusion melt-compounding method to manufacture tough, nanofiller-reinforced thermoplastics by adding an aqueous filler slurry and/or rubber dispersion to the molten polymer followed by evaporation of the water carrier. The research work also compared the mechanical, thermal and viscoelastic properties of nanoreinforced/toughened thermoplastic composites prepared discontinuously by masterbatch and direct melt mixing processes. The results and conclusions, obtained in this work, are summarized in two parts. Finally, suggestions for future studies are also given in this section.

Discontinuously produced micro- and nanoreinforced polymer composites

Polystyrene/fluorohectorite composites

This combination served to explore the potential benefits of the PS latex mediated dispersion of pristine layered silicate (sodium fluorohectorite, FH) on the properties of melt compounded polystyrene (PS). The FH became intercalated when introduced in the PS melt in form of a dry masterbatch. The corresponding masterbatch was produced by drying the FH containing homogenized PS latex. By contrast, the direct introduction of FH in the PS melt (direct melt mixing) resulted in a microcomposite (limited delamination with hardly any intercalation). The stiffness and strength of the FH-reinforced PS nanocomposites produced by the masterbatch technique were superior to those prepared by melt mixing. Poor dispersion of the FH particles and stacks reduced the ductility of the composites in larger extent compared to those which contained well delaminated and dispersed FH stacks. The creep compliance proved to be a suitable measure of the FH dispersion. Improved dispersion of the layered silicate, associated with the formation of an interphase, is well reflected by a reduction of the initial compliance value. The master curves, constructed based on the isothermal creep experiments, obey the WLF description in the first approximation. The stable creep regime is matrix (bulk)-dominated as the related curve sections of the composites run parallel with that of the PS matrix.

Alumina-filled polystyrene composites

This composite system was used to collate the mechanical, thermal and rheological properties of PS/alumina composites in which the alumina particles are micro- and nano-scaled dispersed. The related dispersion was achieved by melt compounding with (masterbatch technique) and without (direct melt compounding) precompounding of the PS latex with water dispersible alumina of various primary particle sizes. The masterbatch technique resulted in nano-, whereas direct melt blending in PS/alumina microcomposites. This was demonstrated by TEM and SEM investigations. The stiffness, measured in DMTA and tensile tests, of the nanocomposites was markedly higher than that of the microcomposites. The tensile strength and HDT values were also enhanced, however, did not reflect the effects of composite preparation and alumina particle size. The creep results, especially when summarized in compliance vs. time master curves, proved to be very sensitive indications for both alumina size and dispersion type. Rheological tests at very low angular frequencies seem to be also a useful tool to detect effects of the alumina dispersion state.

Polyoxymethylene/polyurethane/alumina ternary composites

This composite system was used to study the potential of the PU latex mediated dispersion of the alumina particles in ternary POM/PU/alumina composites. The latter were produced by the masterbatch (MB) and direct melt mixing (DM) techniques, respectively. The mechanical, thermal and dielectrical properties of the resulting composites were investigated. The dispersion of the alumina was markedly better when produced by MB compared to DM. Introduction of PU and alumina did not affect practically the crystallinity of the POM. The thermooxidative stability of PU toughened POM was markedly improved by the alumina particles. Incorporation of PU decreased the stiffness (enhanced the compliance) of the related POM/PU blend that could be only partly compensated by the alumina filler. The preparation techniques of the composites (MB and DM) had a strong effect on the tensile mechanical, dielectrical, rheological and long-term creep properties. Master curves constructed from short term creep data did not accurately depict the long-term creep behavior of composites. However, the former approach is acceptable for engineering purposes. On the other hand, the preparation method marginally influenced the TGA and creep re-

sponse. The creep behavior was suggested to be controlled by the PU phase along with its dispersion.

Continuously produced toughened and/or reinforced polymer composites

Alumina-filled polystyrene composites

Aqueous alumina suspension was injected into melted PS to prepare reinforced composites by continuously (denoted water mediated continuous technique, WM-CT). Compared with the composites obtained by direct melt mixing (DM-CT), the alumina dispersion can be improved by this strategy. Finer dispersion of the alumina was accompanied with improved elastic modulus along with a dramatic reduction of the strain at break and toughness. Regarding the creep properties, pronounced reduction in the creep compliance was noted for the composite produced by WM-CT with respect to the pure PS and composite prepared by DM-CT at all temperatures. The Burgers model was fairly adequate predict the creep data for short-term test of these PS-based systems.

Polyoxymethylene/polyurethane/alumina ternary composites

Toughened or reinforced polymer composites have been successfully produced by WM-CT. SEM and TEM results have shown that the POM composite systems produced by WM-CT present better alumina or rubber dispersion than those prepared by MB or DM discontinuously. The mechanical properties (stiffness and creep resistance) of the composites were superior to those of the POM and POM/PU blend. The impact resistance of POM was highly enhanced by the addition of PU rubber. Note that the dispersed rubber particle size was closely matched with that one required from usual toughening agents, impact modifiers. The results of creep test are clear from good agreement between the master curves constructed from short-term creep data and the predictions of this power law model. Besides, this WM-CT is a very effective process being simple and cost efficient for producing composite materials, as the expensive chemical modification of the nanofillers can be avoided.

The continuous technique to produce nanocomposites containing alumina- and rubber particles as nanoscale reinforcements and toughness offers a general way to modify the properties, such as stiffness and toughness. However, continuing the work as follow up of the current thesis the following aspects should be considered. The toughened properties of and reinforced nanocomposites should be optimized via various rubber/filler ratios and concentrations. This task requires an extensive design of experiments. A further open issue is to find connections between short- and long-term creep tests and to pinpoint the most likely reasons for the deviation between the corresponding results.

6 Appendix

Stress-relaxation studies, which provide another route to study the time dependence and gain understanding on viscoelastic behavior of polymer and polymeric composites, were carried out and are reported also in this work. Short-time stress relaxation tests were made in tensile mode at different temperatures using dynamic mechanical thermal analysis (DMTA), (DMA Q800 apparatus of TA Instruments, New Castle, USA). The relaxation modulus was determined as a function of the time ($t_{relax.}$ = 60 min.). The tensile strain applied was 0.5 %. This strain value was chosen based on the results of static tensile tests. The 0.5 % strain corresponds to ca. 9 % of the tensile strain at break of the PS. For stress relaxation tests dumbbell-shaped specimens (5B type according to DIN EN ISO 527) were used. The temperature dependence of the relaxation modulus was studied in the temperature range from 25 to 75 °C response of the PS reference and its composites. In this temperature range isothermal tests were run on the same specimen by increasing the temperature stepwise by 5 °C. Prior to the stress relaxation measurement (duration 15 min) the specimen was equilibrated for 5 min at each temperature.

Relaxation modulus

DMTA is one of the simplest techniques which provide information about the viscoelastic properties. Figure 6.1 displays the relaxation modulus values for the PS and its composites produced by DM and MB methods. The shape of the relaxation curves of the composites is similar to that of the PS reference, but their relaxation modulus values are much higher compared to the PS reference. One can see that the relaxation modulus of the nanocomposites produced by the MB method are higher in the whole relaxation time range than those of the microcomposites prepared by DM. The relaxation modulus values of the composites reflect the dispersion state of the FH: a change from micro- to nanocomposite is accompanied with a significant increase in the modulus, as expected. The above results suggest that stress relaxation behaviors are suitable indicators for the dispersion state of the fillers.

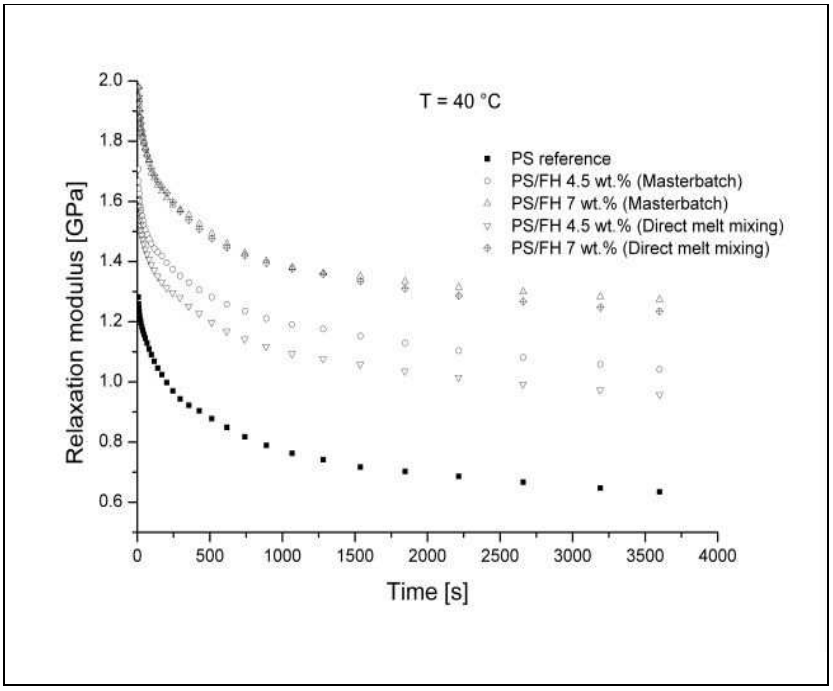

Figure 6.1: Relaxation modulus of the PS reference and its FH composites prepared by different methods

Effect of temperature and time-temperature superposition

Figures 6.2a-6.2c demonstrate the effect of increasing temperature on the relaxation modulus of PS reference, PS/FH micro- and nanocomposites at 4.5 wt.% FH content. The general trend is that the relaxation modulus, read at a given time, decreases with increasing temperature. The relaxation modulus increased remarkably with incorporation of FH compared to the PS reference. One can also notice that at all test temperatures, the nanocomposite manufactured by MB proved to have the highest relaxation modulus. Interestingly, the relaxation modulus rate of the PS at 75 °C is the fastest. When FH were introduced into the PS matrix, the relaxation modulus rate decreased. The increase of the relaxation modulus with increasing filler content is due to the development of an interphase in which molecular mobility is hampered. DMTA as given in Figure 4.9 corroborated this indicating that the glass transition temperature (T_g) of the corresponding micro- and nanocomposites was shifted towards higher temperatures. Thus, the degree of restriction of the mobility of the PS chains, was higher for the nanocomposite (produced by the MB) than for the microcomposite (prepared by DM).

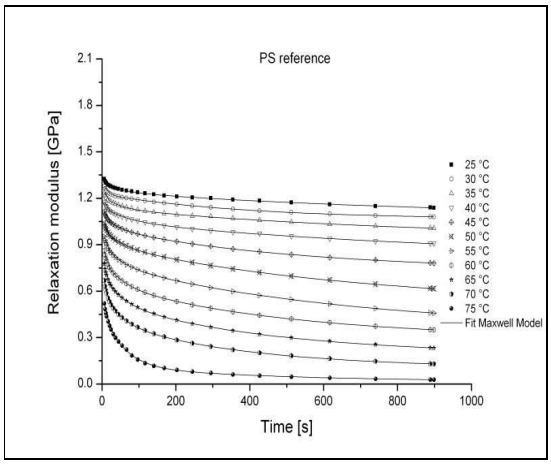

a)

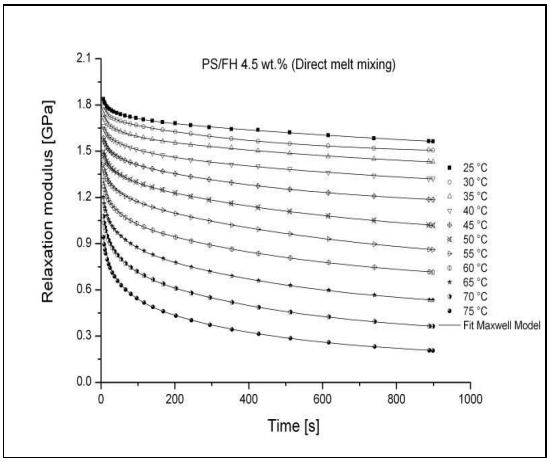

b)

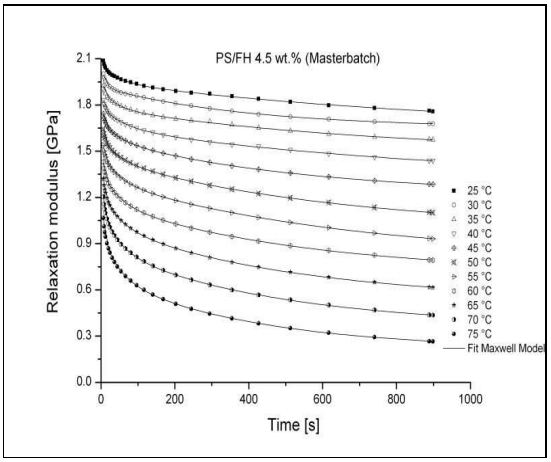

c)

Figure 6.2: Effect of temperature on the relaxation modulus of PS reference (a) and its composites with 4.5 wt.% FH (b and c) prepared by different methods (Stress relaxation conditions were: strain = 0.5 %, relaxation time = 15 min) Note: continuous line represents the Maxwell model fitting

The relaxation curve versus time data were filled by using a phenomenological spring-dashpot model (generalized Maxwell model). The mathematical representation of the relaxation modulus (E_r) for Maxwell model is given by the following equation [111]:

$$E_r(t) = E_0 + \sum_{k=1}^{N} E_k * e^{-t/\tau_k} \qquad (6.1)$$

where E_0 is the zero-time relaxation modulus, and τ_k represents different relaxation times with corresponding relaxation modulus E_k.

This Maxwell model described the experimental data for each temperature properly (cf. Figure 6.2a-6.2c). The values for the parameters derived for each fit using the related software package of the origin 7.5 G SR6 are listed in Table 6.1.

Table 6.1: Maxwell parameters for the relaxation modulus of the PS-based systems studied

Temperature	Parameter	PS reference	+ FH 4.5 wt.% (DM)	+ FH 4.5 wt.% (MB)
30 °C	E_0 (GPa)	1.06	1.48	1.65
	E_{k1} (GPa)	0.06	0.05	0.13
	τ_1 (s)	14.08	25.89	399.46
	E_{k2} (GPa)	0.14	0.24	0.13
	τ_2 (s)	3.01	417.64	399.46
	E_{k3} (GPa)	0.16	0.16	0.16
	τ_3 (s)	404.63	4.63	10.42
50 °C	E_0 (GPa)	0.51	0.91	0.98
	E_{k1} (GPa)	0.14	0.11	0.14
	τ_1 (s)	6.32	53.93	50.41
	E_{k2} (GPa)	0.39	0.43	0.24
	τ_2 (s)	695.53	677.47	5.57
	E_{k3} (GPa)	0.1	0.17	0.46
	τ_3 (s)	50.63	6.72	638.7

70 °C	E_0 (GPa)	0.1	0.29	0.36
	E_{k1} (GPa)	0.31	0.48	0.25
	τ_1 (s)	377.72	473.44	49.74
	E_{k2} (GPa)	0.19	0.23	0.51
	τ_2 (s)	46.61	50.86	473.79
	E_{k3} (GPa)	0.25	0.29	0.32
	τ_3 (s)	6.14	6.54	6.34

Master curves in form of E_r vs. time were produced by superimoposing the relaxation modulus vs. time traces using the time-temperature superposition principle. The shift factors can be also correlated with temperature using the WLF equation 1.6. Figure 6.3 demonstrates that the simple WLF-equation adequately describes the temperature dependence of the shift factors of the PS-systems studied.

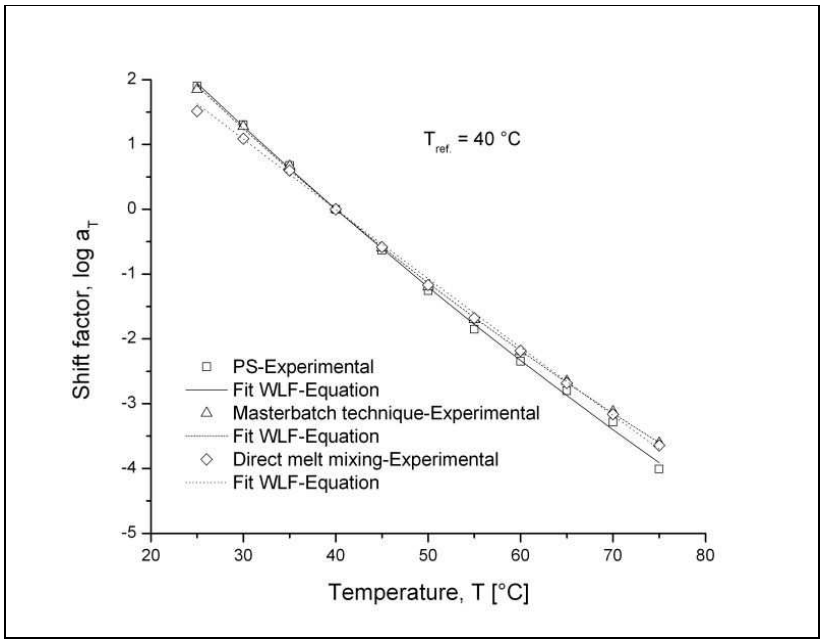

Figure 6.3: Temperature dependence of the shift factor (a_T) based on experimental results and calculation (WLF equation)

The viscoelastic behavior in terms of stress relaxation modulus and creep compliance depends on the polymer structure and testing temperature. As the temperature increases, the mobility of the chains increases and this results in an increased relaxation modulus rate/creep rate at the same applied strain/stress, respectively. In other words, they should be interrelated. If the creep compliance is given by Findley power law, then the relaxation modulus can be obtained by the inverse of the corresponding power function [79].

$$E_{rF} = \left(E_{rF0} + E_{rF1} * t^{n}\right)^{-1} \qquad (6.2)$$

where the subscript F indicates the parameters associated with the Findley power law, n is a constant independent of strain, E_{rF0} is the time-independent relaxation modulus and E_{rF1} is coefficient of the time-dependent term.

The related master curves, viz. relaxation modulus as a function of time, selecting T_{ref}=40 °C as reference temperature, are depicted in Figure 6.4. The reinforcing effect of FH, which increased the tensile relaxation modulus, is obvious in this Figure. Higher relaxation modulus of the nanocomposites compared to the microcomposites was traced to the good dispersion of the FH. This triggered the onset of strong polymer-filler interactions supported by the large specific surface area of the FH. This is to the learning from the corresponding TEM and AFM images (cf. Figure 4.5b and 4.7b, respectively). The experimental data were fitted also by Findley power law approximation. The simulated parameters of the Findley power law was listed in Table 6.2. One may thus conclude that the slope n of the composite produced by MB slightly lower than that the PS reference and the composite produced by DM. However, the inverse Findley law gives satisfactory assessment until a certain time for the PS and its composites.

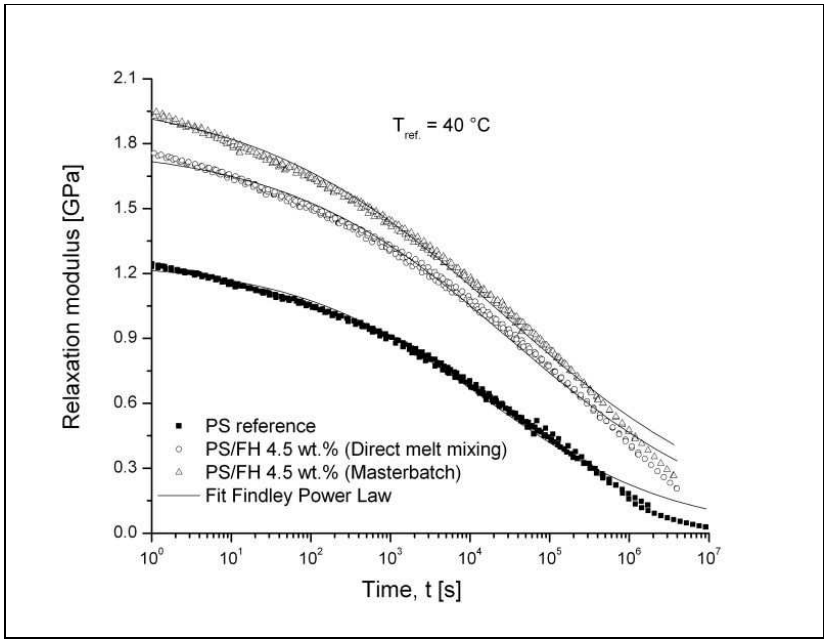

Figure 6.4: Relaxation modulus master curves (compliance vs. time) constructed by considering T_{ref}= 40 °C for the PS reference and its micro- and na nocomposite. Experimental data were fitted by Findley power law (inverse function) approximation

Table 6.2: The simulated parameters of the Findley power law

Sample Designation	$\mathbf{E_{rF0}}$ (GPa)	$\mathbf{E_{rF1}}$ (GPa $s^{1/n}$)	**n**
PS reference	0.79	0.025	0.36
+ FH 4.5 wt.% (DM)	0.56	0.024	0.30
+ FH 4.5 wt.% (MB)	0.49	0.029	0.28

7 References

[1] Wang, Z., Li, G., Peng, H., Zhang, Z., Wang, X.: Study on novel antibacterial high-impact polystyrene/TiO_2 nanocomposites. Journal of Materials Science 40 (2005), pp. 6433-6438.

[2] Ma, C.-C. M., Chen, Y.-J., Kuan, H.-C.: Polystrene nanocomposite materials: Preparation, morphology, and mechanical, electrical, and thermal properties. Journal of Applied Polymer Science 98 (2005), pp. 2266-2273.

[3] Sohn, J.-I., Lee, C.H., Lim, S.T., Kim, T.H., Choi, H.J., Jhon, M.S.: Viscoelasticity and relaxation characteristics of polystyrene/clay nanocomposite. Journal of Materials Science 38 (2003), pp. 1849-1852.

[4] Vuluga, Z., Donescu, D., Radovici, C., Marinache, D., Şerban, S., Vuluga, D.M., Paven, H.: The morphology of polystyrene/organoclay nanocomposites obtained by dynamic melt intercalation. Materiale Plastice 41 (2004), pp. 3-6.

[5] Dazhu, C., Haiyang, Y., Pingsheng, H., Weian, Z.: Rheological and extrusion behavior of intercalated high-impact polystyrene/organomontmorillonite nanocomposites. Composites Science and Technology 65 (2005), pp. 1593-1600.

[6] Jeong, H.M., Choi, J. S., Ahn, Y.T., Kwon, K.H.: Characteristics of polystyrene/organoclay nanocomposites prepared by in-situ polymerization with macroazoinitiator containing poly(dimethylsiloxane) segment. Journal of Applied Polymer Science 99 (2006), pp. 2841-2847.

[7] Yilmazer, U., Ozden, G.: Polystyrene-organoclay nanocomposites prepared by melt intercalation, in situ, and masterctach methods. Polymer Composites 27 (2006), pp. 249-255.

[8] Lim, Y.T., Park, O.O.: Rheological evidence for the microstructure of intercalatedpolymer/layered silicate nanocomposites. Macromolecular Rapid Communications 21 (2000), pp. 231-235.

[9] Hoffmann, B., Dietrich, C., Thomann, R., Friedrich, C., Mülhaupt, R.: Morphology and rheology of polystyrene nanocomposites based upon organoclay. Macromolecular Rapid Communications 21 (2000), pp. 57-61.

[10] Meincke, O., Hoffmann, B., Dietrich, C., Thomann, R., Friedrich, C.: Viscoelastic properties of polystyrene nanocomposites based on layered silicates. Macromolecular Chemistry and Physics 204 (2003), pp. 823-830.

[11] Sikka, M., Cerini, L.N., Ghosh, S.S., Winey, K.I.: Melt intercalation of polystyrene in layered silicates. Journal of Polymer Science Part B: Polymer Physics 34 (1996), pp. 1443-1449.

[12] Kim, T.H., Lim, S.T., Lee, C.H., Choi, H.J., Jhon, M.S.: Preparation and rheological characterization of intercalated polystyrene/organophilic montmorillonite nanocomposite. Journal of Applied Polymer Science 87 (2003), pp. 2106-2112.

[13] Morgan, A.B., Gilman, J.W.: Characterization of polymer-layered silicate (clay) nanocomposites by transmission electron microscopy and X-ray diffraction: A comparative study. Journal of Applied Polymer Science 87 (2003), pp. 1329-1338.

[14] Beyer, F.L., Tan, N.C.B., Dasgupta, A., Galvin, M.E.: polymer-layered silicate nanocomposites from model surfactants. Chemistry of Materials 14 (2002), pp. 2983-2988.

[15] Loos, J., Alexeev, A., Grossiord, N., Koning C.E., Regev, O.: Visualization of single-wall carbon nanotube (SWNT) networks in conductive polystyrene nanocomposites by charge contrast imaging. Ultramicroscopy 104 (2005), pp.160-167.

[16] Chang, T.-E., Kisliuk, A., Rhodes, S.M., Brittain, W.J., Sokolov, A.P.: Conductivity and mechanical properties of well-dispersed single-wall carbon nanotube/polystyrene composite. Polymer 47 (2006), pp. 7740-7746.

[17] Wang, Z., Lu, M., Li, H.-L., Guo, X.-Y.: SWNTs-polystyrene composites preparations and electrical properties research. Materials Chemistry and Physics 100 (2006), pp. 77-81.

[18] Ultracki, L.A., Kamal, M.R.: Clay-containing polymeric nanocomposites. Arabian Journal for Science and Engineering 27 (2002), pp. 43-67.

[19] Alexandre, M., Dubois, P.: Polymer-layered silicate nanocomposites: Preparation, properties and uses of a new class of materials. Materials Science and Engineering Reports 28 (2000), pp. 1-63.

[20] Pinnavaia, T.J., Beall, G.W.: Polymer-Clay Nanocomposites, Wiley, New York, 2000.

[21] Theng, B.K.G.: Formation and Properties of Clay-Polymer Complexes, Elsevier Sientific, Amsterdam, 1979.

[22] Zilg, C., Dietsche, F., Hoffmann, B., Dietrich, Ch., Mülhaupt, R.: Nanofillers based upon organophiclic layered silicates. Macromolecular Symposia 169 (2001), pp. 65-77.

[23] Krishnamoorti, R., Vaia, R.A., Gianellis, E.P.: structure and dynamics of polymer-layered silicate nanocomposite, Chemistry of Materials 8 (1996), pp. 1728-1734.

[24] Tanoue, S., Hasook, A., Itoh, T., Yanou, M., Iemoto, Y., Unryu, T.: Effect of screw rotation speed on the properties of polystyrene/organoclay nanocomposites prepared by a twin-screw extruder. Journal of Applied Polymer Science 101 (2006), pp. 1165-1173.

[25] Li, H., Yu, Y., Yang, Y.: Synthesis of exfoliated polystyrene/montmorillonite nanocomposite by emulsion polymerization using a zwitterion as the clay modifier. European Polymer Journal 41 (2005), pp. 2016-2022.

[26] Uğur, S., Alemdar, A., Pekcan, Ö.: The effect of clay particles on film formation from polystyrene latex. Polymer Composites 27 (2006), pp. 299-308.

[27] Shen, J., Cao, X., Lee, L.: Synthesis and foaming of water expandable polystyrene-clay nanocomposites. Polymer 47 (2006), pp. 6303-6310.

[28] Plummer, C. J. G., Scaramuzzino, P., Kausch, H.-H., Philippoz, J.-M.: High temperature slow crack growth in polyoxymethylene. Polymer Engineering and Science 40 (2000), pp. 1306-1317.

[29] Sukhanova, T., Bershtein, V., Keating, M., Matveeva, G., Vylegzhanina, M., Egorov, V., Peschanskaya, N., Yakushev, P., Flexman, E., Greulich, S., Sauer,

B., Schodt, K.: Morphology and properties of poly(oxymethylene) engineering plastics. Macromolecular Symposia 214 (2004), pp. 135-145.

[30] Lesser, A.J.: Effective volume changes during fatigue and fracture of polyacetal. Polymer Engineering and Science 36 (1996), pp. 2366-2374.

[31] Plummer, C. J. G., Menu, P., Cudré-Mauroux, N., Kausch, H.-H.: The effect of crystallization conditions on the properties of polyoxymethylene. Journal of Applied Polymer Science 55 (1995), pp. 489-500.

[32] Xu, W., He, P.: Isothermal crystallization behavior of polyoxymethylene with and without nucleating agents: Journal of Applied Polymer Science 80 (2001), pp. 304-310.

[33] Mehrabzadeh, M., Rezaie, D.: Impact modification of polyacetal by thermoplastic elastomer polyurethane. Journal of Applied Polymer Science 84 (2002), pp. 2573-2582.

[34] Chiang, W.-Y., Lo, M.-S.: Properties of copolymer-type polyacetal/polyurethane blends. Journal of Applied Polymer Science 36 (1988), pp. 1685-1700.

[35] Kawaguchi, K., Tajima, Y.: interfacial reaction and its influence on phase morphology and impact properties of modified-polyacetal/thermoplastic polyurethane blends. Journal of Applied Polymer Science 100 (2006), pp. 4375-4382.

[36] Gao, X., Qu, C., Zhang, Q., Peng, Y., Fu, Q.: Toughening mechanism in polyoxymethylene/thermoplastic polyurethane blends. Polymer International 53 (2004), pp. 1666-1671.

[37] Gao, X., Qu, C., Zhang, Q., Peng, Y., Fu, Q.: Brittle-ductile transition and toughening mechanism in POM/TPU/$CaCO_3$ ternary composites. Macromolecular Materials and Engineering 289 (2004), pp. 41-48.

[38] Wang, Y., Li, Y., Zhang, R., Huang, L., He, W.: Synthesis and characterization of nanosilica/polyacrylate composite latex. Polymer Composites 27 (2006), pp. 282-288.

[39] Karger-Kocsis, J., Zhang, Z.: In: Mechanical Properties of Polymers Based on Nanostructure and Morphology, edited by Michler, G.H. and Baltá-Calleja, F.J., CRC Press: Boca Raton, FL, USA, 2005, Chapter 13, pp. 553-602.

[40] Varghese, S., Karger-Kocsis, J.: In: Polymer Composites from Nano- to Macro-Scale, edited by Friedrich, K., Fakirov, S., Zhang, Z., Springer: Berlin, 2005, Chapter 5, pp. 77-90.

[41] Karger-Kocsis, J., Wu, C.-M.: Thermoset rubber/layered silicate nanocomposites: Status and future trends. Polymer Engineering and Science 44 (2004), pp. 1083-1093.

[42] Wu, J.-P., Wang, Y.-Q., Zhang, H.-F., Wang, Y.-Z., Yu, D.-S., Zhang, L.-Q., Yang, J.: Rubber-pristine clay nanocomposites prepared by co-coagulating rubber latex and clay aqueous suspension. Composites Science and Technology 65 (2005), pp. 1195-1202.

[43] Varghese, S., Gatos, K.G., Apostolov, A.A., Karger-Kocsis, J.: Morphology and mechanical properties of layered silicate reinforced natural and polyurethane rubber blends produced by latex compounding. Journal of Applied Polymer Science 92 (2004), pp. 543-551.

[44] Wang, C., Wang, Q., Chen, X.: Intercalated PS/Na^+-MMT nanocomposites prepared by ultrasonically initiated in situ emulsion polymerization. Macromolecular Materials Engineering 290 (2005), pp. 920-926.

[45] Li, H., You, B., Gu, G., Wu, L., Chen, G.: Particle size and morphology of poly[styrene-co-(butylacrylate)]/nano-silica composite latex. Polymer International 54 (2005), pp. 191-197.

[46] Ding, P., Qu, B. : Synthesis and characterization of polystyrene/layered double-hydroxide nanocomposites via in situ emulsion and suspension polymerization. Journal of Applied Polymer Science 101 (2006), pp. 3758-3766.

[47] Özdilek, C., Kazimierczak, K., van der Beek, D., Picken, S.J.: Preparation and properties of polyamide-6-boehmite nanocomposites. Polymer 45 (2004), pp. 5207-5214.

[48] Sugama, T., Gawlik, K.: nanoscale boehmite filler for corrosion- and wear-resistant polyphenylenesulfide coatings. Polymer and Polymer Composites 12 (2004), pp. 153-167.

[49] Xalter, R., Halbach, T.S., Mülhaupt, R.: New polyolefin nanocomposites and catalyst supports based on organophilic boehmites. Macromolar Symposia 236 (2006), pp. 145-150.

[50] Shahid, N., Villate, R.G., Barron, A.R. : Chemically functionalized alumina nanoparticle effect on carbon fiber/epoxy composites. Composites Science and Technology 65 (2005), pp. 2250-2258.

[51] Adhikari, R., Henning, S., Lebek, W., Godehardt, R., Ilisch, S., Michler, G.H.: Structure and properties of nanocomposites based on SBS block copolymer and alumina. Macromolecular Symposia 231 (2005), pp. 116-124.

[52] Gatos, K.G., Martínez Alcázar, J.G., Psarras, G.C., Thomann, R., Karger-Kocsis, J.: Polyurethane latex/water dispersible boehmite alumina nanocomposites: Thermal, mechanical and dielectrical properties. Composites Science and Technology 67 (2007), pp. 157-167.

[53] Gowarik; V.R., Viswanathan, N.V., Jayadev, S.: Polymer science, India, New Age International (P) Limited, Publishers, 1986.

[54] Van Krevelen, D.W:: Properties of polymers, Elsevier Sientific, Amsterdam, 1997.

[55] Giannelis, E.P.: Review: Polymer layered silicate nanocomposites. Advanced Materials 8 (1996), pp. 29-35.

[56] Thostenenson, E., Li, C., Chou, T.: Review nanocomposites in context. Composites Science and Technology 65 (2005), pp. 491-516.

[57] Borggreve, R.J.M., Gaymans, R.J., Schuijer, J.: Impact behaviour of nylon-rubber blends: 5. Influence of the mechanical properties of the elastomer. Polymer 30 (1987), pp. 71-77.

[58] Margolina, A., Wu, S.: Percolation model for brittle-tough transition in nylon/rubber blends. Polymer 29 (1988), pp. 2170-2173.

[59] Baldi, F., Bignotti, F., Tieghi, G., Riccó T.: Rubber toughening of polyamide 6/organoclay nanocomposites obtained by melt blending. Journal of Applied Polymer Science 99 (2006), pp. 3406-3416.

[60] Wu, S.: A generalized criterion for rubber toughening: The critical matrix ligament thickness. Journal of Applied Polymer Science 35 (1988), pp. 549-561.

[61] Jiang, W., Yuan, Q., An, L., Jiang, B.: Effect of cavitations on brittle-ductile transition of particle toughened thermoplastic. Polymer Communication 43 (2002), pp. 1555-1558.

[62] Wang, F., Wu, J.K., Xia, H.S., Wang, Q.: Polyoxymethylene/carbon nanotubes composites prepared by solid state mechanochemical approach. Plastics, Rubber and Composites 36 (2007), pp. 396-403.

[63] Sun, T.J., Ye, L., Zhao, X.W.: Thermostabilising and nucleating effect of montmorillonite on polyoxymethylene. Plastics, Rubber and Composites 36 (2007), pp. 350-359.

[64] Yu, L., Yang, S., Wang, H., Xue, Q.: An investigation of the friction and wear bahaviors of micrometer copper particle- and nanometer copper particle-filled polyoxymethylene composites. Journal of Applied Polymer Science 77 (2000), pp. 2404-2410.

[65] Morales-Teyssier, Sánchez-Valdes, S., Ramos-de Valle, L.F.: Effect of carbon nanofiber functionalization on the dispersion and physical and mechanical properties of polystyrene nanocomposites: Macromolecular Materials and Engineering 291 (2006), pp. 1547-1555.

[66] Ma, C.-C. M., Chen, Y.-J., Kuan, H.-C.: Polystrene nanocomposite Materials: Preparation, mechanical, electrical, and thermal properties and morphology. Journal of Applied Polymer Science 100 (2006), pp. 508-515.

[67] Park, E.J., Heo, H., Lim, K. T.: Synthesis and characterization of $Al(OH)_3$/ polystyrene nanocomposite latex particles by emulsion polymerization. Macromolecular Symposia 249-250 (2007), pp. 247-250.

[68] Akelah, A., Moet, A.: Polymer-clay nanocomposites: free-radical grafting of polystyrene on to organophilic montmorillonite interlayers. Journal of Materials Science 31 (1996), pp. 3589-3596.

[66] Wang, D., Zhu, J., Yao, Q., Wilkie, C.A.: A comparison of various methods for the preparation of polystyrene and poly(methylmethacrylate) clay nanocomposites. Chemistry of Materials 14 (2002), pp. 3837-3843.

[70] Chen, G., Qi, Z., Shen, D.: Shear-induced ordered structure in polystyrene/clay nanocomposite. Journal of Materials Research 15 (2000), pp. 351-356.

[71] Zhou, Q., Fan, X., Xia, C., Mays, J., Advincula, R.: Living anionic surface initiated polymerization (SIP) of styrene from clay surfaces. Chemistry of Materials 13 (2001) , pp. 2465-2467.

[72] Grunlan, J.C., Mehrabi, A.R., Bannon, M.V.: Water-based single-walled-nanotube-filled polymer composite with an exceptionally low percolation thershold. Advanced Materials 16 (2004), pp. 150-153.

[73] Grunlan, J.C., Kim, Y.S., Ziaee, S., Wei, X., Abdel-Magid, B., Tao, K.: Thermal and mechanical behavior of carbon nanotube-filled latex. Macromolecular Materials and Engineering 291 (2006), pp. 1035-1043.

[74] Xia, H., song, M., Zhang, Z., Richardson, M.: Microphase separation, stress relaxation, and creep behavior of polyurethane nanocomposites. Journal of Applied Polymer Science 103 (2002), pp. 2992-3002.

[75] Eckstein, A., Suhm, J., Friedrich, C., Maier, R.D., Sassmannshausen, J., Bochmann, M., Mülhaupt, R.: Determination of plateau moduli and entanglement molecular weights of isotatic, sydiotactic, and atactic polypropylenes synthesized with metallocene catalysts. Macromolecules 31 (1998), pp. 1335-1340.

[76] Schapery, R.A.: On the characterization of nonlinear viscoelastic materials. Polymer Engineering and Science 9 (1969), pp. 295-310.

[77] Brueller, O.S.: On the nonlinear characterization of the long term behavior of polymeric materials. Polymer Engineering and Science 27 (1987), pp. 144-148.

[78] Ferry, J.D.: Viscoelastic Properties of Polymers, Wiley, New York, 1980.

[79] Palade, L.I., Verney, V., Attane, P.: Time-temperature superposition and kinear viscoelasticity of polybutadienes. Macromolecules 28 (1995), pp. 7051-7057.

[80] Williams, M.L., Landel, R.F., Ferry, J.D.: The temperature dependence of relaxation mechanisms in amorphous polymers and other glass-forming liquids. Journal of the American Chemical Society 77 (1955), pp. 3701-3706.

[81] Ward, I.M.: Mechanical properties of solid polymers, New York: John Wiley & Sons, Inc 1979, Chapter 7.

[82] Findley, W.N., Lai, J.S., Onaran, K.: Creep and relaxation of nonlinear viscoelastic materials,New York: Dover Publications, Inc 1989.

[83] Kaschta, J., Schwarzl, F. R.: Calculation of discrete retardation spectra from creep data-I. Method. Rheologica Acta 33 (1994), pp. 517-529.

[84] Yang J.L., Zhang Z., Schlarb A.K., Friedrich K.: On the characterization of tensile creep resistance of polyamide 66 nanocomposites. Part II: Modeling and prediction of long-term performance. Polymer 47 (2006), pp. 6745-6758.

[85] Yang, J.L.: Characterization, modelling and prediction of the creep resistance of polymer nanocomposites. Dissertation, University of Kaiserslautern, IVW Verlag 72 (2006).

[86] Lu, J.P., Burn, L.S., Tiganis, B.E.: Creep modelling of ABS pipes at variable temperature. Polymer Engineering and Science 40 (2000), pp. 2407-2413.

[87] Shaw, M.T, MacKnight, W.J: Introduction to polymer viscoelasticity, New York: John Wiley & Sons, Inc 2005, Chapter 2.

[88] Houshyar, S., Shanks, R.A., Hodzic, A.: Influence of different woven geometry in poly(propylene) woven composites, Macromolecular Materials and Engineering 290 (2005), pp. 45-52.

[89] Streller, R.C., Thomann, R., Torno, O., Mülhaupt, R.: Isotactic poly(propylene) nanocomposites based upon boehmite nanofillers, Macromolecular Materials and Engineering 293 (2008), pp. 218-227.

[90] Gatos, K.G., Karger-Kocsis, J.: Effects of primary and quaternary amine intercalants on the organoclay dispersion in a sulfur-cured EDPM rubber. Polymer 46 (2005), pp. 3069-3076.

[91] Chen, H.Y., Stepanov, E.V., Chum, S.P., Hiltner, A., Baer, E.: Creep behavior of amorphous ethylene-styrene interpolymers in the glass transition region. Journal Polymer Science Part B: Polymer Physics, 1999, 37, pp. 2373-2382.

[92] Bellemare, S.C., Bureau, M.N., Denault, J., Dickson, J.I. : Fatigue crack initiation and propagation in polyamide-6 and in polyamide-6 nanocomposites Polymer Composites 25 (2004), pp. 433-441.

[93] Satapathy, B.K., Weidisch, R., Pötschke, P., Janke, A.: Crack toughness behaviour of multiwalled carbon nanotube (MWNT)/polycarbonate nanocomposites. Macromolecular Rapid Communications 26 (2005), pp. 1246-1252.

[94] Karger-Kocsis, J.: In: The Application of Fracture Mechanics to Polymers: Adhesives and Composites, edited by Moore, D.R., Elsevier and ESIS, Oxford, 2004, pp. 233-239.

[95] Yang J.L., Zhang Z., Schlarb A.K., Friedrich K.: On the characterization of tensile creep resistance of polyamide 66 nanocomposites. Part I: Experimental results and general discussions. Polymer 47 (2006), pp. 2791-2801.

[96] Horrion, J., Cartasegna, S., Agarwal, P.K.: Morphology, thermal, and mechanical properties of polyacetal/ionomer blends. Polymer Engineering and Science 36 (1996), pp. 2061-2068.

[97] Kaito, A., Nakayama, K., Kanetsuna, H.: Roller drawing of polyoxymethylene. Journal of Applied Polymer Science 32 (1986), pp. 3499-3513.

[98] Hojfors, R.J., Baer, E., Geil, P.H.: Dynamic-mechanical study of molecular motions in solid polyoxymethylene copolymer from 4 to 315 °K. Journal of Macromolecular Science, Part B Physics (3) 1977, pp. 323-348.

[99] Van Beck, L.K.H.: Dielectric Behaviour of Heterogeneous Systems, edited by Briks, J.B., Progress in Dielectrics, London: Heywood Books, 1967, pp. 69-117.

[100] Sillars, R.W.: The properties of a dielectric containing semi-conducting particles of various shapes. Journal of Institution of Electrical Engineerings 80 (1937), pp. 378-394.

[101] Hedvig, P.: Dielectric Spectroscopy of Polymers. Bristol: Adam Hilger, 1977, p. 283.

[102] Tsangaris, G. M., Psarras, G. C.: The dielectric response of a polymeric three-component composite. Journal of Materials Science 34 (1999), pp. 2151-2157.

[103] Tsangaris, G. M., Psarras, G. C., Kouloumbi, N.: Electric modulus and interfacial polarization in composite polymeric systems. Journal of Materials Science 33 (1998), pp. 2027-2037.

[104] Psarras, G. C., Gatos, K.G., Karahaliou, P.K., Georga, S.N., Krontira, C.A., Karger-Kocsis, J.: Relaxation phenomena in rubber/layered silicate nanocomposites. eXPRESS Polymer Letters 1 (2007), pp. 837-845.

[105] Sauer, B. B., Avakian, P., Flexman, E. A., Keating, M., Hsiao, B. S., Verma, R. K.: A.C. dielectric and TSC studies of constrained amorphous motions in flexible polymers including poly(oxymethylene) and miscible blends. Journal of Polymer Science Part B: Polymer Physics 35 (1997), pp. 2121-2132.

[106] Wasylyshyn, D. A.: Effects of moisture on the dielectric properties of polyoxymethylene (POM). IEEE Transactions on Dielectrics and Electrical Insulation 12 (2005), pp. 183-193.

[107] Boyd, R. H.: Relaxation processes in crystalline polymers: Molecular interpretation – a review Polymer 26 (1985), pp. 1123-1133.

[108] Psarras, G. C., Gatos, K. G., Karger-Kocsis, J.: Dielectric properties of layered silicate-reinforced natural and polyurethane rubber nanocomposites. Journal of Applied Polymer Science 106 (2007), pp.1405-1411.

[109] Shen, L., Du, Q., Wang, H., Zhong, W., Yang, Y.: In situ polymerization and characterization of polyamide-6/silica nanocomposites derived from water glass. Polymer International 53 (2004), pp. 1153-1160.

[110] Starkova, O., Yang, J.L., Zhang, Z.: Application of time-stress superstition to nonlinear creep of polyamide 66 filled with nanoparticles of various sizes. Composites Science and Technology 67 (2007), pp. 2691-2698.

[111] Manich, A.M., Castellar, M.D. de, González, B., Ussman, M.A., Marsal, A.: Influence of leather stretching to gain area yield on its stress-relaxation behavior. Journal of Applied Polymer Science, 102 (2006), pp. 6000-6008.

List of Publications

Journals

1. Siengchin, S., Karger-Kocsis, J.: Creep behaviour of polystyrene/fluorohectorite micro- and nanocomposites. Macromolecular Rapid Communications 27 (2006), pp. 2090-2094.

2. Siengchin, S., Karger-Kocsis, J., Thomann, R.: Alumina filled polystyrene micro- and nanocomposites prepared by melt mixing with and without latex precompounding: structure and properties, Journal of Applied Polymer Science 105 (2007), pp. 2963-2972.

3. Siengchin, S., Karger-Kocsis, J., Apostolov, A.A., Thomann, R.: Polystyrene-fluorohectorite nanocomposites prepared by melt mixing with latex precompounding: structure and mechanical properties, Journal of Applied Polymer Science 106 (2007), pp. 248-254.

4. Abraham, T.N., Siengchin, S., Karger-Kocsis, J.: Dynamic mechanical thermal analysis of all-PP composites based on β and α polymorphic forms, Journal of Materials Science 43 (2008), pp. 3697-3703.

5. Siengchin, S., Karger-Kocsis, J., Psarras, G.C., Thomann, R.: Polyoxymethylene/polyurethane/alumina ternary composites: structure, mechanical, thermal and dielectric properties, Journal of Applied Polymer Science 110 (2008), pp. 1613-1623.

6. Siengchin, S., Abraham, T.N., Karger-Kocsis, J.: Structure–stress relaxation relationship in polystyrene/fluorohectorite micro- and nanocomposites, Mechanics of Composite Materials 5 (2008), pp. 709-722.

7. Abraham, T.N., Ratna, D., Siengchin, S., Karger-Kocsis, J.: Rheological and thermal properties of poly(ethylene) oxide/ multi wall carbon nanotube composites, Journal of Applied Polymer Science 110 (2008), pp. 2094-2101.

8. Abraham, T.N., Ratna, D., Siengchin, S., Karger-Kocsis, J.: Structure and properties of poly (ethylene oxide) organo clay nanocomposite prepared via melt mixing, Polymer Engineering and Science, in press.

9. Jiang, Z., Siengchin, S., Steeg, M., Karger-Kocsis, J., Zhou, L.: Poly (butylene terephthalate)/silica nanocomposites prepared from cyclic butylene terephthalate, Composites Part A: Applied Science and Manufacturing, submitted.
10. Siengchin, S., Karger-Kocsis, J., Thomann, R.: Nanofilled and/or toughened POM composites produced by water-mediated melt compounding: structure and mechanical properties, eXPRESS Polymer Letters 2 (2008), pp. 746-756.
11. Ratna, D., Abraham, T.N., Siengchin, S., Karger-Kocsis, J.: Novel method for dispersion of multiwall carbon nanotube in poly (ethylene oxide) matrix: Effect of dicarboxylic acid salts, communicated.

Conference and Symposium Proceedings

1. Siengchin, S., Karger-Kocsis, J.: Structure-property relationships of polystyrene/layered silicate nanocomposites as a function of their preparation, TNT 2006 „Trends in Nanotechnology“ Conference, Grenoble , France, 04.-08. September 2006, CD-ROM.
2. Siengchin, S., Karger-Kocsis, J.: Polystyrene-based micro- and nanocomposites: production (latex compounding) and characterization, IVW-Kolloquium 2006, IVW-Schrifteneihe Band 68, 14.-15. November 2006, pp. 164-165.
3. Siengchin, S., Karger-Kocsis, J.: Structure-property relationships in POM/PU/nanofiller ternary composites produced via the latex route, 12. Probemseminar “Gefüllte und verstärkte Polymerblends Nanoblends, Bad Lauchstädt, Germany, 28.-29. March 2007, p. 51.
4. Siengchin, S., Karger-Kocsis, J.: Creep and thermo- mechanical behavior of toughened and “nanoreinforced” polyamides produced via latex route: effect of the nanofiller, Materiais 2007, Porto, Portugal, 1.-4. April 2007, p. 292.
5. Siengchin, S., Karger-Kocsis, J.: Structure-property relationships in toughened and “nanoreinforced” polyamides produced via latex route: effect of the nanofiller, Eurofillers 2007, Zalakaros, Hungary, 26.-30. August 2007, p. 99.
6. Schlarb, A.K., Siengchin, S., Knör, N., Karger-Kocsis, J.: Creep behavior of thermoplastics containing nano-scale reinforcements, COMAT 2007, Rio De Janeiro, Brazil, proceedings, 9.-12. December 2007.

7. Siengchin, S., Karger-Kocsis, J.: Polystyrene-based micro- and nanocomposites: structure-mechanical relaxation relationship, MCM 2008, Riga, Latvia, 26.-30. May 2008, pp. 244-245.

Student Support Work

Bergmann, C.: Mechanical investigation on NBR/nanofiller based PA-6 produced via the latex route, Studienarbeit, Technische Universität Kaiserslautern (2007).